

# *Contents*

<b>Introduction</b>	<b>3</b>
<b>I Theoretical Foundation</b>	<b>7</b>
<b>1 The Many Body Problem</b>	<b>9</b>
1.1 The Many Body Hamiltonian . . . . .	9
1.2 The Born Oppenheimer Approximation . . . . .	10
1.3 Density Functional Theory . . . . .	12
1.4 The Born-Oppenheimer Surface . . . . .	14
1.5 Kohn-Sham Scheme . . . . .	15
1.6 Approximations to the exchange-correlation energy . . . . .	17
1.7 Periodic Systems . . . . .	19
1.8 Conclusion . . . . .	20
<b>2 Nuclear and Lattice Dynamics</b>	<b>21</b>
2.1 Harmonic Approximation . . . . .	22
2.2 Extended Systems . . . . .	25
2.3 Statistical Mechanics and Molecular Dynamics . . . . .	31
2.4 Classical harmonic dynamics and harmonic mapping . . . . .	36
<b>3 Heat Transport</b>	<b>41</b>
3.1 Linear Response Theory . . . . .	42
3.2 Heat Flux Definition . . . . .	45
3.3 Ab initio Heat Flux . . . . .	48
3.4 Heat Flux in the Harmonic Approximation . . . . .	50
3.5 Ab initio Green Kubo . . . . .	54
3.6 Conclusion . . . . .	55
<b>II Applications</b>	<b>57</b>
<b>4 Anharmonicity</b>	<b>59</b>
4.1 Definition of Anharmonicity . . . . .	59
4.2 Anharmonicity measure . . . . .	60
4.3 Anharmonicity and thermal conductivity . . . . .	64
4.4 Candidate Materials . . . . .	65
4.5 Dynamical effects . . . . .	67
<b>5 Ab Initio Green Kubo: Implementation</b>	<b>75</b>

5.1	Noise Reduction Scheme and Cutoff Estimation . . . . .	77
5.2	Size extrapolation . . . . .	79
5.3	Simulation Time Convergence . . . . .	80
5.4	Comparison to Literature Values . . . . .	81
5.5	Case Study Copper Iodide . . . . .	83
5.6	Conclusion . . . . .	84
<b>6</b>	<b>Thermal Conductivities for Strongly Anharmonic Compounds</b>	<b>85</b>
6.1	Convergence estimation . . . . .	85
6.2	Comparison to Experiment . . . . .	86
6.3	New materials and relation to anharmonicity . . . . .	88
6.4	Conclusion . . . . .	90
<b>7</b>	<b>Conclusion</b>	<b>93</b>
7.1	Summary . . . . .	93
7.2	Outlook . . . . .	94
7.3	Perspective . . . . .	96
<b>Bibliography</b>		<b>99</b>
<b>Appendices</b>		<b>119</b>
<b>A</b>	<b>Notation</b>	<b>121</b>
<b>B</b>	<b>Bloch Theorem and Brillouin Zone</b>	<b>123</b>
<b>C</b>	<b>Born-von Karman Supercell</b>	<b>125</b>
<b>D</b>	<b>Numerical Force Constants</b>	<b>127</b>
<b>E</b>	<b>Geometry Optimization for Crystals</b>	<b>129</b>
<b>F</b>	<b>Linear Response Distribution Function</b>	<b>133</b>
<b>G</b>	<b>Explicit Formulas</b>	<b>135</b>
<b>H</b>	<b>Computational details</b>	<b>137</b>
<b>I</b>	<b>Experimental References</b>	<b>139</b>

# *Introduction*

*“Die Zeit des unbedenklichen Wirtschaftens mit den Energiequellen und Stofflagern, die uns die Natur zur Verfügung gestellt hat, wird wahrscheinlich schon für unsere Kinder nur noch die Bedeutung einer vergangenen Wirtschaftsepoke haben.”*

W. Schottky, 1929 [1]

ONE OF THE MAJOR CHALLENGES humankind faces in the 21th century is the responsible and sustainable handling of the earth’s natural resources. Yet, most energy today is lost as waste heat during the transformation of raw energy sources to usable power. To date, there is no fuel based heat engine that exceeds an efficiency of 50 % and often it is even worse [2]. Since gas- and aircraft-turbines are essentially Carnot engines, their efficiency and core power are directly related to combustion temperature [3, 4]. This relationship has been taken advantage off during the past 30 years by developing ceramics with high thermal resistivity that are nowadays applied as *thermal barrier coatings* on turbine airfoils in heat engines: thin heat insulating layers that allow to operate a turbine at higher temperatures, thereby increasing its efficiency [5].

A complementary strategy is to recycle waste heat where it occurs. One way of achieving this is by using the *thermoelectric effect* to generate electric power from temperature gradients [6]. The main obstacle preventing mass operation is the limited conversion rate (figure of merit)  $zT$  of even the most advanced thermoelectric materials known to date. To make matters worse, these materials often contain heavy metals and are toxic, and their manufacturing process is difficult and expensive [7]. Recent advancements in the field, such as the discovery of a high thermoelectric figure of merit in the lead-free material Tin Selenide [8], offer hope that novel materials with significant figure of merit that are non-toxic, easy and cheap to produce, and consist of abundant elements, can be found.

A KEY PHYSICAL PROPERTY of both thermal barrier coatings (TBCs) and thermoelectrics is their thermal conductivity  $\kappa$ . In the case of thermoelectrics, the figure of merit is inversely proportional to  $\kappa$  [7]:

$$zT = \frac{S^2 \sigma_{\text{el}}}{\kappa} T, \quad (1)$$

where  $T$  denotes the temperature,  $S$  the Seebeck coefficient, and  $\sigma_{\text{el}}$  is the electrical conductivity. A prerequisite to finding better thermoelectrics or

TBCs is to find materials which are thermally insulating. These are typically non-metals, since the free electrons in metals are good heat carriers, and most of the known thermoelectrics are thermally insulating inorganic semiconductors [7, p. 15].

Despite the technological need, systematic knowledge of thermal conductivities in inorganic compounds is scarce. A database like Springer Materials only lists thermal conductivities for about 200 of these compounds [9], which is partially due to the fact that accurate measurements of thermal conductivity are challenging to perform and reproducibility between different experimental groups is often not guaranteed [10]. As a consequence, thermal conductivity is not systematically understood beyond semi-empirical and phenomenological trends in a very limited number of simple material classes [11].

THE AIM OF THIS WORK is therefore to open a new pathway for overcoming the problem of limited data by devising a route to systematically scan material space for thermal insulators and calculate their thermal conductivities from first principles.

While the theoretical foundations of thermal transport in non-metals are about one hundred years old,<sup>1</sup> the simulation of thermal conductivities with predictive accuracy from first principles only emerged in the past fifteen years in the framework of Boltzmann transport theory [13]. Yet, as we will see later, thermal insulators are often strongly *anharmonic* and require a non-perturbative treatment to describe their dynamical properties accurately. Such a fully non-perturbative treatment in terms of *ab initio* Green-Kubo theory is available since five years [14, 15]. However, the number of solid materials computed by the latter approach is very small: Solid silicon and zirconia [15], ice X [16], and amorphous silica [17].

THE APPROACH ADOPTED IN THIS WORK IS THEREFORE TWOFOLD: After reviewing the relevant theoretical tools necessary to simulate heat transport in thermal insulators, we describe how to assess anharmonicity in a quantitative and parameter-free way. In a second step, we use this “measure of anharmonicity” to identify candidate thermal insulators. We subsequently compute non-perturbative thermal conductivities for 60 materials with nearly experimental accuracy, thereby increasing the number of materials studied with *ab initio* Green Kubo by an order of magnitude while suggesting several new materials as effective thermal insulators. Furthermore, the data is used to test trends in material space previously based on experimental data, such as the quantitative relation between thermal conductivity and anharmonicity.

### *Organization of the Thesis*

The thesis is split into two parts: The first part introduces the theoretical concepts necessary to understand thermal transport in materials from an *ab initio* perspective. In chapter one, we will introduce the quantum-mechanical many-body problem and describe the necessary steps and key approximations that lead to Kohn-Sham density functional theory as a way of solving the electronic problem in practice. Chapter two will describe the key concepts of nuclear dynamics that are necessary to study thermodynamical properties of

<sup>1</sup> The many pitfalls in early attempts to describe thermal transport in semiconductors was summarized by Peierls in his memorial text in honor of Wolfgang Pauli [12].

materials, such as heat transport: The chapter introduces the harmonic approximation as a powerful starting point for studying dynamical properties of matter, and the fully non-perturbative treatment of nuclear dynamics and thermodynamic properties in terms of molecular dynamics simulations. Chapter three is dedicated to heat transport theory in the framework of linear response as formulated in the Green-Kubo formalism. The purpose is to clarify how heat transport emerges from the many-body Schrödinger equation, and how, in principle, thermal conductivity can be computed from first principles.

The second part can be understood as an application of this body of theory and is devoted to the investigation of materials in the context of heat transport. In chapter four, we introduce a novel concept to quantify the anharmonicity of material as a means to detect materials that should be treated non-perturbatively. As we will see, this quantity directly correlates with a material's thermal conductivity and therefore enables to predict candidate thermal insulators. Chapter five is devoted to introducing the technical details necessary to run *ab initio* Green Kubo (aiGK) simulations in practice. In chapter six, we present results for 60 materials, first for 20 where experimental reference is available to benchmark the aiGK method, then for the remaining materials where thermal conductivity was previously unknown. In this context, we discuss the underlying microscopic mechanisms, in particular the relation to anharmonicity.

After discussing our results, we conclude with a summary and an outlook on new questions that arose in the course of this work.

check

check



# **Part I**

## **Theoretical Foundation**



# 1

## The Many Body Problem

*“The underlying physical laws necessary for the mathematical theory of a large part of physics and the whole of chemistry are [...] completely known, and the difficulty is only that the exact application of these laws leads to equations much too complicated to be soluble. It therefore becomes desirable that approximate practical methods of applying quantum mechanics should be developed, which can lead to an explanation of the main features of complex atomic systems without too much computation.”*

P.A.M. Dirac, 1929 [18]

IN THIS CHAPTER, we summarize the theoretical background of *ab initio* simulations starting from the non-relativistic, time-independent Schrödinger equation for a general many-body system.

### 1.1 The Many Body Hamiltonian

The full (non-relativistic) many body Hamiltonian in the absence of external electromagnetic fields for an otherwise arbitrary system reads

$$\hat{H} = \hat{T}^e + \hat{V}^{e-e} + \hat{V}^{e-\text{Nuc}} + \hat{V}^{\text{Nuc}-\text{Nuc}} + \hat{T}^{\text{Nuc}}, \quad (1.1)$$

where

$$\hat{T}^e = \sum_i \frac{\hat{\mathbf{p}}_i^2}{2m_e} \quad (1.2)$$

is the kinetic energy operator for electrons of mass  $m_e$  with momentum operators  $\hat{\mathbf{p}}_i$ , and

$$\hat{V}^{e-e} = \sum_{i < j} \frac{e^2}{|\hat{\mathbf{r}}_i - \hat{\mathbf{r}}_j|}, \quad (1.3)$$

is the Coulombic electron-electron repulsion operator with the electronic position operators  $\hat{\mathbf{r}}_i$  and the elementary charge  $e$ . The Coulomb attraction between the negatively charged electrons and the positively charged nuclei reads

$$\hat{V}^{e-\text{Nuc}} = - \sum_{i,J} \frac{Z_J e^2}{|\hat{\mathbf{r}}_i - \hat{\mathbf{R}}_J|}, \quad (1.4)$$

where  $Z_J$  denotes the charge number of nucleus  $J$ , and  $\hat{\mathbf{R}}_J$  is the nuclear position operator. Accordingly, we define the nuclear-nuclear repulsion as

$$\hat{V}^{\text{Nuc-Nuc}} = \sum_{I < J} \frac{Z_I Z_J e^2}{|\hat{\mathbf{R}}_I - \hat{\mathbf{R}}_J|}, \quad (1.5)$$

and the kinetic energy operator for nuclei with momentum operators  $\hat{\mathbf{P}}_I$  and masses  $M_I$  reads

$$\hat{T}^{\text{Nuc}} = \sum_I \frac{\hat{\mathbf{P}}_I^2}{2M_I}. \quad (1.6)$$

This Hamiltonian governs the dynamical evolution of a many-particle system represented by a state  $|\Psi\rangle$  via the time dependent Schrödinger equation,

$$\hat{H} |\Psi\rangle = i\hbar \frac{\partial}{\partial t} |\Psi\rangle, \quad (1.7)$$

from which all material properties (neglecting relativistic and effects and electromagnetic fields) follow.

## 1.2 The Born Oppenheimer Approximation

We go over to a unitless Hamiltonian by scaling Eq. (1.1) with the Hartree energy  $E_h = m_e e^4 / \hbar^2 \approx 27.2 \text{ eV}$ , where  $\hbar$  denotes the Planck constant. Distances are expressed in terms of the Bohr radius  $a_0 = \hbar^2 / me^2$  such that  $\hat{\mathbf{r}} \equiv \mathbf{r} = a_0 \tilde{\mathbf{r}}$ , and the momentum operators are replaced by the respective differential operators,  $\hat{\mathbf{p}} = -i\hbar \partial / \partial \mathbf{r}$  [19]. We find

$$\begin{aligned} \hat{H} &\equiv \hat{H}/E_h \\ &= -\frac{1}{2} \sum_i \frac{\partial^2}{\partial \tilde{\mathbf{r}}_i^2} + \sum_{i < j} \frac{1}{|\tilde{\mathbf{r}}_i - \tilde{\mathbf{r}}_j|} - \sum_{i, J} -\frac{Z_J}{|\tilde{\mathbf{r}}_i - \tilde{\mathbf{R}}_J|} + \sum_{I < J} \frac{Z_I Z_J}{|\tilde{\mathbf{R}}_I - \tilde{\mathbf{R}}_J|} \\ &\quad - \underbrace{\frac{1}{2} \sum_I \frac{m_e}{M_I} \frac{\partial^2}{\partial \tilde{\mathbf{R}}_I^2}}_{\hat{T}^{\text{Nuc}}}, \end{aligned} \quad (1.8)$$

which depends on the charge numbers  $\{Z_I\}$  and the mass ratios  $\{m_e/M_I\}$ . From this viewpoint, we see that the relative order of magnitude of the nuclear kinetic energy  $\hat{T}^{\text{Nuc}}$  is  $m_e/M_I \approx 10^{-4} - 10^{-5}$ . This means that the nuclear kinetic energy can be treated as a perturbation term with respect to the electronic and electron-nuclear contributions,

$$\hat{H} = \hat{H}^0 + \hat{T}^{\text{Nuc}}, \text{ where} \quad (1.9)$$

$$\hat{H}^0 = \hat{T}^e + \hat{V}^{e-e} + \hat{V}^{e-\text{Nuc}} + \hat{V}^{\text{Nuc-Nuc}}. \quad (1.10)$$

In our notation, the time-independent many-body Schrödinger equation reads

$$\hat{H}\psi(\mathbf{r}, \mathbf{R}) = E\psi(\mathbf{r}, \mathbf{R}), \quad (1.11)$$

with ground-state eigenvalues  $E$  and many-body wave functions  $\psi(\mathbf{r}, \mathbf{R})$ , where  $\mathbf{r} = (\mathbf{r} \dots \mathbf{r}_{N_e})$  denotes all electronic coordinates, and  $\mathbf{R} = (\mathbf{R}_1 \dots \mathbf{R}_{N_{\text{Nuc}}})$  the nuclear coordinates, respectively. According to Eq. (1.9), we expand the wave functions  $\psi(\mathbf{r}, \mathbf{R})$  in a complete set of orthonormal basis functions  $\phi_l$ ,

$$\psi(\mathbf{r}, \mathbf{R}) = \sum_l \chi_l(\mathbf{R}) \phi_l(\mathbf{r}; \mathbf{R}), \quad (1.12)$$

where the  $\phi_l$  are the solutions to the Hamiltonian  $\hat{H}^0$ ,

$$\hat{H}^0 \phi_l(\mathbf{r}; \mathbf{R}) = E_l^0(\mathbf{R}) \phi_l(\mathbf{r}; \mathbf{R}) . \quad (1.13)$$

The functions  $\phi_l$  and the eigenvalue  $E_l^0(\mathbf{R})$  depend *parametrically* on  $\mathbf{R}$ , which means that they are obtained for a nuclear configuration  $\mathbf{R}$  regarded as fixed. The nuclear functions  $\chi_l$  are determined by using the expanded wavefunction  $\psi$  given by Eq.(1.12) in the full Schrödinger equation (1.11),

$$\begin{aligned} (\hat{H} - E)\psi(\mathbf{r}, \mathbf{R}) &= \sum_l (\hat{H}^0 + \hat{T}^{\text{Nuc}} - E)\chi_l(\mathbf{R})\phi_l(\mathbf{r}, \mathbf{R}) \\ &= \sum_l (E_l^0(\mathbf{R}) + \hat{T}^{\text{Nuc}} - E)\chi_l(\mathbf{R})\phi_l(\mathbf{r}, \mathbf{R}) = 0 , \end{aligned} \quad (1.14)$$

and integrating with  $\int d^3r \phi_m^*(\mathbf{r}, \mathbf{R})$  using their orthonormality, so that

$$\left( \hat{T}^{\text{Nuc}} + E_m^0(\mathbf{R}) \right) \chi_m(\mathbf{R}) + \sum_l \hat{C}_{ml}(\mathbf{R}) \chi_l(\mathbf{R}) = E \chi_m(\mathbf{R}) . \quad (1.15)$$

The operator  $\hat{C}_{ml}$ , given by

$$\begin{aligned} \hat{C}_{ml}(\mathbf{R}) &= - \sum_I \frac{\hbar^2}{2M_I} \int d^3r \left[ \phi_m^*(\mathbf{r}, \mathbf{R}) \frac{\partial^2}{\partial \mathbf{R}_I^2} \phi_l(\mathbf{r}, \mathbf{R}) \right. \\ &\quad \left. + 2\phi_m^*(\mathbf{r}, \mathbf{R}) \left( \frac{\partial}{\partial \mathbf{R}_I} \phi_l(\mathbf{r}, \mathbf{R}) \right) \frac{\partial}{\partial \mathbf{R}_I} \right] , \end{aligned} \quad (1.16)$$

describes coupling between different electronic states  $(l, m)$ . This term is of the order  $(m/M)^{1/4} \approx 10^{-1} - 10^{-2}$  smaller than the nuclear energy [20]. Neglecting the coupling terms  $C_{ml}$  is known as the *Born-Oppenheimer (BO) approximation*.<sup>1</sup> Within this approximation, the dynamical evolution of electrons and nuclei is completely separated and the electrons can be pictured as moving *adiabatically* with the nuclei. The nuclear Schrödinger equation reduces to

$$\left( \hat{T}^{\text{Nuc}} + E_l^0(\mathbf{R}) \right) \chi_l(\mathbf{R}) = E \chi_l(\mathbf{R}) . \quad (1.17)$$

Solving this equation is performed in two steps:

1. For a given configuration  $\mathbf{R}$ , the electronic Schrödinger equation (1.13) is solved, yielding the energies  $E_l^0(\mathbf{R})$  which thereby parametrically depend on  $\mathbf{R}$ .
2. For each electronic quantum number  $l$ , Eq.(1.17) is solved, where the electronic energy  $E_l^0(\mathbf{R})$  defines the effective *potential-energy surface* for the nuclei.

SINCE WE WILL DEAL WITH INSULATORS AND SEMICONDUCTORS with bandgaps providing a sufficient energetic separation between the electronic ground state  $l = 0$  and the first excited state  $l = 1$ ,<sup>2</sup> we will concentrate on the electronic ground state energy  $E_0^0$  for the given configuration  $\mathbf{R}$  in the following. We denote this energy as the *Born-Oppenheimer potential energy*,

$$E^{\text{BO}}(\mathbf{R}) \equiv E_0^0(\mathbf{R}) . \quad (1.18)$$

<sup>1</sup> Born and Oppenheimer neglected  $C_{ml}$  in their original work [20] and later called this the *adiabatic approximation* [21]. However, only the terms  $C_{m \neq l}$  describe transitions between different electronic states induced by nuclear coupling, and keeping the terms  $C_{m=l}$  gives the exact potential when the electronic states are sufficiently separated, e. g., in presence of an electronic gap [22]. Therefore the term “adiabatic approximation” is nowadays used when only the terms  $C_{m=l}$  are kept [23]. The full BO approximation is correct to fourth order in the expansion of the full Hamiltonian in the mass parameter  $\sqrt[4]{m/M}$  [21]. Corrections to the forces arising from the  $C_{m=l}$  term can however be expected to be much smaller [24].

<sup>2</sup> Thermal energy at room temperature is  $\sim 25 \text{ meV} \ll \text{typical bandgap}$ .

### 1.3 Density Functional Theory

*"It is my sense that at the present time DFT is the method of choice for systems consisting of many ( $\gtrsim 5$ ) atoms and for smaller systems, when moderate accuracies are sufficient."*

W. Kohn, 1993

In the previous chapter, it was tacitly assumed that the electronic Schrödinger equation (1.13) yielding the effective potential for the nuclei can be solved. Finding an exact solution to this equation is, however, infeasible for more than a few electrons. We will now introduce *density functional theory* (DFT) as a framework for making approximations that enable to find a first-principles electronic potential-energy surface  $E^{\text{BO}}(\mathbf{R})$  for atomic systems with order of magnitudes more electrons.

To set the stage, we rewrite the electronic Schrödinger equation (1.13):

$$\hat{H} = \hat{T} + \hat{W} + \hat{V}^{\text{ext}}, \quad (1.19)$$

where  $\hat{T} \equiv \hat{T}^e$  denotes the electronic kinetic energy operator,  $\hat{W} \equiv \hat{V}^{e-e}$  is the electronic Coulomb repulsion, and  $\hat{V}^{\text{ext}} \equiv \hat{V}^{e-\text{Nuc}}$  is the *external* potential determined by the nuclear configuration  $\mathbf{R}$ . For the time being, the bare nuclear-nuclear repulsion  $\hat{V}^{\text{Nuc-Nuc}}$  is neglected as it merely contributes an additive constant to the electronic Hamiltonian at fixed configuration  $\mathbf{R}$ . We will restore this term again when looking at gradients of the total energy.

WE LOOK FOR SOLUTIONS to Eq. (1.19) of the form

$$\hat{H} |\Psi\rangle = E_\Psi |\Psi\rangle, \quad (1.20)$$

where  $\hat{H}$  is the electronic Hamiltonian given by Eq. (1.19),  $|\Psi\rangle$  denotes a many-body eigenstate in index-free bra–ket notation<sup>3</sup>, and  $E_\Psi$  is the corresponding total energy. The state  $|\Psi\rangle$  maps to an electron density  $n_\Psi(\mathbf{x})$  at a given point in space,  $\mathbf{x} \in \mathbb{R}^3$ , via the density operator

$$\hat{n}(\mathbf{x}) \equiv \sum_i \hat{n}_i(\mathbf{x}) = \sum_i \delta(\mathbf{x} - \hat{\mathbf{r}}_i), \quad (1.21)$$

such that

$$n_\Psi(\mathbf{x}) \equiv \langle \Psi | \hat{n}(\mathbf{x}) | \Psi \rangle = N \int d^3 r_2 \cdots d^3 r_N |\Psi(\mathbf{x}, \mathbf{r}_2, \dots, \mathbf{r}_N)|^2, \quad (1.22)$$

where it was used that the arguments of  $|\Psi(\mathbf{r}_1, \dots, \mathbf{r}_N)|^2$  can be arbitrarily permuted. The density operator  $\hat{n}(\mathbf{x})$  can be used to express the one-particle operator  $\hat{V}^{\text{ext}}$  as an operator valued functional of a potential function  $v^{\text{ext}}(\mathbf{x})$  by writing

$$\hat{V}^{\text{ext}} = \sum_i v^{\text{ext}}(\hat{\mathbf{r}}_i) = \int d^3 x v^{\text{ext}}(\mathbf{x}) \hat{n}(\mathbf{x}), \quad (1.23)$$

where  $v^{\text{ext}}(\mathbf{x})$  is the Coulomb potential stemming from the nuclear arrangement  $\mathbf{R}$ ,

$$v^{\text{ext}}(\mathbf{x}) = - \sum_J \frac{Z_J e^2}{|\mathbf{x} - \mathbf{R}_J|}. \quad (1.24)$$

<sup>3</sup> Here and in the following we employ the usual convention that many-body wavefunctions are obtained from the state  $|\Psi\rangle$  via

$$\begin{aligned} \langle \mathbf{r} | \Psi \rangle &= \Psi(\mathbf{r}) \\ \Leftrightarrow \langle \mathbf{r}_1, \dots, \mathbf{r}_N | \Psi \rangle &= \Psi(\mathbf{r}_1, \dots, \mathbf{r}_N). \end{aligned}$$

Likewise we define the scalar product as

$$\langle \Psi | \Phi \rangle = \int d^{3N} r \Psi^*(\mathbf{r}) \Phi(\mathbf{r}).$$

All functions are assumed to be sufficiently well-behaved such that the usual manipulations are mathematically well defined.

It follows that the expectation value of  $\hat{V}^{\text{ext}}$  is a functional of the density,

$$\langle \Psi | \hat{V}^{\text{ext}} | \Psi \rangle = V^{\text{ext}}[n_\Psi] = \int d^3x v^{\text{ext}}(\mathbf{x}) n_\Psi(\mathbf{x}). \quad (1.25)$$

Since the density  $n_\Psi$  is obtained from the solution  $|\Psi\rangle$  of Eq. (1.20) and the term  $\hat{V}^{\text{ext}}$  in the Hamiltonian given by Eq. (1.19) is solely determined by the external potential function  $v^{\text{ext}}(\mathbf{x})$  via Eq. (1.23), it follows that  $n_\Psi(\mathbf{r})$  is a functional of  $v^{\text{ext}}(\mathbf{x})$ . In other words, there is a map  $M$  between the set of external potentials  $\mathbb{V} = \{v^{\text{ext}}\}$  to the set of eigensolutions  $\mathbb{P} = \{\Psi\}$  and their corresponding densities  $\mathbb{N} = \{n_\Psi\}$ :

$$M : \mathbb{V} \rightarrow \mathbb{N}. \quad (1.26)$$

### 1.3.1 Hohenberg-Kohn Theorem

Hohenberg and Kohn were able to show that, for non-degenerate<sup>4</sup> ground states  $\Psi \equiv \Psi_0$ , there exists the *inverse map* from ground-state densities  $\mathbb{N}_0$  to potential functions  $\mathbb{V}$ , and that this map is bijective [26]:

$$M^{-1} : \mathbb{N}_0 \rightarrow \mathbb{V}. \quad (1.27)$$

The beauty of this theorem is that it establishes a one-to-one correspondence between the *ground-state density*  $n_0(\mathbf{x})$  and the external potential function  $v^{\text{ext}}(\mathbf{x})$  which, in turn, describes the full many-body problem via the Schrödinger equation. It follows that the ground-state wavefunctions  $\Psi_0$  are functionals of  $n_0$ , as well as the expectation value of any ground-state observable. Since we are only concerned with electronic ground-state densities in the following, we denote it simply by  $n(\mathbf{x}) \equiv n_0(\mathbf{x})$ .

HOHENBERG AND KOHN FURTHER DEFINE the *universal functional*

$$F[n] \equiv \langle \Psi[n] | \hat{T} + \hat{W} | \Psi[n] \rangle, \quad (1.28)$$

i. e., the contributions to the Hamiltonian which do not depend on the external potential. The ground-state total energy for a given potential function  $v^{\text{ext}}$  is then given as

$$E[n] = \langle \Psi[n] | \hat{H} | \Psi[n] \rangle \equiv F[n] + V^{\text{ext}}[n], \quad (1.29)$$

where  $V^{\text{ext}}[n]$  is given by Eq. (1.25). By virtue of the Raleigh-Ritz variational principle, this functional is minimized for the correct ground-state density  $n$  only, and any other density  $\rho$  that differs from  $n$  non-trivially yields a larger energy:

$$E[n] < E[\rho] \quad \text{for } n \neq \rho. \quad (1.30)$$

This also means that the true ground-state density for a given potential  $v^{\text{ext}}$  can be found by minimizing the total energy function, Eq. (1.29),

$$n = \arg \min_{\rho} E[\rho], \quad (1.31)$$

under the constraint of fixed particle number imposed by the Lagrange multiplier  $\mu$ ,

$$\frac{\delta}{\delta \rho(\mathbf{x})} \left[ E[\rho] + \mu \left( \int d^3x' \rho(\mathbf{x}') - N \right) \right] \Big|_{\rho=n} = 0. \quad (1.32)$$

<sup>4</sup> Kohn was later able to loosen the requirement of non-degeneracy [25].

## 1.4 The Born-Oppenheimer Surface

In the definition of the effective electronic Hamiltonian in Eq. (1.19), we had neglected the electrostatic nuclear repulsion  $V^{\text{Nuc-Nuc}}$  defined in Eq. (1.5). The Born-Oppenheimer potential-energy surface defined in Eq. (1.18) therefore consists of both terms, i. e.,

$$E^{\text{BO}}(\mathbf{R}) = E[n] + \sum_{I < J} \frac{Z_I Z_J e^2}{|\mathbf{R}_I - \mathbf{R}_J|}. \quad (1.33)$$

### 1.4.1 Hellmann-Feynmann Theorem

The forces on individual atomic positions  $\mathbf{R}_I$  are given in terms of derivatives of the Born-Oppenheimer energy,  $E^{\text{BO}}(\mathbf{R})$ ,

$$\frac{d}{d\mathbf{R}_I} E^{\text{BO}}(\mathbf{R}) \stackrel{(1.33)}{=} \frac{d}{d\mathbf{R}_I} \left[ E[n] + \sum_{J < K} \frac{Z_J Z_K e^2}{|\mathbf{R}_J - \mathbf{R}_K|} \right]. \quad (1.34)$$

The electronic part is given by

$$\frac{d}{d\mathbf{R}_I} E[n] = \underbrace{\frac{\partial}{\partial \mathbf{R}_I} E[n]}_{I} + \underbrace{\int d^3x \frac{\delta E[n]}{\delta n(\mathbf{x})} \frac{\partial n(\mathbf{x})}{\partial \mathbf{R}_I}}_{II}, \quad (1.35)$$

where term  $II$ ) can be evaluated under the assumption of stationarity expressed by Eq. (1.32) which yields  $\delta E[n]/\delta n(\mathbf{x}) = -\mu$ , and using the Leibniz rule,<sup>5</sup> so that

$$\int d^3x \frac{\delta E[n]}{\delta n(\mathbf{x})} \frac{\partial n(\mathbf{x})}{\partial \mathbf{R}_I} = -\mu \frac{d}{d\mathbf{R}_I} \int d^3x n(\mathbf{x}) = 0. \quad (1.36)$$

Term  $I$ ) only depends explicitly on  $\mathbf{R}_I$  via the electron-nucleus contribution to  $V^{\text{ext}}$ , i. e., in terms of the Coulomb kernel  $v^{\text{ext}}(\mathbf{x})$ ,

$$\frac{d}{d\mathbf{R}_I} E[n] = \frac{d}{d\mathbf{R}_I} \langle \Psi_0 | \hat{V}^{\text{ext}} | \Psi_0 \rangle = \int d^3x n(\mathbf{x}) \frac{Z_I e^2 (\mathbf{R}_I - \mathbf{x})}{|\mathbf{R}_I - \mathbf{x}|^3}. \quad (1.37)$$

In total, we have

$$\frac{d}{d\mathbf{R}_I} E^{\text{BO}}(\mathbf{R}) = \int d^3x n(\mathbf{x}) \frac{Z_I e^2 (\mathbf{R}_I - \mathbf{x})}{|\mathbf{R}_I - \mathbf{x}|^3} - \sum_{I \neq J} \frac{Z_I Z_J e^2 (\mathbf{R}_I - \mathbf{R}_J)}{|\mathbf{R}_I - \mathbf{R}_J|^3}, \quad (1.38)$$

which is solely determined by the ground-state electron density  $n(\mathbf{x})$  and the nuclear configuration  $\mathbf{R}$ . This result is known as the *Hellmann-Feynman theorem* [27, 28], which can also be formulated in more general terms for any parametric dependence of the Hamiltonian on some external quantity  $\lambda$ :

**Theorem** (Hellmann-Feynman).

$$\frac{dE_\lambda}{d\lambda} = \frac{d}{d\lambda} \langle \Psi_\lambda | \hat{H}_\lambda | \Psi_\lambda \rangle = \left\langle \Psi_\lambda \left| \frac{d\hat{H}_\lambda}{d\lambda} \right| \Psi_\lambda \right\rangle. \quad (1.39)$$

WHILE THE HELLMANN-FEYNMAN THEOREM IS FORMALLY CORRECT, in practice there often arise correction terms when non-complete basis sets are used that also depend on the parameter  $\lambda$ , or an approximation to the true ground-state density is used [29, 30]. In atomic-centered basissets, the most important correction terms are the so-called *Pulay forces* [31].

<sup>5</sup> Leibniz rule for parameter integrals:

$$\int dx \frac{\partial}{\partial y} f(x, y) = \frac{d}{dy} \int dx f(x, y).$$

## 1.5 Kohn-Sham Scheme

BY INTRODUCING DENSITY FUNCTIONAL THEORY, we have not solved the many-body problem. However, we have shifted the intricacies of this problem to a *universal* functional  $F[n]$  which depends on the electron density  $n(\mathbf{x})$ . Since the density is a scalar function of three coordinates,  $n : \mathbb{R}^3 \rightarrow \mathbb{R}$ , this entails a massive reduction of complexity compared to working with wavefunctions, which are complex functions of  $3N$  variables,  $\Psi : \mathbb{R}^{3N} \rightarrow \mathbb{C}$ . In order to proceed, we follow the original argument by Kohn and Sham [32] and investigate the universal functional  $F[n]$  in more detail. The definition reads

$$F[n] = \langle \Psi[n] | \hat{T} + \hat{W} | \Psi[n] \rangle \equiv T[n] + W[n], \quad (1.40)$$

where  $T[n]$  denotes the kinetic energy of the electrons expressed as a functional of the density  $n(\mathbf{x})$ , and  $W[n]$  denotes the electron-electron interaction term as before. We split this term into two contributions,

$$\begin{aligned} W[n] &= E^{\text{es}}[n] + E^{\text{xc}}[n] \\ &= \frac{1}{2} \int d^3x v^{\text{es}}[n](\mathbf{x}) n(\mathbf{x}) + E^{\text{xc}}[n], \end{aligned} \quad (1.41)$$

where  $E^{\text{es}}[n]$  is the electrostatic (Hartree) energy stemming from the charge distribution  $n(\mathbf{x})$  in the Coulomb potential

$$v^{\text{es}}[n](\mathbf{x}) = \int d^3x' \frac{n(\mathbf{x}')}{|\mathbf{x} - \mathbf{x}'|}, \quad (1.42)$$

which is a functional of the density itself.  $E^{\text{xc}}[n]$  denotes all exchange and correlation effects not captured by  $E^{\text{es}}[n]$  and is therefore termed the *exchange-correlation energy*. Again, we have only shifted the problem, this time to the unknown functional  $E^{\text{xc}}[n]$  which we will discuss later. In this notation, the total energy functional for the electron system in an external potential reads

$$E[n] = T[n] + E^{\text{es}}[n] + E^{\text{xc}}[n] + V^{\text{ext}}[n]. \quad (1.43)$$

Let us now define the density  $n(\mathbf{x})$  in terms of an *auxiliary* orthonormal set of complex functions  $\{\psi_l(\mathbf{x})\}$ , such that

$$n(\mathbf{x}) = \sum_l f_l |\psi_l(\mathbf{x})|^2, \quad (1.44)$$

where the  $f_l$  denote the occupation of each orbital, i. e., a Fermi-like function that represents a thermal ensemble or the 0 K ground state.<sup>6</sup> We use Eq. (1.44) in Eq. (1.43) and vary with respect to  $\psi_l^*(\mathbf{x})$  under the constraint of keeping the functions  $\{\psi_l\}$  normalized via the Lagrange multiplier  $\lambda_l$ ,

$$\frac{\delta}{\delta \psi_l^*(\mathbf{x})} \left[ T[n] + E^{\text{es}}[n] + E^{\text{xc}}[n] + V^{\text{ext}}[n] - \lambda_l \left( \int d^3x |\psi_l(\mathbf{x})|^2 - 1 \right) \right] = 0. \quad (1.45)$$

By Eq. (1.44) we have

$$\frac{\delta n(\mathbf{x})}{\delta \psi_l^*(\mathbf{x}')} = f_l \psi_l(\mathbf{x}) \delta(\mathbf{x} - \mathbf{x}'), \quad (1.46)$$

<sup>6</sup> The occupations are  $f_l \in [0, 1]$  when the spin is treated explicitly, otherwise the spin degeneracy can be accounted for by allowing  $f_l \in [0, 2]$ .

and therefore by chain rule  $\delta/\delta\psi^* = (\delta n/\delta\psi^*)\delta/\delta n$ , so that

$$\left(-\frac{1}{2}\nabla^2 + v^{\text{es}}[n](\mathbf{x}) + v^{\text{xc}}[n](\mathbf{x}) + v^{\text{ext}}(\mathbf{x})\right)\psi_l(\mathbf{x}) = \frac{\lambda_l}{f_l}\psi_l(\mathbf{x}) . \quad (1.47)$$

Here,  $-\frac{1}{2}\nabla^2$  is the kinetic operator,  $v^{\text{es}}$  and  $v^{\text{ext}}$  are the electrostatic and external potentials defined earlier, and

$$v^{\text{xc}}[n](\mathbf{x}) = \frac{\delta E^{\text{xc}}[n]}{\delta n(\mathbf{x})} \quad (1.48)$$

is the *exchange-correlation potential* formally defined as the functional derivative of  $E^{\text{xc}}[n]$  with respect to the density. By summarizing the three potentials entering Eq. (1.47) as one *effective* potential,

$$v^{\text{eff}}[n](\mathbf{x}) \equiv v^{\text{es}}[n](\mathbf{x}) + v^{\text{xc}}[n](\mathbf{x}) + v^{\text{ext}}(\mathbf{x}) , \quad (1.49)$$

and denoting  $\epsilon_l \equiv \lambda_l/f_l$ , we can write

$$\left(-\frac{1}{2}\nabla^2 + v^{\text{eff}}[n](\mathbf{x})\right)\psi_l(\mathbf{x}) = \epsilon_l\psi_l(\mathbf{x}) . \quad (1.50)$$

This is a set of one-particle Schrödinger-like equations for the orbitals  $\psi_l$  with eigenvalues  $\epsilon_l$  in an effective potential  $v^{\text{eff}}[n]$  called *Kohn-Sham equations*. The *Kohn-Sham theorem* ensures that, for any external potential  $v^{\text{ext}}$ , there exists a *unique* effective potential  $v^{\text{eff}}[n]$  which yields *non-interacting* single-particle orbitals  $\psi_l$  that reproduce the ground-state density  $n$  of the *interacting* many-particle system [32, p. 51].

**THE EFFECTIVE POTENTIAL ITSELF IS A FUNCTIONAL OF THE DENSITY  $n$**  given in terms of the orbitals by Eq. (1.44), the Kohn-Sham equations therefore need to be solved *self-consistently*: One starts from an initial guess for the density  $n^0$  to set up the effective potential, and solves for  $(\psi_l, \epsilon_l)$ . From the solution, an updated density  $n^1$  is computed via Eq. (1.44). The procedure is repeated until the density residual  $\delta n^i = \|n^i - n^{i-1}\|$  is smaller than the desired precision.

**WHEN THE SOLUTION  $\{\psi_l, \epsilon_l\}$  IS KNOWN**, Eq. (1.50) can be used to express the kinetic energy in terms of the density  $n$  and eigenvalues  $\epsilon_l$  by summing and integrating with  $\sum_l \int d^3x \psi_l^*(\mathbf{x})$  and using the orthonormality of the orbitals  $\psi_l$ , so that

$$T[n] \equiv -\frac{1}{2} \sum_l \int d^3x \psi_l^*(\mathbf{x}) \nabla^2 \psi_l(\mathbf{x}) \stackrel{(1.50)}{=} \sum_l \epsilon_l - \int d^3x v^{\text{eff}}[n](\mathbf{x}) n(\mathbf{x}) , \quad (1.51)$$

thereby eliminating the Kohn-Sham orbitals  $\psi_l$  from the expression. The total energy in terms of the Kohn-Sham eigenvalues  $\{\epsilon_l\}$  and density  $n(\mathbf{x}) = \sum_l |\psi_l(\mathbf{x})|^2$  is then given as

$$E[n] \stackrel{(1.51)}{=} \sum_l \epsilon_l - \frac{1}{2} \int d^3x v^{\text{es}}[n](\mathbf{x}) n(\mathbf{x}) + E^{\text{xc}}[n] - \int d^3x v^{\text{xc}}[n](\mathbf{x}) n(\mathbf{x}) . \quad (1.52)$$

Remember that

$$E[n] = T[n] + E^{\text{es}}[n] + E^{\text{xc}}[n] + V^{\text{ext}}[n] ,$$

and

$$v^{\text{eff}}[n](\mathbf{x}) = v^{\text{es}}[n](\mathbf{x}) + v^{\text{xc}}[n](\mathbf{x}) + v^{\text{ext}}(\mathbf{x}) .$$

## 1.6 Approximations to the exchange-correlation energy

We are finally in position to introduce approximations to the exchange-correlation energy functional  $E^{xc}[n]$  from which the corresponding potential can be obtained by the functional derivative with respect to the density. Indeed, the very success of the Kohn-Sham DFT scheme can most likely be traced back to the fact that simple approximations to  $E^{xc}[n]$  lead to reasonable results for a large class of systems.

### 1.6.1 Local Density Approximation (LDA)

LET US NOW DEFINE an exchange-correlation energy density  $e^{xc}[n](\mathbf{x})$  via

$$E^{xc}[n] = \int d^3x e^{xc}[n](\mathbf{x}), \quad (1.53)$$

where the density is a functional of the density by itself. The most straightforward way to approximate  $e^{xc}[n](\mathbf{x})$  is to replace the *functional*  $e^{xc}[n](\mathbf{x})$  by a *function* of the local density,

$$e^{xc}[n](\mathbf{x}) \approx e_{\text{LDA}}^{xc}(n(\mathbf{x})). \quad (1.54)$$

This approximation is called the *local density approximation* (LDA), and the resulting exchange-correlation energy reads

$$E_{\text{LDA}}^{xc}[n] = \int d^3x e_{\text{LDA}}^{xc}(n(\mathbf{x})). \quad (1.55)$$

The energy density  $e_{\text{LDA}}^{xc}(n(\mathbf{x}))$  is usually taken to be the exchange-correlation energy density of a homogeneous electron gas obtained from higher-level theory approaches [33].<sup>7</sup> The LDA is (by construction) exact in the limit of vanishing density gradient,  $|\nabla n(\mathbf{x})|/n(\mathbf{x}) \rightarrow 0$ , but yields surprisingly good results under circumstances where the density is non-homogeneous as well [35, p. 183].

### 1.6.2 Generalized Gradient Approximation (GGA)

IN THE SPIRIT OF THE ORIGINAL WORK by Hohenberg and Kohn, and Kohn and Sham, improvements on the LDA can be constructed by going beyond the local density and taking into account gradients of the density as well,

$$e^{xc}[n](\mathbf{x}) \approx e_{\text{GGA}}^{xc}(n(\mathbf{x}), \nabla n(\mathbf{x})). \quad (1.56)$$

Again, the full functional  $e^{xc}[n]$  is replaced by a function of the density and its gradient. This approximation is called *generalized gradient approximation* (GGA), and the resulting energy is usually written in the form

$$E_{\text{GGA}}^{xc}[n] = \int d^3x e_{\text{hom}}^x(n(\mathbf{x})) F^{xc}(n(\mathbf{x}), |\nabla n(\mathbf{x})|), \quad (1.57)$$

where  $e_{\text{hom}}^x(n)$  is the exchange energy density of a homogeneous electron gas, and  $F^{xc}(n, \nabla n)$  is an *enhancement factor* [36].

Remember

$$v^{xc}[n](\mathbf{x}) = \frac{\delta E^{xc}[n]}{\delta n(\mathbf{x})}.$$

Some authors prefer to write  $e^{xc}(n) = n \tilde{e}^{xc}(n)$ , such that

$$E^{xc} = \int d^3x n(\mathbf{x}) \tilde{e}^{xc}(n(\mathbf{x})).$$

<sup>7</sup> Depending on the application, it can be beneficial to parametrize LDA on other reference system [34].

THE GENERALIZED GRADIENT APPROXIMATION IS OFTEN A GOOD COMPROMISE between accuracy and numerical cost when studying nuclear dynamics of solids, and we will use this approximation throughout the work. However, when studying electronic properties including excitations, one often needs to use more sophisticated approximation schemes [37, 38].

## 1.7 Periodic Systems

**REM:** Duplicate of the phonon part, maybe just introduce BvK boundary conditions – or don't mention at all?

So far, we did not specify the external potential  $v^{\text{ext}}(\mathbf{x})$  entering the Kohn-Sham equation (1.47) beyond stating that it describes the arrangement of nuclei. For (finite) molecules and clusters, this is already sufficient and a self-consistent solution to Eq. (1.47) can be attempted from here. For (practically infinite) bulk systems and crystals on the other hand, further assumptions need to be made.

Let us assume that the configuration of the nuclei is in a perfect periodic arrangement described by the *Bravais vectors*

$$\mathbf{R}_n = \sum_{i=1}^3 n^i \mathbf{a}_i , \quad (1.58)$$

where  $\{ \mathbf{a}_i \}$  are *lattice vectors* that span the *unit cell*,

$$\mathbb{V}_{\text{uc}} = \{ \mathbf{x} = f^i \mathbf{a}_i : f^i \in \mathbb{R}^{[-0.5,0.5]} \} , \quad (1.59)$$

and the full crystal is spanned by the unit cell translated by all possible translations  $\mathbf{R}_n$  given by Eq. (1.58) with integer numbers  $n_i \in \mathbb{Z}$ . The periodicity of the crystal is characterized by the condition that any translation by  $\mathbf{R}_n$  maps the crystal back onto itself such that

$$v^{\text{ext}}(\mathbf{x} + \mathbf{R}_n) = v^{\text{ext}}(\mathbf{x}) . \quad (1.60)$$

By definition of the effective potential entering the Kohn-Sham equations (1.50),  $v^{\text{eff}}[n](\mathbf{x})$  shares this periodicity. We can therefore formulate a *Bloch theorem*<sup>8</sup> for the Kohn-Sham orbitals  $\psi_l(\mathbf{x})$ , i. e., solutions to Eq. (1.50) can be separated into independent equations labelled by a quantum number  $\mathbf{k}$  with solutions

$$\psi_{\mathbf{k}l}(\mathbf{x}) = e^{i\mathbf{k}\cdot\mathbf{x}} u_{\mathbf{k}l}(\mathbf{x}) \quad (1.61)$$

where  $u_{\mathbf{k}l}$  are periodic functions satisfying

$$u_{\mathbf{k}l}(\mathbf{x} + \mathbf{R}_n) = u_{\mathbf{k}l}(\mathbf{x}) , \quad (1.62)$$

and  $\mathbf{k}$  is restricted to the first Brillouin zone of the reciprocal lattice.

To ensure normalizability of the functions  $\psi_{\mathbf{k}l}$ , one additionally imposes the *Born-von Karman boundary conditions*

$$\psi_{\mathbf{k}l}(\mathbf{x} + N_i \mathbf{a}_i) = \psi_{\mathbf{k}l}(\mathbf{x}) \quad (1.63)$$

where  $N_i$  denotes the number of repetitions along direction  $\mathbf{a}_i$ . The domain  $V$  of all functions and functionals appearing the Kohn-Sham equations thereby becomes a parallelepiped of size  $V = N_1 N_2 N_3 \mathbf{a}_1 \cdot (\mathbf{a}_2 \times \mathbf{a}_3)$  with periodically connected edges. The ideal, infinite crystal is obtained in the limit  $N_i \rightarrow \infty$ . Using the periodic boundary condition expressed by Eq. (1.63) in the Bloch functions given by Eq. (1.61), and the periodicity of the functions  $u_{\mathbf{k}l}$ , one finds that

$$\mathbf{k} \cdot \mathbf{a}_i = \frac{2\pi}{N_i} m_i , \quad \text{with } m_i \in \mathbb{N}^{[0, N_i)} . \quad (1.64)$$

<sup>8</sup> Cf. Sec. B.1 for an informal proof.

In total there are  $N = N_1 N_2 N_3$  unique values of  $\mathbf{k}$  labelled by  $\mathbf{m} = (m_1, m_2, m_3)$  that can be expressed in terms of the *reciprocal lattice vectors* [39]

$$\mathbf{b}^i = 2\pi \varepsilon^{ijk} \frac{\mathbf{a}_j \times \mathbf{a}_k}{\mathbf{a}_1 \cdot (\mathbf{a}_2 \times \mathbf{a}_3)}, \quad (1.65)$$

where  $\varepsilon^{ijk}$  denotes the Levi-Civita symbol enforcing the correct ordering of  $ijk$ . The complete set of  $\mathbf{k}$ -values sampled in a simulation box of the given size, i. e., the *Born-von Karman cell*, is

$$\mathbf{k}_m = \sum_{i=1}^3 \frac{m_i}{N_i} \mathbf{b}^i. \quad (1.66)$$

The space spanned by the  $\{\mathbf{b}_i\}$ , i. e., the space containing all unique values of  $\mathbf{k}$ , is the unit cell of the reciprocal lattice. Alternatively, one chooses those equivalent  $\mathbf{k}_m$  which are closest to the  $\mathbf{0}$ , i. e., the Brillouin zone.

## 1.8 Conclusion

The concept of density functional theory in the Kohn-Sham scheme (KS-DFT) has been presented starting from the general, many-body Hamiltonian given in Eq. (1.1). Besides the Born-Oppenheimer (BO) approximation which decouples electron and nuclear dynamics, KS-DFT offers a formally exact way of computing the non-relativistic total energy of the electronic ground state from first principles by solving the Kohn-Sham equations, a set of Schrödinger-like single-particle equations, for an auxiliary set of functions, i. e., the Kohn-Sham orbitals. In order to solve the Kohn-Sham equations one needs to approximate the exchange-correlation energy,  $E^{xc}[n]$ . In Sec. 1.6 we have introduced the most common approaches to approximate  $E^{xc}[n]$ : The local-density approximation (LDA), as well as the generalized-gradient approximation (GGA). In this framework, the BO potential-energy surface defined in Eq. (1.18) is given by the total energy obtained by (semi-)local KS-DFT. In the next chapter, we discuss how the BO potential-energy surface determines the dynamical properties of the nuclear system.

## 2

# Nuclear and Lattice Dynamics

In the previous chapter, we have seen how the many-body problem can be decoupled into an electronic problem which can be solved in the framework of DFT, and a nuclear problem that describes the dynamical properties of the nuclei. This was achieved by means of the Born-Oppenheimer approximation where electron-nucleus interactions beyond a parametric dependence on each other are neglected [20].

WE WILL NOW APPROACH the description of the nuclear dynamics from two sides: First, we introduce the *harmonic approximation* in which the nuclear Schrödinger equation is solved for an approximated potential in terms of vibrational eigenmodes. We will use the opportunity to discuss extended systems, in particular crystalline systems with long-range order. Second, we treat the nuclei as *classical* particles on the full, non-truncated Born-Oppenheimer potential  $E^{\text{BO}}(\mathbf{R})$ . This will lead to the formulation of *ab initio molecular dynamics* (aiMD). In a last step, we will connect the two approaches to allow for extracting phonon properties from MD simulations. As no electron will appear anymore,  $N \equiv N_{\text{Nuc}}$  will henceforth denote the number of nuclei in the system of interest, and we denote the Born-Oppenheimer potential simply as *the* potential,  $E^{\text{BO}}(\mathbf{R}) \equiv \mathcal{V}(\mathbf{R})$ .

TO SET THE STAGE, WE RECALL THE SCHRÖDINGER EQUATION for the nuclear wavefunction  $\chi(\mathbf{R})$  corresponding to the electronic ground state as initially defined in Eq. (1.17),

$$(\mathcal{T} + \mathcal{V}(\mathbf{R}) - E) \chi(\mathbf{R}) = 0, \quad (2.1)$$

where

$$\mathcal{T} = \sum_I \frac{-\hbar^2}{2M_I} \frac{\partial^2}{\partial \mathbf{R}_I^2}, \quad (2.2)$$

is the nuclear kinetic-energy operator as before.

## 2.1 Harmonic Approximation

The Born-Oppenheimer potential  $\mathcal{V}(\mathbf{R})$  appearing in Eq.(2.1) is an ordinary function of the  $3N$  coordinates  $\mathbf{R} = (\mathbf{R}_1, \dots, \mathbf{R}_N)$  and therefore can be expanded as a Taylor series in displacements  $\mathbf{U} \equiv \Delta\mathbf{R}$  about a given configuration  $\mathbf{R}^0$ , i.e.,

$$\begin{aligned}\mathcal{V}(\mathbf{R} = \mathbf{R}^0 + \mathbf{U}) &= \mathcal{V}(\mathbf{R}^0) + \sum_{I,\alpha} \frac{\partial \mathcal{V}(\mathbf{R})}{\partial R_I^\alpha} \Big|_{\mathbf{R}^0} U_I^\alpha \\ &\quad + \frac{1}{2} \sum_{\substack{I,J \\ \alpha,\beta}} \frac{\partial^2 \mathcal{V}(\mathbf{R})}{\partial R_I^\alpha \partial R_J^\beta} \Big|_{\mathbf{R}^0} U_I^\alpha U_J^\beta \\ &\quad + \frac{1}{3!} \dots,\end{aligned}\quad (2.3)$$

where the expansion coefficients are called *force constants*. In particular, we have the *harmonic force constants*

$$\Phi_{I\alpha,J\beta} \equiv \frac{\partial^2 \mathcal{V}(\mathbf{R})}{\partial R_I^\alpha \partial R_J^\beta} \Big|_{\mathbf{R}^0}. \quad (2.4)$$

The harmonic approximation is typically used to assess dynamical properties of a system in some confined phase-space region close to a (local) minimum of the potential-energy surface.<sup>1</sup> A local minimum configuration  $\mathbf{R}^0$  is characterized by

$$\frac{\partial V(\mathbf{R})}{\partial R_I^\alpha} \Big|_{\mathbf{R}^0} = 0 \quad \text{for all } (I, \alpha), \text{ and} \quad (2.5)$$

$$\sum_{\substack{I,J \\ \alpha,\beta}} \Phi_{I\alpha,J\beta} U_I^\alpha U_J^\beta > 0 \quad \text{for all possible } \{ \mathbf{U}_I \}. \quad (2.6)$$

The condition in Eq.(2.6) is satisfied when the harmonic force constants  $\Phi_{I\alpha,J\beta}$  are positive-definite. It needs to be fulfilled to make the Hamiltonian bounded. Details on how to obtain force constants numerically are given in appendix D.

WE DEFINE MASS-REDUCED COORDINATES for the displacements,

$$\mathbf{u}_I \equiv \sqrt{M_I} \mathbf{U}_I, \quad (2.7)$$

$$\mathbf{p}_I \equiv -i\hbar \frac{\partial}{\partial \mathbf{u}_I}, \quad (2.8)$$

$$D_{I\alpha,J\beta} \equiv \frac{1}{\sqrt{M_I M_J}} \Phi_{I\alpha,J\beta}, \quad (2.9)$$

where Eq.(2.9) defines the *dynamical matrix* D.<sup>2</sup> Expressed in the mass-reduced coordinates  $\mathbf{u} = \{ \mathbf{u}_I \}$  and  $\mathbf{p} = \{ \mathbf{p}_I \}$ , the harmonic Hamiltonian reads

$$\begin{aligned}\mathcal{H}^{(2)}(\mathbf{p}, \mathbf{u}) &= \mathcal{T}(\mathbf{p}) + \mathcal{V}^{(2)}(\mathbf{u}) \\ &= \frac{1}{2} \sum_I \mathbf{p}_I^2 + \frac{1}{2} \sum_{\substack{I,J \\ \alpha,\beta}} D_{I\alpha,J\beta} u_I^\alpha u_J^\beta.\end{aligned}\quad (2.10)$$

Remember  $N \equiv N_{\text{Nuc}}$ .

<sup>1</sup> See section E.1 in the appendix for details on geometry optimization in the context of crystal lattices.

<sup>2</sup> There seems to be no general agreement that the matrix D, i.e., the mass-weighted force constants, are called “dynamical matrix”, or if this term is reserved for the Fourier transformed matrices studied in periodic systems. However, we follow Born and Huang in using the term dynamical matrix irrespective of the question of lattice periodicity [21, p. 173].

AS REQUIRED EARLIER, THE DYNAMICAL MATRIX  $D$  IS A POSITIVE DEFINITE MATRIX. Furthermore, we see from Eq. (2.4) that  $D$  is symmetric in the  $3N$  coordinates  $(I, \alpha)$  by the differentiability of the underlying potential  $\mathcal{V}(\mathbf{R})$ ,

$$D_{I\alpha, J\beta} = D_{J\beta, I\alpha} . \quad (2.11)$$

The eigenvalues of  $D$  will therefore be real and positive, and the eigenvectors will be real and orthogonal. We denote the eigensolutions as *modes* labeled by  $s$ , with eigenvalues  $\omega_s^2$ , and the normalized eigenvectors are  $\mathbf{e}_s = \{ \mathbf{e}_{s,I} \}$ . The dynamical matrix elements can be rewritten in terms of the eigenvectors and eigenvalues as

$$D_{I\alpha, J\beta} = \sum_s \omega_s^2 e_{s,I\alpha} e_{s,J\beta} , \quad (2.12)$$

and the eigenvectors fulfill

$$\sum_{I\alpha} e_{s,I\alpha} e_{s',I\alpha} = \delta_{ss'} \quad \text{and} \quad \sum_s e_{s,I\alpha} e_{s,J\beta} = \delta_{IJ} \delta_{\alpha\beta} . \quad (2.13)$$

Using the dynamical matrix elements expressed in terms of eigenvectors and eigenvalues, Eq. (2.12), the harmonic Hamiltonian as defined in Eq. (2.10) can be rewritten as

$$\mathcal{H}^{(2)}(\mathbf{p}, \mathbf{u}) = \frac{1}{2} \sum_s p_s^2 + \frac{1}{2} \sum_s \omega_s^2 u_s^2 . \quad (2.14)$$

Here, we implicitly defined the  $3N$  *normal coordinates*  $u_s$  and their conjugate momenta  $p_s$  via the orthogonal transformation<sup>3</sup>

$$u_s = \sum_I \mathbf{e}_{s,I} \cdot \mathbf{u}_I , \quad \text{and} \quad (2.15)$$

$$p_s = \sum_I \mathbf{e}_{s,I} \cdot \mathbf{p}_I . \quad (2.16)$$

<sup>3</sup> Using vector notation

$$\mathbf{e}_{s,I} \cdot \mathbf{u}_I = \sum_\alpha e_{s,I\alpha} u_I^\alpha .$$

The Hamiltonian expressed in terms of the normal coordinates, Eq. (2.14), contains no cross-terms between different modes  $s$  and  $s'$ . Rewritten in terms of this Hamiltonian, the wave equation (2.1) reads

$$\left\{ \frac{1}{2} \sum_s p_s^2 + \frac{1}{2} \sum_s \omega_s^2 u_s^2 - E \right\} \chi(\mathbf{u}) = 0 \quad (2.17)$$

Since the Hamiltonian is a sum of terms, each depending on one coordinate only, the total bosonic nuclear wavefunction  $\chi$  can be separated into a product of wavefunctions for each mode [21, p. 175],

$$\chi(\mathbf{u}) = \prod_s \chi_s(u_s) . \quad (2.18)$$

We end up with a set of  $3N$  uncoupled equations, one for each mode  $s$ :

$$\left\{ \frac{1}{2} (p_s^2 + \omega_s^2 u_s^2) - E_s \right\} \chi_s(u_s) = 0 , \quad (2.19)$$

where the total energy of the nuclei is the sum of each mode contribution  $E = \sum_s E_s$ . Equation (2.19) is the familiar equation for a harmonic oscillator of frequency  $\omega_s$  [40], thereby establishing  $\omega_s$  as the *eigenfrequency* of the

mode  $s$ . Permissible solutions are labeled by the integer  $n_s \in \mathbb{N}_0$  and the eigenvalue  $E_s$  depends on  $n_s$  via

$$E_s(n_s) = \hbar\omega_s \left( n_s + \frac{1}{2} \right). \quad (2.20)$$

The state of the entire system is therefore specified by the  $3N$  quantum numbers  $\mathbf{n} = (n_1, \dots, n_{3N})$ , and the total energy of the system is

$$E(\mathbf{n}) = \sum_s \hbar\omega_s \left( n_s + \frac{1}{2} \right). \quad (2.21)$$

This derivation is generally valid for a system of  $N$  particles described by a potential-energy surface of which a (local) minimum  $\mathbf{R}^0$ , and the matrix of second derivatives at this configuration,  $\Phi_{IJ}$ , is known. The thermodynamic properties of such a system of harmonic oscillators follow from this spectrum in straightforward fashion [21].

## 2.2 Extended Systems

**REM:** Move up, include discussion of symmetry beyond translational

The expressions presented in the previous section are generally valid for a system of  $N$  nuclei. Macroscopic materials, however, consist of  $\sim 10^{23}$  atoms. From a microscopic point of view, this number is virtually infinite, and mathematically described by the *bulk limit*  $N \rightarrow \infty$ . The most common way to deal with this bulk limit is to impose *periodic boundary conditions* on a finite region of space, i. e., a *generating volume*, and normalize the quantities of interest to this volume [21]. This procedure can be adopted for extended system such as liquids, amorphous solids such as glasses, and crystals. Since we are interested in the special case of crystals with an inherent periodic long-range order throughout this work, it is beneficial to first introduce the concept of a *crystal lattice* that describes a bulk crystal in terms of a *unit cell* arranged periodically in three dimensional space [41]. The periodic boundary conditions are then imposed on a generating volume containing several unit cells, i. e., a *supercell*.

### 2.2.1 Periodic systems: Crystals

The crystalline state is characterized by a periodic long-range order of the potential energy  $\mathcal{V}(\mathbf{R})$ . We describe this order in terms of the *Bravais vectors*

$$\mathbf{L} = L^\mu \mathbf{a}_\mu \quad \text{with} \quad L^\mu \in \mathbb{Z}, \quad (2.22)$$

where  $\{\mathbf{a}_\mu\}$  are *lattice vectors* spanning the unit cell of the crystal.<sup>4</sup> The Bravais vectors  $\mathbf{L}$  span a regular grid, i. e., a *lattice*, and are therefore also called *lattice points*.

<sup>4</sup> Notation: We index components in the crystal basis  $\{\mathbf{a}_\mu\}$  with  $\mu, \nu$ , as opposed to Cartesian components indexed by  $\alpha, \beta$ .

THE INVARIANCE OF THE POTENTIAL ENERGY UNDER TRANSLATIONS BY ARBITRARY BRAVAIS VECTORS  $\mathbf{L}$  is defined as follows: Let  $\mathbf{R} = \{\mathbf{R}_I\}$  be a configuration of atoms, and let  $\mathbf{R}' = \{\mathbf{R}'_I\}$  denote the configuration obtained by moving all atoms by a Bravais vector  $\mathbf{L}$ ,

$$\mathbf{R}'_I = \mathbf{R}_I + \mathbf{L}. \quad (2.23)$$

As a prerequisite for  $\mathcal{V}(\mathbf{R})$  to be translationally invariant, we require that  $\mathbf{R}^0 = \{\mathbf{R}_I^0\}$  are minimum configurations of the potential both before and after translating the system by  $\mathbf{L}$ , and there is a bijective permutation map  $P_{\mathbf{L}}$  between the atomic positions  $\mathbf{R}_I^0$  and  $\mathbf{R}'_I$ , which fulfills

$$P_{\mathbf{L}} : I \rightarrow I' \quad \text{such that} \quad \mathbf{R}_I^0 = \mathbf{R}_{I'}^0. \quad (2.24)$$

This statement is equivalent to requiring that the configurations  $\mathbf{R}_I^0$  and  $\mathbf{R}'_I$  are indistinguishable.<sup>5</sup> The final requirement for translational invariance of the potential is that the potential energy for *any* configuration differing by a Bravais vector is unchanged,

$$\mathcal{V}(\mathbf{R}' = \{\mathbf{R}_I + \mathbf{L}\}) = \mathcal{V}(\mathbf{R} = \{\mathbf{R}_I\}) \quad \text{for all} \quad \mathbf{L} = L^\mu \mathbf{a}_\mu, \quad (2.25)$$

i. e., not just at the minimum. This effectively corresponds to a permutation of the displacements of the atoms,  $U_I \rightarrow U_{I'}$  according to  $P_{\mathbf{L}}$  defined in

<sup>5</sup> This requirement is obviously not fulfilled for molecules, where rigidly shifting all atoms can by no means induce a permutation map between atoms.

Eq. (2.24). Figure 2.1 shows a one-dimensional depiction of the relation between discrete translation by Bravais vectors and the permutation map.

We can draw important conclusions from Eq. (2.24) and (2.25). First, the existence of the map  $P_{\mathbf{L}}$  enables us to write every atomic coordinate  $\mathbf{R}_I$  as

$$\mathbf{R}_I \equiv \mathbf{R}_{i\mathbf{L}} = \mathbf{R}_{i\mathbf{L}}^0 + \mathbf{U}_{i\mathbf{L}} = \mathbf{R}_i^0 + \mathbf{L} + \mathbf{U}_{i\mathbf{L}}, \quad (2.26)$$

where  $\mathbf{R}_i^0$  labels the position of an equivalent reference atom in the unit cell,  $\mathbf{U}_{i\mathbf{L}}$  is the displacement of the atom from its equilibrium position, and  $\mathbf{L}$  is a Bravais vector as before. We can therefore split the index  $I$  into the tuple

$$I = (i, \mathbf{L}), \quad (2.27)$$

where  $i$  labels the atom in the unit cell, and  $\mathbf{L}$  is the corresponding lattice point. Likewise, the forceconstants  $\Phi_{I\alpha, J\beta}$  can be written as  $\Phi_{i\mathbf{L}\alpha, j\mathbf{K}\beta}$ , where  $\mathbf{L}$  and  $\mathbf{K}$  are the Bravais vectors belonging to  $I$  and  $J$ , respectively. From the translational invariance of the potential, Eq. (2.25), we see that the forceconstants have to fulfill

$$\Phi_{i\mathbf{L}+\mathbf{M}\alpha, j\mathbf{K}+\mathbf{M}\beta} = \Phi_{i\mathbf{L}\alpha, j\mathbf{K}\beta}, \quad (2.28)$$

where  $\mathbf{M} = M^\mu \mathbf{a}_\mu$  with integers  $M^\mu$  denotes an arbitrary Bravais vector. The translational invariance holds likewise for the dynamical matrix  $D_{IJ} = \frac{1}{\sqrt{M_I M_J}} \Phi_{IJ}$ . The translational invariance expressed, e. g., by Eq. (2.28) can be regarded as the *intrinsic* periodicity of the system.

## 2.2.2 Periodic boundary conditions

In the previous section, we did not specify the system beyond requiring periodicity in space, and implicitly assumed an infinite crystal in the limit  $N \rightarrow \infty$  without boundaries. In practice we introduce Born-von Karman cyclic boundary conditions [42], as already done in Sec. 1.7 for the description of electronic states, but reintroduce them here in a slightly more general fashion.

WE DEFINE THE BOUNDARY CONDITIONS for the nuclear problem such that

$$\mathbf{R}_I + S^\mu \mathbf{A}_\mu = \mathbf{R}_I \quad \text{with} \quad S^\mu \in \mathbb{Z}, \quad (2.29)$$

where each  $\mathbf{A}_\mu$  is a linear combination of the primitive basis vectors  $\{\mathbf{a}_\nu\}$ ,

$$\mathbf{A}_\mu = M_\mu^{\text{sc}, \nu} \mathbf{a}_\nu \quad \text{with} \quad M_\mu^{\text{sc}, \nu} \in \mathbb{Z}, \quad (2.30)$$

and  $M^{\text{sc}}$  is a non-singular matrix with integer elements. The space spanned by the  $\{\mathbf{A}_i\}$  is a parallelepiped of volume  $V_{\text{sc}} = N_{\mathbf{q}} V_{\text{uc}}$ , where  $N_{\mathbf{q}} = \det M^{\text{sc}}$  is the number of lattice points that fit into the enlarged cell,<sup>6</sup> and  $V_{\text{uc}} = \mathbf{a}_1 \cdot (\mathbf{a}_2 \times \mathbf{a}_3)$  is the unit cell volume. This cell is therefore called *supercell* and the matrix  $M^{\text{sc}}$  is the *supercell matrix*.

We define the supercell such that its midpoint is located at the origin, i. e.,

$$\mathbb{V}_{\text{sc}} = \{ \mathbf{x} = x^\mu \mathbf{A}_\mu : x^\mu \in [-0.5, 0.5]_{\mathbb{R}} \}. \quad (2.31)$$

The vectors  $\mathbf{S} = S^\mu \mathbf{A}_\mu$  are the equivalent of the Bravais vectors  $\mathbf{L}$  in a superlattice described by  $\{\mathbf{A}_\mu\}$  instead of  $\{\mathbf{a}_\mu\}$ . The ideal, infinite crystal is

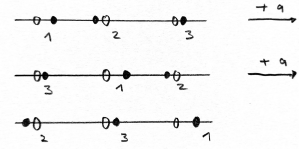


Figure 2.1:

**REM: w/o PBC!**

A linear chain with three atoms (bullets) displaced from their equilibrium position (open circles). With periodic boundary conditions, the consecutive translation by a lattice vector  $a$  induces a permutation of the atoms, i. e.,  $(1, 2, 3) \rightarrow (3, 1, 2) \rightarrow (2, 3, 1)$ .

<sup>6</sup> The notation  $N_{\mathbf{q}}$  will become more clear in the next section, where we deal with the inverse lattice points denoted by  $\mathbf{q}$ .

obtained in the limit  $N_{\mathbf{q}} \rightarrow \infty$ . By imposing the periodic boundary conditions specified in Eq.(2.29), the force constants become periodic functions in the superlattice,

$$\Phi_{i\mathbf{L}\alpha,j\mathbf{K}+\mathbf{S}\beta} = \Phi_{i\mathbf{L}\alpha,j\mathbf{K}\beta} \quad \text{for all } \mathbf{S} = S^\mu \mathbf{A}_\mu . \quad (2.32)$$

Again this property carries over to the dynamical matrix. In contrast to Eq.(2.28), the translational invariance expressed by Eq.(2.32) must be regarded as an *extrinsic* periodicity of the system, as it imposes an effective cutoff on the range of interactions captured in the finite supercell.

**REM:** Supercell imposes effective cutoff on the range of the force constants -> effect on spectrum, Maradudin, Ledermann

### 2.2.3 Dynamical matrix for periodic systems

Using the periodic boundary conditions in the superlattice, the dynamical matrix for the crystal can be written in terms of a Fourier series as

$$D_{i\mathbf{L}\alpha,j\mathbf{K}\beta} = \frac{1}{N_{\mathbf{q}}} \sum_{\mathbf{q}} e^{-i\mathbf{q} \cdot (\mathbf{R}_{i\mathbf{L}}^0 - \mathbf{R}_{j\mathbf{K}}^0)} D_{i\alpha,j\beta}(\mathbf{q}) , \quad (2.33)$$

with the inverse relation

$$D_{i\alpha,j\beta}(\mathbf{q}) = \frac{1}{N_{\mathbf{q}}} \sum_{\mathbf{L},\mathbf{K}} e^{i\mathbf{q} \cdot (\mathbf{R}_{i\mathbf{L}}^0 - \mathbf{R}_{j\mathbf{K}}^0)} D_{i\mathbf{L}\alpha,j\mathbf{K}\beta} \quad (2.34)$$

$$\equiv \sum_{\mathbf{L}} e^{-i\mathbf{q} \cdot \mathbf{L}} e^{i\mathbf{q} \cdot (\mathbf{R}_i^0 - \mathbf{R}_j^0)} D_{i0\alpha,j\mathbf{L}\beta} , \quad (2.35)$$

where in the last step the intrinsic periodicity of the crystal was used to write the dynamical matrix in Eq.(2.35) as a single sum over lattice points that are contained in the supercell only,  $\{\mathbf{L} \in \mathbb{V}_{sc}\}$ . The  $\mathbf{q}$ -points are elements of the inverse superlattice given by the lattice vectors of the reciprocal supercell,

$$\mathbf{B}^\mu = 2\pi \varepsilon^{\mu\nu\rho} \frac{\mathbf{A}_\nu \times \mathbf{A}_\rho}{\mathbf{A}_1 \cdot (\mathbf{A}_2 \times \mathbf{A}_3)} , \quad (2.36)$$

where  $\varepsilon^{\mu\nu\rho}$  denotes the Levi-Civita symbol enforcing the correct ordering of  $\mu\nu\rho$ , so that

$$\mathbf{q} = q_\mu \mathbf{B}^\mu \quad \text{with } q_\mu \in \mathbb{Z} . \quad (2.37)$$

These  $\mathbf{q}$ -points are called *commensurate*, as they represent wave numbers that fit into the supercell, and the  $q_\mu$  can be chosen such that each  $\mathbf{q}$  is located in the first Brillouin zone of the inverse lattice. In total, there are  $N_{\mathbf{q}}$  inequivalent values of  $\mathbf{q}$ .

Equation (2.35) transforms the  $3N_{sc} \times 3N_{sc}$  matrix  $D_{IJ}$  to one  $3N_{uc} \times 3N_{uc}$  matrix  $D_{ij}(\mathbf{q})$  for each  $\mathbf{q}$ , where  $N_{uc}$  is the number of atoms in the unit cell, and  $N_{sc} = N_{\mathbf{q}} N_{uc}$  the number of atoms in the supercell. The phase factor  $e^{i\mathbf{q} \cdot (\mathbf{R}_i^0 - \mathbf{R}_j^0)}$  does not change the eigenvalues of  $D(\mathbf{q})$  and is sometimes omitted to simplify the formulas [21].

### 2.2.4 Interpolation to non-commensurate $q$ -points

When restricting the lattice points to the supercell, the dynamical matrix as defined in Eq.(2.35) is evaluated only for the truncated sum over  $\{\mathbf{L} \in \mathbb{V}_{sc}\}$ .

The wavenumbers  $\mathbf{q}$  are then restricted to the commensurate  $\mathbf{q}$ -points, i. e., the points given in terms of Eq. (2.37). Evaluating the truncated dynamical matrix at a non-commensurate value  $\tilde{\mathbf{q}}$  will, in general, yield a non-hermitian matrix which cannot be used to extract physically sound information about the system. To obtain an *approximated* dynamical matrix at any other, non-commensurate value  $\tilde{\mathbf{q}}$  within the Brillouin zone, we define an *extended supercell*,

$$\mathbb{V}_{\text{sc}}^{\text{ext}} = \{ \mathbf{x} = x^\mu \mathbf{A}_\mu : x^\mu \in [-0.5, 0.5]_{\mathbb{R}} \} , \quad (2.38)$$

which also contains the lattice points at the positive boundary of the supercell as depicted by open circles in Fig. 2.2.

These lattice points are included in the Fourier series with an appropriate weight  $w_{\mathbf{L}}$  that accounts for double counting of lattice points that are separated by a linear combination of supercell lattice vectors  $\mathbf{S}$  [43]. Furthermore, we use a minimal image convention (MIC) between the atoms  $(i, \mathbf{0})$  and  $(j, \mathbf{L})$ : For each pair, we use an equivalent lattice point  $\mathbf{L}'$  within the extended supercell which depends on  $(i, j, \mathbf{L})$  such that

$$-\mathbf{R}_i^0 + \mathbf{R}_j^0 + \mathbf{L}' \in \mathbb{V}_{\text{sc}}^{\text{ext}} . \quad (2.39)$$

In total we define

$$D_{i\alpha,j\beta}(\tilde{\mathbf{q}}) = \sum_{\mathbf{L} \in \mathbb{V}_{\text{sc}}^{\text{ext}}} w_{\mathbf{L}} e^{-i\tilde{\mathbf{q}} \cdot \mathbf{L}'} e^{i\tilde{\mathbf{q}} \cdot (\mathbf{R}_i^0 - \mathbf{R}_j^0)} D_{i0\alpha,j\mathbf{L}\beta} \quad (2.40)$$

where  $\mathbf{L}'$  is chosen such that it satisfies Eq. (2.39), and the weights  $w_{\mathbf{L}}$  are chosen based on the multiplicity of the lattice point  $\mathbf{L}$  in the extended supercell. The dynamical matrices defined by Eq. (2.35) and (2.40) are equal when evaluated at commensurate  $\mathbf{q}$ -points. We will therefore use the latter definition as *the* dynamical matrix in the following.

## 2.2.5 Properties of the Dynamical Matrix and its Eigenvectors

As noted before, the dynamical matrix  $D(\mathbf{q})$  defined in Eq. (2.40) is a hermitian  $3N_{\text{uc}} \times 3N_{\text{uc}}$  matrix in the indices  $(i\alpha, j\beta)$  for each  $\mathbf{q}$  within the Brillouin zone.<sup>7</sup> The  $3N_{\text{uc}}$  eigenvalues will therefore be real, and there will be  $3N_{\text{uc}}$  complex, orthogonal eigenvectors. In accordance with Eq. (2.12) we denote

$$\sum_{j\beta} D_{i\alpha,j\beta}(\mathbf{q}) e_{b,j\beta}(\mathbf{q}) = \omega_b^2(\mathbf{q}) e_{b,i\alpha}(\mathbf{q}) , \quad (2.41a)$$

$$D_{i\alpha,j\beta}(\mathbf{q}) = \sum_b \omega_b^2(\mathbf{q}) e_{b,i\alpha}(\mathbf{q}) e_{b,j\beta}^*(\mathbf{q}) , \quad (2.41b)$$

where the *band index*  $b$  is used to discern the  $3N_{\text{uc}}$  branches at each  $\mathbf{q}$ .<sup>8</sup> Since  $D(\mathbf{q})$  is hermitian, it follows that [44]

$$D_{i\alpha,j\beta}(-\mathbf{q}) = D_{i\alpha,j\beta}^*(\mathbf{q}) , \quad (2.42)$$

$$e_{b,i\alpha}(-\mathbf{q}) = e_{b,i\alpha}^*(\mathbf{q}) , \text{ and} \quad (2.43)$$

$$\omega_b(-\mathbf{q}) = \omega_b(\mathbf{q}) . \quad (2.44)$$

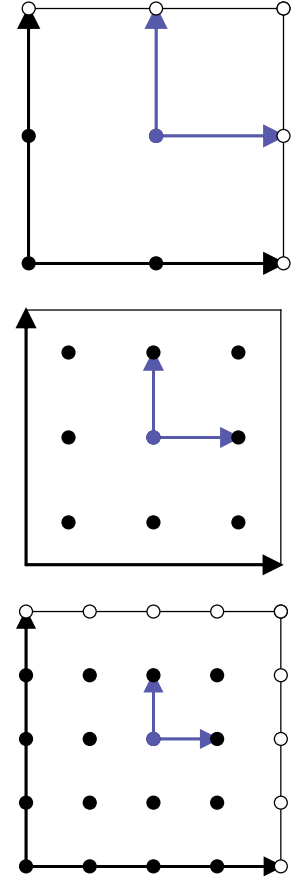


Figure 2.2: Depiction of square supercells with lattice points in the range  $[-0.5A, 0.5A]$  (bullets  $\bullet$ ), and extended lattice points at the supercell boundary (empty bullets  $\circ$ ), where  $A$  is the edge length of the supercell. Blue arrows denote the unit cell vectors, black arrows denote the supercell vectors.

<sup>7</sup> These can be either commensurate points  $\mathbf{q}$ , or interpolated points  $\tilde{\mathbf{q}}$ .

<sup>8</sup> The notation highlights that the  $\mathbf{q}$  become quasi-continuous in the  $N_{\mathbf{q}} \rightarrow \infty$  limit. In that case,  $\frac{1}{N_{\mathbf{q}}} \sum_{\mathbf{q}} \rightarrow \int \frac{d^3 q}{(2\pi)^3}$

With the help of Eq.(2.41), the real-space dynamical matrix  $D_{IJ}$  for the supercell can be written as

$$D_{i\mathbf{L}\alpha,j\mathbf{K}\beta} = \frac{1}{N_{\mathbf{q}}} \sum_{\mathbf{q}} e^{-i\mathbf{q}\cdot(\mathbf{R}_{i\mathbf{L}}^0 - \mathbf{R}_{j\mathbf{K}}^0)} D_{i\alpha,j\beta}(\mathbf{q}) \quad (2.45)$$

$$\equiv \sum_{b,\mathbf{q}} \omega_b^2(\mathbf{q}) e_{b,i\mathbf{L}\alpha}(\mathbf{q}) e_{b,j\mathbf{K}\beta}^*(\mathbf{q}) . \quad (2.46)$$

The eigenvectors of the  $3N_{\text{uc}} \times 3N_{\text{uc}}$  matrices  $\mathbf{D}(\mathbf{q})$  appearing in Eq.(2.41), and the eigenvectors of the  $3N_{\text{sc}} \times 3N_{\text{sc}}$  matrix  $D_{IJ}$  appearing in Eq.(2.46) are related by

$$e_{b,i\mathbf{L}\alpha}(\mathbf{q}) \equiv \frac{1}{\sqrt{N_{\mathbf{q}}}} e^{-i\mathbf{q}\cdot\mathbf{R}_{i\mathbf{L}}^0} e_{b,i\alpha}(\mathbf{q}) . \quad (2.47)$$

The completeness relations accordingly read

$$\sum_{i\mathbf{L}\alpha} e_{b,i\mathbf{L}\alpha}(\mathbf{q}) e_{b',i\mathbf{L}\alpha}^*(\mathbf{q}') = \delta_{bb'} \delta(\mathbf{q} - \mathbf{q}') \quad \text{and} \quad (2.48)$$

$$\sum_{b,\mathbf{q}} e_{b,i\mathbf{L}\alpha}(\mathbf{q}) e_{b,j\mathbf{K}\beta}^*(\mathbf{q}) = \delta_{il} \delta_{\mathbf{L}\mathbf{K}} \delta_{\alpha\beta} , \quad (2.49)$$

WE USE THE SHORTHAND NOTATION  $s = (b, \mathbf{q})$  AND  $-s = (b, -\mathbf{q})$  in the following to simplify the notation, and explicitly refer to the band index  $b$  and the wavenumber  $\mathbf{q}$  only when necessary. With these shorthands, the formulas closely resemble the non-periodic case as introduced in Sec. 2.1, with  $3N_{\text{sc}}$  degrees of freedom, only that the eigenvectors  $\mathbf{e}_{s=(b,\mathbf{q})}$  can be complex-valued instead of strictly real. In this notation, the dynamical matrix reads

$$D_{I\alpha,J\beta} = \sum_s \omega_s^2 e_{s,I\alpha} e_{s,J\beta}^* . \quad (2.50)$$

### 2.2.6 Phonon dispersions and density of states

**REM:** It makes more sense to discuss the ha. model earlier, i.e., most of what is discussed in “class. harm. dyn.” at the end?

With the dynamical matrix for arbitrary  $\mathbf{q}$ -points in the Brillouin zone at hand, we are in position to evaluate the spectrum of harmonic vibrational excitations in a crystal, i. e., *phonon dispersions* or *phonon band structure*, as well as the *density of states*, often called DOS for short.

The density of states  $g(\omega)$  can be used to evaluate Brillouin-zone integrals of functions that depend on the phonon energy  $\hbar\omega(\mathbf{q})$ . It is implicitly defined via

$$\langle f \rangle = \frac{1}{V_{\text{BZ}}} \int \frac{d^3q}{(2\pi)^3} f(\omega(\mathbf{q})) = \int d\omega f(\omega) g(\omega) , \quad (2.51)$$

where

$$g(\omega) = \frac{1}{V_{\text{BZ}}} \int \frac{d^3q}{(2\pi)^3} \delta(\omega(\mathbf{q}) - \omega) , \quad (2.52)$$

The density of states can be computed by evaluating the phonon frequencies  $\omega(\mathbf{q})$  on a grid in the Brillouin zone and use approximations to the  $\delta$ -function in Eq.(2.52) of finite width, for example by using Gaussian functions, or by using a tetrahedron method where the integration weights on the finite grid are computed analytically based on the dispersion [45].

IN EXPERIMENT, DISPERSIONS CAN BE PROBED by neutron scattering, where the incoming neutron beam scatters inelastically with the phonons in the crystal, and a momentum-dependent scattering amplitude can be measured with peaks corresponding to the phonon frequencies [46]. The phonon spectrum of fcc-silicon compared to inelastic neutron scattering data is shown in Fig. 2.3. An alternative approach is *Raman scattering*, where an incoming

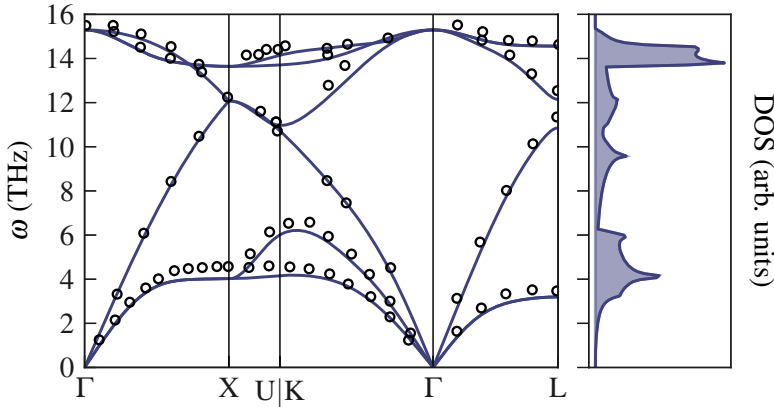


Figure 2.3: Phonon bandstructure of fcc-diamond silicon obtained for a supercell with 216 atoms. Open circles denote experimental reference data from inelastic neutron scattering at room temperature [47].

light beam scatters with a subset of the modes depending on their symmetry properties. Since the light has typical frequencies similar of the vibrational spectrum, i. e., of the order of 10 THz  $\sim$  40 meV, its wavenumber  $k = \omega/c$  is approximately  $3 \cdot 10^{-7} \text{ \AA}^{-1}$ , where  $c$  is the speed of light. Taking a typical crystal lattice constant of  $a \approx 5 \text{ \AA}$ , the maximum crystal wavenumber is  $q = 2\pi/a \approx 1 \text{ \AA}^{-1}$ . Light of similar energy as phonons therefore typically probe the dispersion very close to  $\mathbf{q} = 0$ , i. e., the  $\Gamma$  point. A comparison of calculated phonon dispersion and frequencies from Raman spectroscopy is shown in Fig. 2.4 for the orthorombic perovskite  $\text{KCaF}_3$  [48, 49, 50].

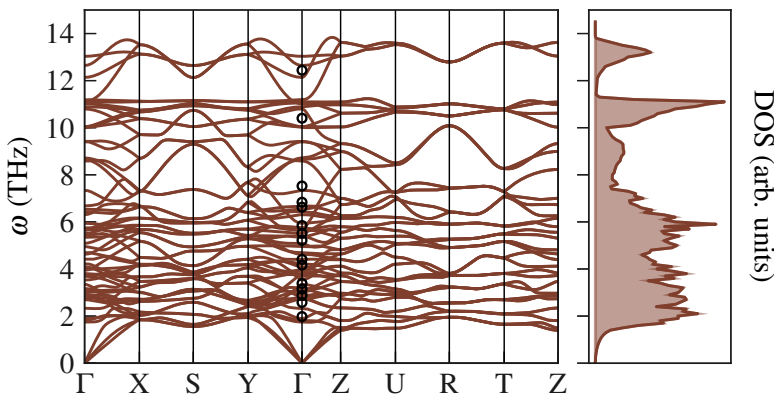


Figure 2.4: Phonon bandstructure of  $\text{KCaF}_3$  in the Pnma structure obtained from a supercell with 160 atoms. Open circles denote experimental reference data from Raman scattering at 40 K [51].

## 2.3 Statistical Mechanics and Molecular Dynamics

After discussing nuclear dynamics in the harmonic approximation, and specifying the crystalline state in terms of an intrinsic and extrinsic periodicity in space, we proceed by discussing nuclear dynamics on the full potential energy surface  $\mathcal{V}(\mathbf{R})$  without approximations, but in the classical limit.

### 2.3.1 Classical Limit

The classical limit of the nuclear Schrödinger equation (2.1) is usually performed by writing the nuclear wavefunction  $\chi(\mathbf{R}, t)$  in terms of a real amplitude  $A(\mathbf{R}, t)$  and a *classical action function*  $S(\mathbf{R}, t)$  [40, 52, 23]

$$\chi(\mathbf{R}, t) = A(\mathbf{R}, t) e^{\frac{i}{\hbar} S(\mathbf{R}, t)}. \quad (2.53)$$

The Schrödinger equation then yields a set of differential equations for  $A$  and  $S$  that, in the limit  $\hbar \rightarrow 0$ , go over to a *Hamilton-Jacobi* equation for the action  $S$ ,

$$\frac{\partial S}{\partial t} + \mathcal{H}(\mathbf{R}, \mathbf{P}) = 0, \quad (2.54)$$

where  $\mathbf{P} = (\mathbf{P}_1, \dots) \equiv (\nabla_1 S, \dots)$  denotes the conjugate momenta and  $\mathcal{H}$  is the *classical Hamilton function*<sup>9</sup> corresponding to the operator in Eq. (2.1), from which the equations of motion for the nuclei can be obtained:

$$\dot{\mathbf{P}}_I = -\frac{\partial \mathcal{H}}{\partial \mathbf{R}_I} \implies M_I \ddot{\mathbf{R}}_I = -\frac{\partial \mathcal{V}}{\partial \mathbf{R}_I}. \quad (2.55)$$

The negative gradient of the Born-Oppenheimer potential,  $-\partial \mathcal{V} / \partial \mathbf{R}_I$  is the force  $\mathbf{F}_I$  acting on atom  $I$  which can be obtained via the Hellmann-Feynmann theorem, cf. Sec. 1.4.1.

AN ALTERNATIVE VIEWPOINT that is more instructive can be taken by invoking the *Ehrenfest theorem* [53, 54]. The statement is that the time derivative of the expectation value of an atom's momentum  $\mathbf{P}_I$  is given by the expectation value of the negative gradient of the potential,

$$\frac{d}{dt} \langle \mathbf{P}_I \rangle_\chi = \left\langle -\frac{\partial \mathcal{V}}{\partial \mathbf{R}_I} \right\rangle_\chi, \quad (2.56)$$

where  $\langle \cdot \rangle_\chi$  denotes an expectation value taken with respect to the nuclear wavefunction  $\chi$ . This expression differs only slightly from the classical counterpart, which would read

$$\frac{d}{dt} \langle \mathbf{P}_I \rangle = -\frac{\partial \mathcal{V}}{\partial \mathbf{R}_I} \Big|_{\mathbf{R}=\langle \mathbf{R} \rangle}. \quad (2.57)$$

The difference comes from the fact that, in quantum mechanics, the expectation value of a function of an observable does not equal the function of its expectation. In mathematical terms, we have

$$\delta f \equiv f(\langle x \rangle) - \langle f(x) \rangle \neq 0, \quad (2.58)$$

where  $x = \mathbf{R}_I$  denotes the space coordinate,  $f$  is some function of the observable  $x$ , and  $\delta f$  measures the difference between the two values, i. e., the

<sup>9</sup> We use the terms *Hamilton function* and *Hamiltonian* interchangeably in the following.

error introduced by using a classical description. Ehrenfest's argument is that this difference becomes negligible when the state is sufficiently peaked around some value  $x_0$ . Expanding  $f$  around the expectation value of  $x$  denoted by  $x_0 \equiv \langle x \rangle$ , we have

$$f(x) = f(\langle x \rangle) + (x - \langle x \rangle) f'(\langle x \rangle) + \frac{1}{2} (x - \langle x \rangle)^2 f''(\langle x \rangle) + \dots \quad (2.59)$$

It follows that the  $f'$  term vanishes when the expectation value is taken, and

$$\langle f(x) \rangle = f(\langle x \rangle) + \frac{1}{2} \Delta x^2 f''(\langle x \rangle) + \dots, \quad (2.60)$$

where  $\Delta x^2 = \langle (x - \langle x \rangle)^2 \rangle$  measures the variance of the underlying distribution, i. e. the width of the wavepacket. The relative error between the classical and quantum expectation value is therefore proportional to the variance  $\Delta x^2$ ,

$$\left| \frac{\delta f}{f(\langle x \rangle)} \right| = \frac{1}{2} \Delta x^2 \left| \frac{f''(\langle x \rangle)}{f(\langle x \rangle)} \right| + O(\Delta x^3). \quad (2.61)$$

This estimation is general and holds for any observable  $f$ . By crudely estimating the dimension of the wavepacket in terms of the thermal de Broglie-wavelength, we find

$$\Delta x^2 \sim \left( \frac{h}{P} \right)^2 \sim \frac{h^2}{MT}, \quad (2.62)$$

where  $h$  is Planck's constants,  $M$  is the atomic mass, and  $T$  is temperature. This estimate gives support to the intuitive assumption that we can expect the classical limit to work better the heavier the atoms and the higher the temperature. Let us now set  $f(x) \hat{=} -\partial \mathcal{V}/\partial \mathbf{R}_I$ , then another important conclusion can be drawn from Eq. (2.61): For a harmonic potential  $\mathcal{V}(\mathbf{R}) = \mathcal{V}^{(2)}(\mathbf{R})$ , where derivatives higher than second order vanish, the classical and quantum mechanical expectation values coincide. The quantum mechanical expectation value of the position will therefore evolve in the same time-periodic fashion as a classical particle in a harmonic well.

THESE CONSIDERATIONS NATURALLY LEAD TO THE FORMULATION OF AB INITIO MOLECULAR DYNAMICS SIMULATIONS, where the time evolution of a system of particles is simulated by propagating the classical equations of motion for each particle on the Born-Oppenheimer potential energy surface,  $\mathcal{V}(\mathbf{R})$  [55, 56]. In conjunction with classical statistical mechanics, a wealth of thermodynamic properties of materials can be simulated. We note in passing that additional care must be taken at low temperatures and for systems with light atoms, especially hydrogen-bonded systems, because in these cases the quantum nature of the nuclei can become non-negligible, as already mentioned in the discussion following Eq. (2.62) [57, 58, 59].

AS THERE EXIST PLENTY OF EXCELLENT BOOKS ON STATISTICAL MECHANICS, some of which are included in the references [60, 61, 62], this chapter mainly serves to recall the most important notions necessary for computing properties of materials under thermodynamic conditions, and introduce the notation used in the remainder of the work. In particular, the concepts of ensemble, state, and averages are briefly introduced. 

*This is O.K. as it is needed for your later analysis. The other stuff is like "trying but not succeeding to write a text book."*

### 2.3.2 Phase space and ergodic hypothesis

A thermodynamic *ensemble* can be viewed as a complete list of all allowed *states*  $\Gamma$  of a system of particles, where the state is an instantaneous snapshot of all microscopic variables [60]. In classical statistical mechanics, these variables are the  $N$  positions  $\mathbf{R} = (\mathbf{R}_1, \dots, \mathbf{R}_N)$  and momenta  $\mathbf{P} = (\mathbf{P}_1, \dots, \mathbf{P}_N)$ .<sup>10</sup> A particular configuration  $\Gamma = \{\mathbf{R}, \mathbf{P}\}$  is called *phase-space point*, and the phase space is the collection of all points  $\Gamma$  compliant with external constraints.<sup>11</sup> To each state  $\Gamma$ , a statistical weight  $f(\Gamma)$  is assigned, where  $f$  is called the *distribution function*. A thermodynamic ensemble is completely specified by the set of external constraints under which the mechanical system evolves, and the associated statistical weight function  $f$ .

STATISTICAL AVERAGES OF PHASE-SPACE FUNCTIONS can be obtained by averaging over all permissible states  $\Gamma$  with the statistical weight given by the distribution function,  $f(\Gamma)$ . The *phase-space average* of a generic phase-space function  $A(\Gamma)$  is defined as

$$\langle A \rangle_f = \int d\Gamma A(\Gamma) f(\Gamma). \quad (2.63)$$

An alternative approach towards computing averages is the concept of time averaging. The *time average* of a phase-space function is defined as

$$\langle A \rangle_t = \lim_{t \rightarrow \infty} \frac{1}{t} \int_0^t dt' A(\Gamma_{t'}), \quad (2.64)$$

where  $\Gamma_t = \{\mathbf{R}(t), \mathbf{P}(t)\}$  denotes a phase-space point at time  $t$  after evolving from an initial point  $\Gamma_0$  as explained in the next section. A system for which the phase-space and the time average are identical is said to be *ergodic*. The *ergodic hypothesis* states that this is true for most systems with non-pathological particle interaction  $\mathcal{V}$ . Albeit being virtually impossible to prove rigorously, this hypothesis is the underlying idea of *molecular dynamics* (MD) simulations, where the statistical behavior of a system is assessed by choosing a suitable initial condition and propagating it in time by numerically solving the equations of motion.

IN THIS WORK, we use two thermodynamic ensembles: the microcanonical, *NVE* for short, where the total energy  $E$  of the system is conserved, and the canonical (*NVT*), where the system can be viewed as coupled to a bath of temperature  $T$ . The latter is mimicking more realistic experimental conditions, where usually the temperature and not the total energy of the system can be controlled. Technically, experiments are performed rather at constant pressure  $p$  instead of constant volume, and the correct ensemble to describe such a situation is the isothermal-isobaric one commonly denoted as *NPT*. In practice however, the canonical ensemble is easier to simulate and is a good approximation to the *NPT* ensemble when the system size is not too small [61, p. 134]

### 2.3.3 Microcanonical Ensemble

The microcanonical ensemble is characterized by three conserved extensive quantities: particle number  $N$ , system volume  $V$ , and total energy  $E$ . The

<sup>10</sup> We denote by  $N$  either the number of atoms in a system of finite size, or, in periodic systems, the number of atoms in the simulation cell,  $N_{sc}$ .

<sup>11</sup> The simplest example of an external constraint: If the particles are confined in a box with impenetrable walls, the possible position  $\mathbf{R}$  are necessarily confined to that box. Other constraints comprise total energy, particle number, and more.

total energy of a given microstate, i. e., the configuration of particles and their momenta represented by the phase-space point  $\Gamma = \{ \mathbf{R}, \mathbf{P} \}$ , is given by the Hamiltonian of the system,  $\mathcal{H}(\Gamma)$ . The microcanonical distribution function is defined as

$$f_E(\Gamma) = \frac{1}{\mathcal{Z}_E} \delta(\mathcal{H}(\Gamma) - E), \quad (2.65)$$

where the microcanonical partition function  $\mathcal{Z}_E$  is a normalizing factor for  $f_E$ . The distribution function  $f_E$  encapsulates the underlying postulate of the microcanonical ensemble, i. e., that any point in phase space  $\Gamma$  yielding an energy  $\mathcal{H}(\Gamma)$  in a thin interval around the target energy  $E$  will be realized with the same likelihood.

THE TIME EVOLUTION OF A SYSTEM is governed by the Hamiltonian  $\mathcal{H}$  which generates an energy conserving propagation of a phase space point  $\Gamma_t = \{ \mathbf{R}(t), \mathbf{P}(t) \}$  in terms of Hamilton's equations,

$$\dot{\mathbf{R}}_I(t) = \frac{\partial \mathcal{H}(t)}{\partial \mathbf{P}_I} \quad \text{and} \quad \dot{\mathbf{P}}_I(t) = -\frac{\partial \mathcal{H}(t)}{\partial \mathbf{R}_I}. \quad (2.66)$$

The temporal evolution of a phase-space observable  $B(\Gamma_t) \equiv B(t)$  is then given by the Liouville equation [61]

$$\dot{B}(t) = \{ B(t), \mathcal{H}(t) \} \equiv i\mathcal{L}B(t), \quad (2.67)$$

where  $\mathcal{L}$  is the *Liouville operator* defined by its action according to Eq. (2.67), and  $\{ \cdot, \cdot \}$  denotes the *Poisson bracket*. The Liouville equation is formally solved by

$$B(t) = e^{i\mathcal{L}t} B(0), \quad (2.69)$$

the operator  $e^{i\mathcal{L}t}$  is therefore called the *time evolution operator* or *classical propagator*. In practice, the equations of motion are solved numerically, for example by the *velocity Verlet* algorithm [63],

$$\mathbf{R}_I(t + \delta t) = \mathbf{R}_I(t) + \delta t \dot{\mathbf{R}}_I(t) + \frac{\delta t^2}{2M_I} \mathbf{F}_I(t) + O(\delta t^4), \quad (2.70a)$$

$$\dot{\mathbf{R}}_I(t + \delta t) = \dot{\mathbf{R}}_I(t) + \frac{\delta t}{2M_I} [\mathbf{F}_I(t) + \mathbf{F}_I(t + \delta t)] + O(\delta t^4). \quad (2.70b)$$

The velocity Verlet algorithm introduces an error of order  $\delta t^4$  in the integration step, but has two important properties mitigating a negative impact on observables: First, a velocity Verlet integration step is time-reversible, an important prerequisite for long-term stability of the total energy for symmetry reasons. Second, the velocity Verlet map from  $t$  to  $t + \delta t$  has the property of being *symplectic* [61, p. 101]. This means that the discrete time propagation is not guaranteed to preserve the energy along the trajectory  $\Gamma_t$ , but there exists a Hamiltonian  $\tilde{\mathcal{H}}(\Gamma, \delta t)$  which is conserved exactly and fulfills  $\mathcal{H}(\tilde{\Gamma}, \delta t) \rightarrow \mathcal{H}(\Gamma)$  for vanishing timestep  $\delta t \rightarrow 0$  [61, p. 121]. The symplectic property is formalized in the “shadowing theorem”, which states that existence of a “shadow Hamiltonian”  $\tilde{\mathcal{H}}$  ensures that errors introduced by using a finite time step are bounded [61, p. ,120].

The Poisson bracket is defined by

$$\{ B, \mathcal{H} \} = \sum_{I,\alpha} \frac{\partial B}{\partial R_I^\alpha} \frac{\partial \mathcal{H}}{\partial P_I^\alpha} - \frac{\partial B}{\partial P_I^\alpha} \frac{\partial \mathcal{H}}{\partial R_I^\alpha} \quad (2.68)$$

### 2.3.4 Canonical ensemble

The canonical ensemble is characterized by the two extensive variables particle number  $N$  and volume  $V$ , and the intensive quantity temperature  $T$ . It can be viewed as representing a system in contact with an infinite thermal bath of temperature  $T$ , where heat can be exchanged via a weak coupling. In analogy to the previous section, we define the *canonical distribution function* at inverse temperature  $\beta = 1/k_B T$

$$f_\beta(\Gamma) = \frac{1}{Z_\beta} e^{-\beta \mathcal{H}(\Gamma)}, \quad (2.71)$$

where the canonical partition sum  $Z_\beta$  normalizes  $f_\beta$ .

As we have seen earlier, a time-independent Hamiltonian generates energy-preserving dynamics via the equations of motion given in Eq. (2.66). To perform a simulation at non-constant energy, the coupling to a thermal bath therefore has to be incorporated explicitly into the equations of motion. One of the many ways to achieve this is via the *Langevin equation* [64] in which the change of momentum is modified,

$$\dot{\mathbf{P}}_I(t) = \mathbf{F}_I(t) - \gamma \mathbf{P}_I(t) + \mathbf{F}_I^{\text{stochastic}}(t). \quad (2.72)$$

This equation describes a perturbation of the nuclei induced by a velocity-dependent friction proportional to a constant  $\gamma$ , and a stochastic force proportional to a white-noise kernel  $\eta(t)$ .<sup>12</sup> With the modified equations of motion in terms of the stochastic force, an ergodic time evolution that generates the canonical distribution can be obtained, so that

$$\langle A \rangle_t = \langle A \rangle_T. \quad (2.73)$$

In practice, the Langevin equation can be used to thermalize a system and generate a canonical ensemble starting from some initial configuration  $\mathbf{R}^0$  [61, p. 590].

Other ways of generating an *NVT* ensemble are deterministic Nosé-Hoover simulations, or the stochastic velocity rescaling approach that can preserve spectral properties [65, 66, 67].

*nuclear*  
It is important  
that you make  
it clear when  
a concept is  
from you. But  
it must also be  
clear when it is  
~100 years old  
and/or from others.

<sup>12</sup> The stochastic force is given by:

$$\begin{aligned} \mathbf{F}_I^{\text{stochastic}}(t) &= \sqrt{2k_B T M_I \gamma} \eta(t), \\ \langle \eta(t) \eta(0) \rangle &= \delta(t). \end{aligned}$$

It replenishes the kinetic energy dissipated by the friction proportional to  $\gamma$ , see discussion in Ref. [60, p. 328].

## 2.4 Classical harmonic dynamics and harmonic mapping

Also the harmonic Hamiltonian defined in Eq. (2.14) generates classical dynamics by means of the canonical equations of motion for the normal coordinates  $\{u_s, p_s\}$ ,<sup>13</sup>

$$\dot{u}_s = \frac{\partial \mathcal{H}^{(2)}}{\partial p_s} = p_s, \quad \text{and} \quad \dot{p}_s = -\frac{\partial \mathcal{H}^{(2)}}{\partial u_s} = -\omega_s^2 u_s. \quad (2.74)$$

These equations of motion can be solved in straightforward fashion in terms of plane waves for the normal mode coordinates  $\{u_s, p_s\}$ . We find it, however, more instructive to find a solution in formal similarity with quantum mechanics,<sup>14</sup> by first expressing the real normal coordinates  $\{u_s, p_s\}$  terms of complex, unitless amplitudes  $\{a_s\}$  as

$$u_s(t) \equiv \sqrt{\frac{\hbar}{2\omega_s}} [a_s^\dagger(t) + a_s(t)], \quad (2.75a)$$

$$p_s(t) \equiv i\sqrt{\frac{\hbar\omega_s}{2}} [a_s^\dagger(t) - a_s(t)], \quad (2.75b)$$

with the inverse relation

$$a_s = \sqrt{\frac{\omega_s}{2\hbar}} u_s + \frac{i}{\sqrt{2\hbar\omega_s}} p_s, \quad (2.76)$$

where  $a_s^\dagger$  denotes the complex conjugate of  $a_s$ . In terms of these amplitudes, the harmonic Hamiltonian reads

$$\mathcal{H}^{(2)}(\mathbf{a}, t) = \sum_s \hbar\omega_s a_s^\dagger(t) a_s(t) \equiv \sum_s \hbar\omega_s n_s(t), \quad (2.77)$$

where we identify the squared modulus of the amplitudes with the *mode occupation*  $n_s$ ,

$$a_s^\dagger(t) a_s(t) \equiv n_s(t). \quad (2.78)$$

The time derivative of the amplitude  $a_s$  is found by using the classical equations of motions given in Eq. (2.74),

$$\dot{a}_s = -i\omega_s a_s, \quad (2.79)$$

so that  $a_s(t)$  is given in terms of a complex plane wave,

$$a_s(t) = e^{-i\omega_s t} a_s(0). \quad (2.80)$$

It is evident that in the purely harmonic dynamics, the mode occupation defined in Eq. (2.78) is constant in time,  $n_s(t) \equiv n_s = \text{const}$ . We therefore express the amplitudes at intial time  $t = 0$  as

$$a_s(0) = \sqrt{n_s} e^{-i\varphi_s}, \quad (2.81)$$

where  $n_s$  and  $\varphi_s$  are chosen based on the initial configuration of atoms.

By using this solution for the normal coordinates  $\{u_s, p_s\}$  in Eq. (2.75), we find

$$u_s(t) = A_s \sin(\omega_s t + \varphi_s), \quad (2.82a)$$

$$p_s(t) = \omega_s A_s \cos(\omega_s t + \varphi_s), \quad (2.82b)$$

<sup>13</sup>We deal with the finite simulation cell, where the dynamical matrix is a symmetric matrix with real eigenvalues  $\omega_s^2$  and real eigenvectors  $e_{sI}$ .

How do you know this before doing the calculation?

<sup>14</sup>The relation to quantum mechanics is achieved by replacing the complex numbers  $a_s$  with the operators  $\hat{a}_s$  fulfilling the canonical commutation relations

$$[\hat{a}_s, \hat{a}_{s'}^\dagger] = \delta_{ss'}. \quad$$

where

$$A_s = \sqrt{\frac{2\hbar n_s}{\omega_s}} \quad (2.83)$$

is the amplitude of the mode displacement  $u_s$ .

FOR A SYSTEM IN THERMAL EQUILIBRIUM AT A FINITE TEMPERATURE  $T$ , the mode occupation  $n_s$  can be estimated by analogy with quantum mechanics, where the harmonic energy is given by [68]

$$\langle \mathcal{H}^{(2)} \rangle_T = \sum_s \hbar \omega_s \left( n_B(\omega_s, T) + \frac{1}{2} \right), \quad (2.84)$$

with the Bose function  $n_B(\omega, T)$  giving the occupation of state of energy  $\hbar\omega$  at temperature  $T$ .<sup>15</sup> The expectation of the mode amplitude is therefore given by

$$\langle n_s \rangle_T = \left( n_B(\omega_s, T) + \frac{1}{2} \right) \xrightarrow{k_B T \gg \hbar \omega_s} \frac{k_B T}{\hbar \omega_s}, \quad (2.85)$$

i.e., in the high temperature limit, the energy of the mode  $s$  given by  $E_s = \hbar \omega_s \langle n_s \rangle_T$  approaches the *equipartition* value

$$E_s = k_B T. \quad (2.86)$$

<sup>15</sup> Bose function ( $\beta = 1/k_B T$ ):

$$n_B(\omega, T) = \frac{1}{e^{\beta \hbar \omega} - 1}.$$

#### 2.4.1 Harmonic sampling

The solution to the equations of motion for the normal coordinates given in Eq. (2.82) can be used to describe the time evolution of the real-space displacements  $\mathbf{U}_I(t)$ ,

$$\mathbf{U}_I(t) = \frac{1}{\sqrt{M_I}} \mathbf{u}_I(t) = \frac{1}{\sqrt{M_I}} \sum_s \mathbf{e}_{sI} u_s(t) \quad (2.87)$$

$$= \frac{1}{\sqrt{M_I}} \sum_s A_s \mathbf{e}_{sI} \sin(\omega_s t + \varphi_s), \quad (2.88)$$

where  $\mathbf{e}_{sI}$  denotes the eigenvector elements corresponding to mode  $s$  and atom  $I$ . This equation can be used to generate atomic configurations representative for a given temperature via

$$\mathbf{U}_I = \frac{1}{\sqrt{M_I}} \sum_s \zeta_s \langle A_s \rangle_T \mathbf{e}_{sI}, \quad (2.89)$$

where  $\langle A_s \rangle_T = \sqrt{\frac{2\hbar \langle n_s \rangle_T}{\omega_s}}$  is the mean mode amplitude in terms of the mean mode occupation  $\langle n_s \rangle_T$  given by Eq. (2.85), and  $\zeta_s$  is a normally distributed random number mimicking thermal fluctuations [69]. The practical use of Eq. (2.89) is twofold: First, it can be used to pre-thermalize molecular dynamics simulations by providing an approximately correct distribution of displacements. Second, it can be used to estimate thermodynamic expectation values of configuration-dependent observables by approximating the ensemble average with respect to the full potential  $\mathcal{V}(\mathbf{R})$ ,

$$\langle B(\mathbf{R}) \rangle_T = \frac{1}{Z_V} \int d\mathbf{R} e^{-\beta \mathcal{V}(\mathbf{R})} B(\mathbf{R}), \quad (2.90)$$

with an average with respect to the harmonic potential,

$$\langle B(\mathbf{R}) \rangle_T^{(2)} \approx \frac{1}{M} \sum_{m=1}^M B(\mathbf{R}_m) , \quad (2.91)$$

where  $\mathbf{R}_m$  denotes a sample generated by Eq. (2.89), and  $M$  ist the total number of samples [70, p. 15]. This sampling approach can be understood as a harmonic Monte Carlo approach [69, 71].

*← everything was flat book. This statement is not. Explain why it is relevant for your thesis.*

#### 2.4.2 Harmonic mapping

In the previous section, we have investigated the time evolution of (mode) displacements generated by the harmonic model in analytical fashion. We found that the mode occupations  $n_s$ , and therefore the energy of each mode,  $E_s$ , were constant in time. Pictorially, this can be explained by the absence of interactions between the normal modes – once a mode is excited, it cannot lose or gain energy. The interaction of vibrational modes can be computed by means of perturbation theory, i. e., by computing the transition amplitudes between modes when taking higher than second-order force constants into account, or by using molecular dynamics simulations, where the interactions are naturally described non-perturbatively. All effects not described by the harmonic model are therefore called *anharmonic*, and we will investigate this topic in more detail in chapter 4. Since the normal mode displacements and momenta  $\{ u_s, p_s \}$  are obtained by means of a unitary transformation from the atom positions and momenta,  $\{ \mathbf{R}_I, \mathbf{P}_I \}$ , they provide a complete basis in which the nuclear dynamics can be described, even when anharmonic effects are considered. When anharmonic effects are not too strong, the main effect of interactions are a shift in frequencies, and finite lifetimes.

IN ORDER TO MAP THE DYNAMICAL EVOLUTION OF THE SYSTEM ONTO THE NORMAL MODES, we recall that normal mode coordinates an real-space coordinates are related by the eigenvectors  $\mathbf{e}_{s,I}$  of the dynamical matrix, i. e.,

$$u_s(t) = \sum_I \mathbf{e}_{s,I} \cdot \mathbf{u}_I(t) , \quad \text{and} \quad (2.92a)$$

$$p_s(t) = \sum_I \mathbf{e}_{s,I} \cdot \mathbf{p}_I(t) , \quad (2.92b)$$

from which the time-dependent complex amplitude  $a_s(t)$  can be found by means of Eq. (2.76), i. e.,

$$a_s(t) = \sqrt{\frac{\omega_s}{2\hbar}} u_s(t) + \frac{i}{\sqrt{2\hbar\omega_s}} p_s(t) , \quad (2.93)$$

with  $\{ u_s(t), p_s(t) \}$  given in terms of the real-space dynamics by Eq. (2.92). In terms of this complex amplitude, the mode occupation  $n_s$  becomes time-dependent,

$$n_s(t) = a_s^\dagger(t) a_s(t) , \quad (2.94)$$

as well as the mode energy,

$$E_s(t) = \hbar\omega_s n_s(t) . \quad (2.95)$$

We will later see how the time-dependent, mode-resolved energy can be used to extract phonon lifetimes from molecular dynamics simulations.

**REM:** Move this discussion to here?

As a final remark, we like to point out that for periodic systems, where  $s = (b, \mathbf{q})$ , the eigenvectors used in the transformation defined in Eq. (2.92) are not strictly real, and therefore the normal mode coordinates  $\{u_s, p_s\}$  can be complex numbers already. In this situation, one needs to define two independent complex amplitudes,  $a_s$  and  $a_{-s}$ , where  $s = (b, -\mathbf{q})$  denotes a mode with opposite wave vector [21, p. 300]. In this case, we define<sup>16</sup>

**REM:** Use notation  $-s \rightarrow \bar{s}$ ?

<sup>16</sup>The explicit formulas in terms of  $(b, \mathbf{q})$  are given in appendix G.1.

$$u_s(t) = \sum_I \mathbf{e}_{s,I} \cdot \mathbf{u}_I(t), \quad (2.96a)$$

$$p_s(t) = \sum_I \mathbf{e}_{s,I} \cdot \mathbf{p}_I(t). \quad (2.96b)$$

with

$$u_s(t) \equiv \frac{1}{\sqrt{2\omega_s}} [a_{-s}^\dagger(t) + a_s(t)], \quad (2.97a)$$

$$p_s(t) \equiv i\sqrt{\frac{\omega_s}{2}} [a_{-s}^\dagger(t) - a_s(t)], \quad (2.97b)$$

and the corresponding inverse relations

$$a_s = \sqrt{\frac{\omega_s}{2}} u_s + \frac{i}{\sqrt{2\omega_s}} p_s \quad (2.98a)$$

$$a_{-s}^\dagger = \sqrt{\frac{\omega_s}{2}} u_s - \frac{i}{\sqrt{2\omega_s}} p_s, \quad (2.98b)$$

in units where  $\hbar = 1$ . Using these amplitudes, the harmonic Hamiltonian reads

$$\mathcal{H}^{(2)} = \frac{1}{2} \sum_s \omega_s (a_s^\dagger a_s + a_{-s}^\dagger a_{-s}) \quad (2.99)$$

$$= \sum_s \omega_s a_s^\dagger a_s \quad (2.100)$$

where the last line holds when the summation contains both  $\mathbf{q}$  and  $-\mathbf{q}$ , because  $\omega_s = \omega_{-s}$ .

I think the text up to here should be reduced to 25-50% and 2 good text books should be cited.



# 3

## Heat Transport

*"It seems there is no problem in modern physics for which there are on record as many false starts, and as many theories which overlook some essential feature, as in the problem of the thermal conductivity of [electrically] non-conducting crystals."*

R. Peierls, 1960 [12]

Conductive heat transport is the phenomenon of vibrational energy traversing a material when a temperature gradient is applied. As first described by Joseph Fourier in the early 19th century [72], the heat flux  $\mathbf{J}$  resulting from a stationary temperature gradient  $\nabla T$  is directly proportional to this gradient. The proportionality constant is second-rank tensor denoted by  $\kappa$  and called the *thermal conductivity*. The defining equation,

$$\mathbf{J} = -\kappa \nabla T , \quad (3.1)$$

is called *Fourier's law*. The sign convention is such that the heat flows from "hot to cold" in compliance with the second law of thermodynamics. The regime where Eq. (3.1) is valid is called the *diffusive* regime, as it holds when the temperature gradient is small on microscopic scale, and the sample size is big enough so that boundary effects are negligible [73, 74].

It is evident from Eq. (3.1) that the thermal conductivity  $\kappa$  is an explicitly non-equilibrium quantity. As such, it can be related to equilibrium fluctuations by means of a *fluctuation-dissipation theorem* [75, 76, 77, 78], resulting in the famous Green-Kubo formula [79, 80],

$$\kappa^{\alpha\beta} = \frac{V}{k_B T^2} \int_0^\infty dt \langle J^\alpha(t) J^\beta(0) \rangle_{eq} . \quad (3.2)$$

This formula relates the temporal fluctuations of the macroscopic heat flux  $\mathbf{J}(t)$  as given by an equilibrium ensemble average of the autocorrelation function,  $\langle J^\alpha(t) J^\beta(0) \rangle_{eq}$ , to the associated transport coefficient  $\kappa^{\alpha\beta}$ , where  $\alpha$  and  $\beta$  denote the respective Cartesian components. It is however *a priori* unclear how a microscopic description of the appearing quantities can be obtained. To tackle this question in full, we first show how the Kubo formula emerges in the framework of linear response theory. We then present how a microscopic description of heat in terms of a thermal energy density and an associated, locally conserved current follows, before reviewing the necessary steps to define an *ab initio* heat flux [15].

Why is this 60 years old statement relevant today?

I would be better to define all means of heat transport first.

Is this your proof? or are you repeating other people's work?

### 3.1 Linear Response Theory

The aim of linear response theory is to compute the expected value of a phase-space observable  $B$  in presence of an external perturbation driving the system out of equilibrium. The ensemble is characterized by a *distribution function*  $f(\Gamma, t)$ , where  $\Gamma = \{\mathbf{R}, \mathbf{P}\}$  is a shorthand for a point in phase space. The expectation value of  $B$  as defined in Eq. (2.63) is given by

$$\langle B(t) \rangle = \int d\Gamma B(\Gamma) f(\Gamma, t), \quad (3.3)$$

and we assume without loss of generality that its equilibrium value vanishes,

$$\langle B(t) \rangle_0 = \int d\Gamma B(\Gamma) f^0(\Gamma) = 0, \quad (3.4)$$

where  $f^0(\Gamma)$  is the distribution function of the unperturbed system in thermal equilibrium. In order to calculate Eq. (3.3) in a non-equilibrium situation, we start by defining the Hamiltonian describing the dynamics of the system in the absence of external perturbations,  $\mathcal{H}^0$ , which we take to be given by the many-body Hamiltonian

$$\mathcal{H}^0(\Gamma) = \sum_I \frac{\mathbf{P}_I^2}{2M_I} + \mathcal{V}(\mathbf{R}). \quad (3.5)$$

The canonical distribution function for the unperturbed system reads

$$f^0(\Gamma) = \frac{1}{Z^0} e^{-\beta \mathcal{H}^0(\Gamma)}, \quad (3.6)$$

where the partition function  $Z_0$  normalizes the phase-space integral,  $\int d\Gamma f^0(\Gamma) = 1$ .

In the next step, we write the full Hamiltonian as

$$\mathcal{H}(\Gamma, t) = \mathcal{H}^0(\Gamma) + \lambda \mathcal{H}'(\Gamma, t), \quad (3.7)$$

where the perturbation is given by some yet unspecified phase-space function  $\mathcal{H}'(\Gamma, t)$  with explicit time dependence, and  $\lambda = 1$  is a bookkeeping parameter that we introduce to count the order in the perturbation. We write the distribution function in presence of the perturbation as

$$f(\Gamma, t) = f^0(\Gamma) + \lambda \Delta f(\Gamma, t), \quad (3.8)$$

where  $\Delta f$  is the perturbation in the distribution generated by  $\mathcal{H}'$ . Using that  $f^0$  carries no explicit time dependence, the Liouville equation for  $\Delta f$  reads

$$\begin{aligned} \lambda \frac{d\Delta f}{dt} &= \{ \mathcal{H}, f \} \\ &= \lambda \{ \mathcal{H}^0, \Delta f \} + \lambda \{ \mathcal{H}', f^0 \} + \mathcal{O}(\lambda^2), \end{aligned} \quad (3.9)$$

$$\Rightarrow \frac{d\Delta f}{dt} \approx \{ \mathcal{H}^0, \Delta f \} + \{ \mathcal{H}'(t), f^0 \} \quad (3.10)$$

where  $\{ \cdot, \cdot \}$  denotes the Poisson bracket and in Eq. (3.10) we only keep the terms to linear order in the perturbation. The solution to this differential equation is found to be<sup>1</sup> [78]

$$\Delta f(\Gamma, t) = \int_{-\infty}^t e^{-i\mathcal{L}^0(t-t')} \{ \mathcal{H}'(\Gamma, t'), f^0(\Gamma) \} dt', \quad (3.11)$$

<sup>1</sup> The solution is given in appendix F.

where  $e^{i\mathcal{L}^0 t}$  propagates a phase-space point  $\Gamma$  by a time  $t$  according to the equations of motion following from  $\mathcal{H}^0$ . By splitting the interaction Hamiltonian  $\mathcal{H}'(t)$  into an operator part  $A(\Gamma)$  and an explicitly time dependent force function  $F(t)$ ,

$$\mathcal{H}'(\Gamma, t) = A(\Gamma)F(t), \quad (3.12)$$

equation (3.10) can be simplified in the canonical ensemble by using that  $\partial f^0 / \partial \mathcal{H}^0 = -\beta f^0$ , which leads to<sup>2</sup>

$$\{A, f^0\} = -\beta \dot{A} f^0, \quad (3.13)$$

so that the Poisson bracket appearing in Eq. (3.11) becomes

$$\{\mathcal{H}'(\Gamma, t'), f^0(\Gamma)\} = -\beta \dot{A}(\Gamma) f^0(\Gamma) F(t'), \quad (3.14)$$

i.e., a product of minus the inverse temperature  $\beta$  with the time derivative of the operator part  $\dot{A}(\Gamma)$ , the distribution  $f^0(\Gamma)$ , and the time-dependent force function  $F(t)$ .

WE ARE NOW IN POSITION TO FORMULATE THE EXPECTED RESPONSE OF a phase space observable  $B$  to linear order in a perturbation described by the Hamiltonian  $\mathcal{H}'(\Gamma, t)$  defined in Eq. (3.12), i.e.,

$$\langle B(t) \rangle = \int d\Gamma B(\Gamma) \Delta f(\Gamma, t) \quad (3.15)$$

$$= -\beta \int_{-\infty}^t \int d\Gamma B(\Gamma) e^{-i\mathcal{L}^0(t-t')} \dot{A}(\Gamma) f^0(\Gamma) F(t') dt' \quad (3.16)$$

$$= -\beta \int_{-\infty}^t \langle B(\Gamma_t) \dot{A}(\Gamma_t) \rangle_0 F(t') dt', \quad (3.17)$$

where  $\langle \cdot \rangle_0$  denotes a phase-space average with respect to the unperturbed canonical distribution function  $f^0(\Gamma)$ , and the notation implies that for each phase-space point  $\Gamma$  in the ensemble,  $B(\Gamma)$  and  $\dot{A}(\Gamma)$  are evaluated at phase-space points separated in time by  $t - t'$  [61, p. 498]. The time propagation of phase-space points is generated by  $\mathcal{L}^0$  and therefore given by the canonical equations of motion with conserved energy as defined in Eq. (2.66). The phase-space average  $\langle \cdot \rangle_0$  on the other hand corresponds to a canonical ensemble average with respect to the distribution function  $f^0$  defined in Eq. (3.6).

### 3.1.1 Conserved densities and currents

Macroscopic properties of matter are often *extensive*, i.e., they scale with the system size, and can be described by a locally conserved *density* [81]. Taking the general property  $A$  represented by the phase-space observable  $A(\Gamma_t)$  evaluated at a time  $t$  as an example, we define

$$A(\Gamma_t) = \int_V a(\mathbf{r}, \Gamma_t) d^3r, \quad (3.18)$$

where  $a(\mathbf{r}, \Gamma_t)$  is a suitably chosen *local density* associated with the observable  $A$ . The notation  $\Gamma_t$  was introduced in Sec. 2.3.2 to highlight that the quantity is implicitly time-dependent because the phase-space configuration  $\Gamma$  evolves in time. The locally conserved density fulfills a continuity equation

$$\partial_t a(\mathbf{r}, \Gamma_t) = -\nabla \cdot \mathbf{j}(\mathbf{r}, \Gamma_t), \quad (3.19)$$

<sup>2</sup> This can be seen by using the chain rule and the canonical equations of motion:

$$\begin{aligned} \{A, f^0\} &= \sum_i \frac{\partial A}{\partial q_i} \frac{\partial f^0}{\partial p_i} - \frac{\partial A}{\partial p_i} \frac{\partial f^0}{\partial q_i} \\ &= \sum_i \frac{\partial A}{\partial q_i} \frac{\partial f^0}{\partial H^0} \frac{\partial H^0}{\partial p_i} - \frac{\partial A}{\partial p_i} \frac{\partial f^0}{\partial H^0} \frac{\partial H^0}{\partial q_i} \\ &= -\beta f^0 \sum_i \left( \frac{\partial A}{\partial p_i} \dot{q}_i + \frac{\partial A}{\partial q_i} \dot{p}_i \right) \\ &= -\beta f^0 \frac{dA}{dt} \\ &\equiv -\beta f^0 \dot{A}. \end{aligned}$$

where  $\mathbf{j}(\mathbf{r}, \Gamma_t)$  is the associated local current. From the local current, the macroscopic flux is obtained by spatially averaging over the system volume,

$$\mathbf{J}(\Gamma_t) = \frac{1}{V} \int_V d^3r \mathbf{j}(\mathbf{r}, \Gamma_t). \quad (3.20)$$

Likewise we formulate a local version of the perturbing Hamiltonian initially defined in Eq. (3.12),

$$\mathcal{H}'(\Gamma_t, t) = \int d^3r a(\mathbf{r}, \Gamma_t) v(\mathbf{r}, t), \quad (3.21)$$

where  $a(\mathbf{r}, \Gamma_t)$  represents the density of interest as introduced above, and  $v(\mathbf{r}, t)$  is the local driving force coupling to the system via the density  $a(\mathbf{r}, \Gamma_t)$ . The local version of the linear-response formula given in Eq. (3.17) for the expectation value of a given local flux  $\mathbf{j}$  at time  $t$  reads:<sup>3</sup>

$$\langle j^\alpha(\mathbf{r}, t) \rangle = -\beta \int_{-\infty}^t dt' \int_V d^3r' \langle j^\alpha(\mathbf{r}, \Gamma_t) \dot{a}(\mathbf{r}', \Gamma_{t'}) \rangle_0 v(\mathbf{r}', t'). \quad (3.22)$$

The time derivative of the density can be eliminated by using the continuity equation (3.19),  $\dot{a} = -\partial_\beta' j^\beta$  where  $\partial_\beta' = \partial/\partial r'^\beta$ , and integrating by parts, so that

$$\langle j^\alpha(\mathbf{r}, t) \rangle = -\beta \int_{-\infty}^t dt' \int_V d^3r' \langle j^\alpha(\mathbf{r}, \Gamma_t) j^\beta(\mathbf{r}', \Gamma_{t'}) \rangle_0 \partial_\beta' v(\mathbf{r}', t'), \quad (3.23)$$

where a boundary term was neglected.<sup>4</sup> If we now assume the external driving force  $v(\mathbf{r}, t)$  to be constant in time and linearly varying in space such that

$$\partial_\beta v(\mathbf{r}, t) \equiv v_\beta, \quad (3.24)$$

and spatially average over Eq. (3.23) with  $\frac{1}{V} \int_V d^3r$ , we arrive at

**REM:** check sign

$$J^\alpha \equiv \langle J^\alpha \rangle = -\beta V \int_0^\infty dt \langle J^\alpha(\Gamma_t) J^\beta(\Gamma_0) \rangle_0 v_\beta, \quad (3.25)$$

where the stationarity in time was used to shift the lower bound of the integral to  $t = 0$ . This resembles the well-known macroscopic transport equation

$$J^\alpha = L^{\alpha\beta} F_\beta, \quad (3.26)$$

where we identify

$$L^{\alpha\beta} = \frac{V}{k_B} \int_0^\infty dt \langle J^\alpha(\Gamma_t) J^\beta(\Gamma_0) \rangle_0, \quad (3.27)$$

and

$$F_\beta = -\frac{v_\beta}{T}. \quad (3.28)$$

Here,  $J^\alpha$  is the macroscopic generalized current associated with the extensive property  $A$ ,  $F_\beta$  is the thermodynamic force, and  $L^{\alpha\beta}$  is the associated conductance tensor [82, 81].

<sup>3</sup> Take  $B \equiv \mathbf{J}$  with  $\langle B \rangle \equiv \langle \mathbf{J} \rangle = 0$ .

<sup>4</sup> Boundary terms scale proportional to the surface of the integration volume and therefore become negligible in the thermodynamic limit  $V \rightarrow \infty$ .

### 3.1.2 Thermal conductivity

After this general exposition, let us now look at the example of the total energy of the system and its associated energy density,

$$E = \int_V d^3r e(\mathbf{r}) . \quad (3.29)$$

We are interested in the occurring flux in the presence of an inhomogeneous temperature,  $T(\mathbf{r}) = T + \Delta T(\mathbf{r})$ , which couples linearly to the energy density  $e(\mathbf{r})$ , so that<sup>5,6</sup>

$$\mathcal{H}(\Gamma) = \frac{1}{T} \int d^3r T(\mathbf{r}) e(\mathbf{r}, \Gamma) \equiv \mathcal{H}^0(\Gamma) + \mathcal{H}'(\Gamma) , \quad (3.30)$$

with

$$\mathcal{H}'(\Gamma) = \frac{1}{T} \int d^3r \Delta T(\mathbf{r}) e(\mathbf{r}, \Gamma) . \quad (3.31)$$

As earlier in Eq. (3.24), we assume  $\Delta T(\mathbf{r})$  to vary linearly in space, so that the thermodynamic force is given by

$$\nu_\beta = \frac{1}{T} \partial_\beta T(\mathbf{r}) \xrightarrow{(3.28)} F_\beta = -\frac{1}{T^2} (\nabla T)_\beta . \quad (3.32)$$

Using the general transport equation  $\mathbf{J} = L\mathbf{F}$  with the conductance given by Eq. (3.27) and  $F$  as defined above, we obtain

$$J^\alpha = -\kappa^{\alpha\beta} (\nabla T)_\beta , \quad (3.33)$$

where  $\kappa^{\alpha\beta}$  denotes the *thermal conductivity tensor* defined as

$$\kappa^{\alpha\beta} = \frac{V}{k_B T^2} \int_0^\infty dt \langle J^\alpha(\Gamma_t) J^\beta(\Gamma_0) \rangle_0 , \quad (3.34)$$

that is, the Green-Kubo formula for the thermal conductivity  $\kappa$ .

## 3.2 Heat Flux Definition

In order to evaluate the thermal conductivity by means of the Green-Kubo formula, Eq. (3.34), the heat flux observable  $\mathbf{J}(t)$  needs to be defined.<sup>7</sup> We do so by starting from the continuity equation again,

$$\dot{e}(\mathbf{r}) = -\nabla \cdot \mathbf{j}(\mathbf{r}) \quad (3.35)$$

and perform a Fourier transform in space defined by the pair of equations

$$e(\mathbf{r}) = \int d^3q e(\mathbf{q}) e^{i\mathbf{q}\cdot\mathbf{r}} , \quad (3.36)$$

$$\Leftrightarrow e(\mathbf{q}) = \frac{1}{V} \int d^3r e(\mathbf{r}) e^{-i\mathbf{q}\cdot\mathbf{r}} , \quad (3.37)$$

so that the continuity equation can be rewritten for the Fourier components as

$$\dot{e}(\mathbf{q}) = -i\mathbf{q} \cdot \mathbf{j}(\mathbf{q}) . \quad (3.38)$$

We split the total current into a longitudinal, heat-carrying component  $\mathbf{j}_{||}$  and a transverse current  $\mathbf{j}_\perp$ ,

$$\mathbf{j} = \frac{\mathbf{q}}{q} j_{||} + \mathbf{j}_\perp \quad \text{where} \quad \mathbf{q} \cdot \mathbf{j}_\perp = 0 , \quad (3.39)$$

<sup>5</sup>  $E$  and  $\mathcal{H}(\Gamma)$  are related by  $E = \langle \mathcal{H} \rangle$ . The same holds for the occurring densities  $e(\mathbf{r})$  and  $e(\mathbf{r}, \Gamma)$ .

<sup>6</sup> The situation can be viewed as a *stationary nonequilibrium state*. The general theory has been worked out by McLennan [83, 84]. See also the discussion by Zwanzig in Ref. [85].

<sup>7</sup> From now on, all time dependence is to be understood as the implicit time dependence of phase-space observables on the time evolution of a phase-space point,  $f(t) = f(\Gamma_t)$ .

so that

$$\mathbf{j}_{\parallel}(\mathbf{q}) = i \frac{\mathbf{q}}{q^2} \dot{e}(\mathbf{q}) . \quad (3.40)$$

As before, the macroscopic heat flux is given by a spatial average of the (longitudinal) current,

$$\mathbf{J} = \frac{1}{V} \int d^3r \mathbf{j}_{\parallel}(\mathbf{r}) = \mathbf{j}_{\parallel}(\mathbf{q} \rightarrow 0) , \quad (3.41)$$

where it was used that, by definition of the Fourier transform, the integral over the system volume equals the long wavelength limit of the current in reciprocal space. The long wavelength limit for the time derivative of the local energy density can be obtained by Taylor expanding in  $\mathbf{q}$

$$\dot{e}(\mathbf{q}) = \lim_{\mathbf{q} \rightarrow 0} \int d^3r \left( \chi - i\mathbf{q} \cdot \mathbf{r} + (\mathbf{q} \cdot \mathbf{r})^2 + \dots \right) \dot{e}(\mathbf{r}) , \quad (3.42)$$

where the first term in the expansion is excluded since the total energy  $E$  is conserved in time.<sup>8</sup> After multiplying  $\dot{e}$  with  $i\mathbf{q}/q^2$  according to Eq. (3.40) and taking the  $\mathbf{q} \rightarrow 0$  limit, we obtain

$$\mathbf{J}(t) = \frac{1}{V} \int d^3r \mathbf{r} \dot{e}(\mathbf{r}, t) = \frac{1}{V} \frac{d}{dt} \int d^3r \mathbf{r} e(\mathbf{r}, t) , \quad (3.43)$$

i. e., the heat flux is given as the first moment of the time derivative of the local energy density. Alternatively, one can view the heat flux as the time derivative of the energy barycenter by moving the time derivative outside the integral.

In force-field approaches, it is common to adopt the latter approach and split the energy density into atomic contributions  $E = \sum_I E_I$  as

$$e(\mathbf{r}, t) = \sum_I E_I(t) \delta(\mathbf{r} - \mathbf{R}_I(t)) . \quad (3.44)$$

The heat flux is then given by [86]

$$\mathbf{J}(t) = \frac{1}{V} \frac{d}{dt} \sum_I E_I(t) \mathbf{R}_I(t) = \mathbf{J}^{\text{pot}}(t) + \mathbf{J}^{\text{kin}}(t) , \quad (3.45)$$

with a *potential* or *virial* current

$$\mathbf{J}_{\text{pot}}(t) = \frac{1}{V} \sum_I \dot{E}_I(t) \mathbf{R}_I(t) , \quad (3.46)$$

and a *kinetic* or *convective* current

$$\mathbf{J}_{\text{kin}}(t) = \frac{1}{V} \sum_I E_I(t) \dot{\mathbf{R}}_I(t) . \quad (3.47)$$

While the kinetic flux becomes increasingly important and even dominant in liquids and gases with substantial convection [87], it is typically neglected in non-convective solids, as it was shown several times in the literature that its contribution to thermal conductivity is orders of magnitude lower compared to the virial flux [88, 89]. However, also in solids it is not strictly vanishing, and discarding the kinetic flux as defined in Eq. (3.47) therefore is an approximation which we discuss in the following.

<sup>8</sup> Using the Leibniz rule,

$$\int d^3r \dot{e}(\mathbf{r}) = \frac{d}{dt} \int d^3r e(\mathbf{r}) = \frac{d}{dt} E = 0 .$$

### 3.2.1 Gauge invariance of heat flux definitions

As seen above, the local current is only defined up to a non-heat carrying contribution  $\mathbf{j}_\perp$ . Likewise, the energy density is only defined up to terms that keep the total energy integral unchanged. The choice of a local energy partitioning as, e. g., given by Eq. (3.44) is therefore not unique, and different partitioning schemes will lead to differing heat fluxes. However, the thermal conductivity obtained after integrating the respective autocorrelation functions will be the same. In particular, Ercole *et al.* have shown in Ref. [90] that two heat fluxes differing by the time derivative of a *bounded* vector field,

$$\tilde{\mathbf{J}}(t) = \mathbf{J}(t) + \frac{d}{dt} \mathbf{P}(t), \quad (3.48)$$

can differ in time, and in general also their autocorrelation functions will differ. The thermal conductivity obtained from both fluxes will however be the same, which can be viewed as a *gauge invariance principle* for the heat flux. This property can be used to discard terms from the flux that do not contribute to the thermal conductivity and thereby reduce noise [17].

AS AN EXAMPLE OF IMMEDIATE PRACTICAL IMPORTANCE, we rewrite the heat flux expression presented in Eq. (3.45) as

$$\mathbf{J}(t) = \frac{1}{V} \sum_I \mathbf{R}_I^0 \dot{E}_I + \frac{1}{V} \frac{d}{dt} \sum_I \mathbf{U}_I E_I, \quad (3.49)$$

where the instantaneous positions  $\mathbf{R}(t)$  are split into a fixed reference  $\mathbf{R}^0$  and a displacement field  $\mathbf{U}(t)$  [91]. When all the atomic displacements  $\{ \mathbf{U}_I \}$  are bounded, i. e., in the absence of convective terms, the second term in Eq. (3.49) fulfills the condition of being the time derivative of a bounded vector field and therefore does not contribute to the thermal conductivity by the gauge invariance principle. Using the definition of the kinetic flux in Eq. (3.47), the second, non-contributing term can be written as

$$\frac{1}{V} \frac{d}{dt} \sum_I \mathbf{U}_I E_I = \mathbf{J}_{\text{kin}} + \mathbf{J}_{\text{res}} \quad (3.50)$$

with a residual flux

$$\mathbf{J}_{\text{res}}(t) = \frac{1}{V} \sum_I \mathbf{U}_I \dot{E}_I. \quad (3.51)$$

This makes clear that, in the absence of convection, the contribution of  $\mathbf{J}_{\text{kin}}$  to thermal conductivity does not vanish alone, as argued in the previous section, but the *joint* contribution of  $\mathbf{J}_{\text{kin}}$  and  $\mathbf{J}_{\text{res}}$  vanishes. By the reverse argument, one can argue that whenever the contribution of  $\mathbf{J}_{\text{kin}}$  to thermal conductivity can be neglected in a solid, the contribution of  $\mathbf{J}_{\text{res}}$  must vanish as well. In consequence, the heat flux in non-diffusing solids is given by

$$\mathbf{J}^{\text{non-convective}}(t) = \frac{1}{V} \sum_I \mathbf{R}_I^0 \dot{E}_I \approx \mathbf{J}_{\text{pot}}(t), \quad (3.52)$$

where the difference between left- and right-hand side is given by  $\mathbf{J}_{\text{res}}$  which can be neglected whenever the kinetic flux can be neglected, as discussed above. The exact definition for the non-diffusive current in terms of fixed reference positions  $\{ \mathbf{R}_I^0 \}$  was already used by Ladd and coworkers in Ref. [92]

to simplify the occurring expressions. An in-depth discussion of the subtleties arising in the definition of an exact expression for the non-convective heat flux in solids can be found in Sec. 2.3.1 and appendix A of Ref. [93].

A FINAL REMARK CONCERNING THE HEAT FLUX DEFINITION is in order: One might argue that the expression in Eq. (3.52) is a total time derivative of  $\mathbf{P} = \frac{1}{V} \sum_I \mathbf{R}_I^0 E_I$ , and therefore vanishes by the aforementioned gauge invariance principle as well. However, this is not the case in an infinite solid, since the atomic configuration  $\{\mathbf{R}_I\}$  is not bounded. The sum over atomic positions is therefore not well defined in the first place and remains to be understood as a symbolic representation of an actual energy partitioning scheme that needs to be cast in a boundary-insensitive form for any practical application of Eq. (3.52).<sup>9</sup>

*Wasn't this discussed  
in the literature by  
several people*

<sup>9</sup> The author thanks Stefano Baroni for an insightful discussion clarifying this point.

*I think also in  
Carbogno et al.*

### 3.3 Ab initio Heat Flux

The above formulas are readily applied when empirical force fields are used to describe the atomic interactions, as an atomic partitioning of the total energy is trivial in that case, although care must be taken in deriving the correct formulae nevertheless [94, 95]. An *ab initio* derivation of heat flux on the other hand was a long-standing problem because it was not clear how an expression like Eq. (3.52) can be obtained when no atomic partitioning is available [96]. This problem was solved when Marcologno *et al.* and Carbogno *et al.* independently arrived at well-defined heat flux expressions in *ab initio* frameworks [14, 15]. We adopt the latter approach in the following, but present a derivation that slightly differs from Ref. [15], i. e., by starting from Eq. (3.43) instead of Eq. (3.45), and using the phase-space formalism developed in this chapter.

To evaluate Eq. (3.43),<sup>10</sup> we need a definition of the time derivative of the energy density. We do so by first going back to the many-body Hamiltonian for a configuration  $\Gamma = (\mathbf{R}, \mathbf{P})$  given by

$$\mathcal{H}(\Gamma) = \sum_I \frac{\mathbf{P}_I^2}{2M_I} + \mathcal{V}(\mathbf{R}) \equiv \int d^3r e(\mathbf{r}, \Gamma), \quad (3.53)$$

where  $e(\mathbf{r}, \Gamma)$  is an appropriately chosen energy density yielding the total energy of the given system. Accordingly, the time derivative of the entire expression reads

$$\dot{\mathcal{H}}(\Gamma) = \sum_I \mathbf{F}_I \cdot \dot{\mathbf{R}}_I + \sum_I \frac{\partial \mathcal{V}(\mathbf{R})}{\partial \mathbf{R}_I} \cdot \dot{\mathbf{R}}_I \equiv \int d^3r \dot{e}(\mathbf{r}, \Gamma). \quad (3.54)$$

Since the energy is conserved, the time derivative of the Hamiltonian vanishes, and therefore  $\dot{e}(\mathbf{r}, \Gamma)$  needs to integrate to zero. As explained in Sec. 1.4.1, the force derived from the BO potential-energy surface  $\mathcal{V}(\mathbf{R})$  appearing in Eq. (3.54) has a nuclear and an electronic contribution given by the two terms

<sup>10</sup> Recall Eq. (3.43):

$$\mathbf{J}(t) = \frac{1}{V} \int d^3r \mathbf{r} \dot{e}(\mathbf{r}, t).$$

in Eq. (1.38), so that

$$\mathbf{F}_I = \int d^3r \mathbf{f}_I^{\text{el}}(\mathbf{r}) + \sum_{J \neq I} \mathbf{F}_{IJ}^{\text{Nuc}}, \quad \text{with} \quad (3.55)$$

$$\mathbf{f}_I^{\text{el}}(\mathbf{r}) = -n(\mathbf{r})Z_I \frac{\mathbf{R}_I - \mathbf{r}}{|\mathbf{R}_I - \mathbf{r}|^3}, \quad \text{and} \quad (3.56)$$

$$\mathbf{F}_{IJ}^{\text{Nuc}} = Z_I Z_J \frac{\mathbf{R}_I - \mathbf{R}_J}{|\mathbf{R}_I - \mathbf{R}_J|^3}. \quad (3.57)$$

Therefore, Eq. (3.54) can be written as the sum of three terms that sum to zero as required,

$$\dot{\mathcal{H}}(\Gamma) = \underbrace{\sum_I \mathbf{F}_I \cdot \dot{\mathbf{R}}_I}_{I)} - \underbrace{\sum_I \int d^3r \mathbf{f}_I^{\text{el}}(\mathbf{r}) \cdot \dot{\mathbf{R}}_I}_{II)} - \underbrace{\sum_{\substack{I,J \\ J \neq I}} \mathbf{F}_{IJ}^{\text{Nuc}} \cdot \dot{\mathbf{R}}_I}_{III)}. \quad (3.58)$$

We use these terms to define three contributions to the local density  $\dot{e}(\mathbf{r})$  as

$$\text{I): } \dot{e}_{\text{kin}}(\mathbf{r}) = \sum_I \mathbf{F}_I \cdot \dot{\mathbf{R}}_I \delta(\mathbf{R}_I - \mathbf{r}), \quad (3.59a)$$

$$\text{II): } \dot{e}_{\text{el}}(\mathbf{r}) = - \sum_I \mathbf{f}_I^{\text{el}}(\mathbf{r}) \cdot \dot{\mathbf{R}}_I, \quad (3.59b)$$

$$\text{III): } \dot{e}_{\text{Nuc}}(\mathbf{r}) = - \sum_{\substack{I,J \\ J \neq I}} \mathbf{F}_{IJ}^{\text{Nuc}} \cdot \dot{\mathbf{R}}_I \delta(\mathbf{R}_J - \mathbf{r}). \quad (3.59c)$$

Pictorially, the kinetic contribution  $\dot{e}_{\text{kin}}(\mathbf{r})$  is assigned to atom  $I$  in the sum, the electronic contribution  $\dot{e}_{\text{el}}(\mathbf{r})$  is assigned to the local electron density at  $\mathbf{r}$  and is therefore a local quantity per definition, and the nuclear contribution  $\dot{e}_{\text{Nuc}}(\mathbf{r})$  is assigned to atom  $J$  in analogy to the electronic case. It is easily verified that the sum of these contributions integrate to zero. Their first moment however gives a non-vanishing heat flux by Eq. (3.43), i. e.,

$$\mathbf{J}(\Gamma) = \frac{1}{V} \int d^3r \mathbf{r} (\dot{e}_{\text{kin}}(\mathbf{r}) + \dot{e}_{\text{el}}(\mathbf{r}) + \dot{e}_{\text{Nuc}}(\mathbf{r})) \quad (3.60)$$

$$= \frac{1}{V} \sum_I \left( \mathbf{R}_I \mathbf{F}_I \cdot \dot{\mathbf{R}}_I - \int d^3r \mathbf{r} \mathbf{f}_I^{\text{el}}(\mathbf{r}) \cdot \dot{\mathbf{R}}_I - \sum_{J \neq I} \mathbf{R}_J \mathbf{F}_{IJ}^{\text{Nuc}} \cdot \dot{\mathbf{R}}_I \right). \quad (3.61)$$

By using Eq. (3.55) in the first summand of the above equation, Eq. (3.56) for the second, and Eq. (3.57) for the third, we arrive at

$$J^\alpha(\Gamma) = \sum_{I,\alpha} \frac{Z_I}{V} \left\{ \sum_{J \neq I} Z_J \frac{(R_I^\alpha - R_J^\alpha)(R_I^\beta - R_J^\beta)}{|\mathbf{R}_I - \mathbf{R}_J|^3} - \int d^3r n(\mathbf{r}) \frac{(R_I^\alpha - r^\alpha)(R_I^\beta - r^\beta)}{|\mathbf{R}_I - \mathbf{r}|^3} \right\} \dot{R}_I^\beta, \quad (3.62)$$

where the Cartesian indices of the expressions have been written out explicitly. As shown in Ref. [15], this expression can be written in terms of atomic contributions to the stress tensor  $\sigma$  defined by

$$\sigma^{\alpha\beta} = -\frac{\partial V(\mathbf{R})}{\partial \varepsilon_{\alpha\beta}} = \sum_I \sigma_I^{\alpha\beta}, \quad (3.63)$$

with

$$\sigma_I^{\alpha\beta} = \frac{Z_I}{V} \left\{ \sum_{J \neq I} Z_J \frac{(R_I^\alpha - R_J^\alpha)(R_I^\beta - R_J^\beta)}{|\mathbf{R}_I - \mathbf{R}_J|^3} - \int d^3r n(\mathbf{r}) \frac{(R_I^\alpha - r^\alpha)(R_I^\beta - r^\beta)}{|\mathbf{R}_I - \mathbf{r}|^3} \right\}. \quad (3.64)$$

This can be rationalized by using the same steps that led to the Hellmann-Feynman expression for the position derivative in Eq. (1.38), and noting that

$$\frac{\partial f(\mathbf{r}_1 - \mathbf{r}_2)}{\partial \varepsilon_{\alpha\beta}} = \frac{\partial f(\mathbf{r}_1 - \mathbf{r}_2)}{\partial r_1^\alpha} (r_1^\beta - r_2^\beta), \quad (3.65)$$

as discussed in detail in Ref. [97].

The atomic stress contributions  $\sigma_I$  are functionals of the electron density and atomic configuration and therefore can be computed in *ab initio* frameworks, for example in the all-electron, numeric atomic orbital electronic structure code *FHI-aims* [98, 97].<sup>11</sup> The final result for the *ab initio* heat flux used in this work is therefore

$$\mathbf{J}_{ai}(t) = \sum_I \sigma_I(t) \dot{\mathbf{R}}_I, \quad (3.66)$$

where  $\sigma_I(t)$  is Eq. (3.64) evaluated for the configuration  $\mathbf{R}(t)$ .

TO CONCLUDE, WE LIKE TO POINT OUT that by using the time derivative of the energy density, we neglect convective contributions to the flux from the very beginning. The present *ab initio* heat flux is therefore valid for solids with vanishing or negligible mass diffusion, as discussed earlier.

### 3.4 Heat Flux in the Harmonic Approximation

We now discuss heat flux in the harmonic approximation. This work was pioneered by Debye and Peierls [99, 100], with a formal derivation first presented by Hardy [101]. It allows to deduct several important conclusions about thermal transport in solids, and the insights will later be used to boost convergence of non-perturbative *ab initio* Green Kubo simulations.

WE START FROM THE GAUGE-INVARIANT HEAT FLUX EXPRESSION for solids as defined in Eq. (3.52), i. e.,

$$\mathbf{J}(t) = \frac{1}{V} \sum_I \mathbf{R}_I^0 \dot{E}_I. \quad (3.67)$$

The atomic energy contribution  $E_I$  expressed in mass-scaled displacements  $\{\mathbf{u}_I\}$  and momenta  $\{\mathbf{p}_I\}$  reads

$$E_I = \frac{1}{2} p_I^2 + \frac{1}{2} \sum_J D_{I\alpha,J\beta} u_I^\alpha u_J^\beta, \quad (3.68)$$

with the dynamical matrix  $D_{IJ}$ , so that

$$\begin{aligned} \dot{E}_I &= \sum_J \dot{p}_{I\alpha} p_I^\alpha + \frac{1}{2} \sum_J D_{I\alpha,J\beta} (p_I^\alpha u_J^\beta + u_I^\alpha p_J^\beta) \\ &= -\frac{1}{2} \sum_J D_{I\alpha,J\beta} (p_I^\alpha u_J^\beta - u_I^\alpha p_J^\beta). \end{aligned} \quad (3.69)$$

<sup>11</sup> We mention in passing that in practical implementations, additional contributions to  $\sigma_I$  need to be computed to account for basis set dependent Pulay terms just like in the computation of other gradients of the total energy. See again Ref. [97] for a comprehensive list of the arising terms.

The harmonic forces are

$$\dot{p}_{I\alpha} = -\frac{\partial E}{\partial u_I^\alpha} = -\sum_J D_{I\alpha,J\beta} u_J^\beta,$$

and in mass-weighted coordinates

$$\dot{u}_I^\alpha = p_I^\alpha.$$

Using this expression for the time derivative of the atom-resolved harmonic energy in Eq. (3.67) leads to a heat flux of the form

$$\mathbf{J}_{\text{ha}}(t) = -\frac{1}{2V} \sum_{IJ} (\mathbf{R}_I^0 - \mathbf{R}_J^0) D_{I\alpha, J\beta} p_I^\alpha(t) u_J^\beta(t), \quad (3.70)$$

which is boundary-insensitive as required since only differences of positions enter. We express the displacements  $\{\mathbf{u}_I\}$  and velocities  $\{\mathbf{p}_I\}$  in terms of the complex mode amplitudes  $a_s(t)$  introduced in Eq. (2.97) in Sec. 2.2.5,

$$\mathbf{u}_I(t) = \sum_s \frac{1}{\sqrt{2\omega_s}} \mathbf{e}_{sI}^* [a_{-s}^\dagger(t) + a_s(t)], \quad \text{and} \quad (3.71)$$

$$\mathbf{p}_I(t) = \sum_s i\sqrt{\frac{\omega_s}{2}} \mathbf{e}_{sI} [a_{-s}^\dagger(t) - a_s(t)], \quad (3.72)$$

where we remind of the shorthand notation  $s = (b, \mathbf{q})$  with band index  $b$  and wave vector  $\mathbf{q}$  summarized in the joint mode label  $s$ . Using the mode amplitudes, the harmonic heat flux reads

$$\mathbf{J}_{\text{ha}}(t) = \frac{1}{2V} \sum_{ss'} \mathbf{v}_{ss'} \omega_s (a_{-s}^\dagger + a_s) (a_{s'}^\dagger - a_{-s'}), \quad (3.73)$$

with the generalized group velocity

$$\mathbf{v}_{ss'} = \frac{1}{2\sqrt{\omega_s \omega_{s'}}} \sum_{IJ} i(\mathbf{R}_I^0 - \mathbf{R}_J^0) D_{I\alpha, J\beta} e_{s,I\alpha}^* e_{s',J\beta}. \quad (3.74)$$

Using that  $\mathbf{v}(-\mathbf{q}) = -\mathbf{v}(\mathbf{q})$ , the diagonal contribution ( $s = s'$ ) to the flux reads

$$\mathbf{J}_{\text{ha-diag}}(t) = \frac{1}{V} \sum_s \mathbf{v}_s \omega_s a_s^\dagger(t) a_s(t) \equiv \frac{1}{V} \sum_s E_s(t) \mathbf{v}_s, \quad (3.75)$$

where the mode energy  $E_s = \omega_s a_s^\dagger a_s$  was used. This result is the familiar phonon heat flux operator (when setting  $\hbar = 1$ ), where  $a_s^\dagger(t) a_s(t) \equiv n_s(t)$  is the instantaneous mode occupation as defined in Eq. (2.94) [100, 101, 91].

### 3.4.1 Thermal conductivity derived from the harmonic flux

With the harmonic heat flux at hand, we are now in position to discuss certain limits of the resulting thermal conductivity. For example, it is straightforward to show that the thermal conductivity of a purely harmonic system is infinite. We demonstrate the reasoning for the case of the diagonal contribution to the heat flux  $\mathbf{J}_{\text{ha-diag}}$  given by Eq. (3.75), which we simply denote by  $J$  in the following, omitting Cartesian components for clarity when no confusion can arise.

As discussed in detail in Sec. 3.1.2, the thermal conductivity is given by the Kubo formula

$$\kappa = \frac{V}{k_B T^2} \int_0^\infty dt \langle J(t) J \rangle, \quad (3.76)$$

where the last quantity in  $\langle \cdot \rangle$  will be evaluated at  $t = 0$ . The autocorrelation function for the diagonal harmonic heat flux defined in Eq. (3.75) reads

$$\langle J(t) J \rangle = \frac{1}{V^2} \sum_{ss'} v_s v_{s'} \langle E_s(t) E_{s'} \rangle, \quad (3.77)$$

With the shorthand notation  $s = (b, \mathbf{q})$  and  $I = (i, \mathbf{L})$ , we find that the diagonal term  $\mathbf{v}_s = \mathbf{v}_{ss'}$  is indeed the group velocity:

$$\begin{aligned} \mathbf{v}_s &= \frac{\partial \omega_s}{\partial \mathbf{q}} = \frac{1}{2\omega_s} \frac{\partial \omega_s^2}{\partial \mathbf{q}} \\ &= \frac{1}{2\omega_s} \sum_{ij} e_{s,ia}^* \frac{\partial D_{i\alpha, j\beta}(\mathbf{q})}{\partial \mathbf{q}} e_{s,j\beta} \\ &= \frac{1}{2\omega_s} \sum_{I,J} i(\mathbf{R}_I^0 - \mathbf{R}_J^0) D_{I\alpha, J\beta} e_{s,I\alpha}^* e_{s,J\beta}. \end{aligned}$$

where the  $E_s(t)$  are chosen such that  $\langle E_s \rangle = 0$ . The thermal conductivity is obtained by integrating the autocorrelation function. We get

$$\kappa^{\alpha\beta} = V \sum_{ss'} c_{ss'} v_s^\alpha v_{s'}^\beta \tau_{ss'} , \quad (3.78)$$

where we define the generalized lifetime

$$\tau_{ss'} = \int_0^\infty dt G_{ss'}(t) \quad (3.79)$$

with the normalized mode-energy autocorrelation function<sup>12</sup>

$$G_{ss'}(t) = \frac{\langle E_s(t)E_{s'} \rangle}{\langle E_s E_{s'} \rangle} = \frac{\langle a_s^\dagger(t)a_s(t)a_{s'}^\dagger a_{s'} \rangle}{\langle n_s \rangle \langle n_{s'} \rangle} - 1 , \quad (3.80)$$

and the generalized heat capacity

$$c_{ss'} = \frac{1}{k_B T^2} \langle E_s E_{s'} \rangle . \quad (3.81)$$

**IN THE PERFECTLY HARMONIC CASE**, the mode-energy autocorrelation function  $G_{ss'}$  can be evaluated analytically by noting that the expectation value  $\langle \cdot \rangle$  can be viewed as a functional integral with the distribution function  $f = e^{-\beta \sum_s \omega_s a_s^\dagger a_s}$  and can therefore be evaluated by means of a Wick theorem [91]. Keeping only the non-vanishing pairings, we have<sup>13</sup>

$$\langle a_s^\dagger(t)a_s(t)a_{s'}^\dagger a_{s'} \rangle = \langle n_s \rangle \langle n_{s'} \rangle + g_s(t)g_s^*(t)\delta_{ss'} , \quad (3.82)$$

where  $\langle n_s \rangle = \frac{k_B T}{\omega_s}$  is the equipartition mode occupation, and the one-particle Green's function  $g_s(t)$  is defined by

$$g_s(t)\delta_{ss'} \equiv \langle a_s^\dagger(t)a_{s'} \rangle = e^{i\omega_s t} \langle n_s \rangle \delta_{ss'} , \quad (3.83)$$

where the time evolution of the complex amplitudes  $a_s^\dagger(t) = e^{i\omega_s t} a_s^\dagger$  was used. It is apparent that the product  $g_s(t)g_s^*(t)$  is not time-dependent, and the heatflux autocorrelation function defined in Eq. (3.77) is therefore given by

$$\langle J(t)J \rangle = \sum_s \langle J_s^2 \rangle . \quad (3.84)$$

Consequently, the harmonic heatflux autocorrelation function integrates to infinity and the thermal conductivity  $\kappa$  diverges.

**A FINITE THERMAL CONDUCTIVITY** is obtained when the phonons are allowed to interact, for example by introducing impurities, electron-phonon interactions, or self interactions via anharmonic contributions to the potential-energy surface. If the perturbation is weak, it can be expressed by modified Green's functions [102]

$$g_s(t) = e^{i(\omega_s + \Sigma_s)t} \langle n_s \rangle , \quad (3.85)$$

where  $\Sigma_s$  is the phonon self energy. Assuming the self energy to be purely imaginary,  $\Sigma_s = i\Gamma_s$ , we have

$$G_s(t) = \frac{g_s(t)g_s^*(t)}{\langle n_s \rangle^2} = e^{-2\Gamma_s t} \equiv e^{-t/\tau_s} , \quad (3.86)$$

<sup>12</sup> The  $-1$  comes from choosing  $\langle E_s \rangle = 0$ .

<sup>13</sup> In the context of complex field integration, the Wick theorem reads [102]

$$\langle ABCD \rangle = \langle AB \rangle \langle CD \rangle + \langle AC \rangle \langle BD \rangle + \langle AD \rangle \langle BC \rangle .$$

Pairings with a non-equal number of “creators”  $a^\dagger$  and “annihilators”  $a$  vanish identically because of the symmetry of the distribution function  $f$ .

where he have defined the lifetime  $\tau_s = 1/2\Gamma_s$ . The heatflux autocorrelation function now reads

$$\langle J(t)J \rangle = \sum_s \langle J_s^2 \rangle e^{-t/\tau_s}, \quad (3.87)$$

and the thermal conductivity integrates to a finite value given by<sup>14</sup>

$$\kappa_{\text{ha}}^{\alpha\beta} = V k_B \sum_s v_s^\alpha v_s^\beta \tau_s, \quad (3.88)$$

which is the single-mode ( $s = s'$ ) approximation to the general  $\kappa$  defined in Eq. (3.78) with the classical value for the mode heat capacity  $c_s = k_B$ .

The same expression can be found from a Boltzmann transport approach using the *single-mode relaxation-time approximation*, and extension to quantum-mechanical distributions is straightforward [103].

### 3.4.2 Mode lifetimes from perturbation theory

In low-order perturbation theory, the phonon self energy can be obtained by approximating the potential-energy surface as

$$\mathcal{V}(\mathbf{R}) \approx V^{(2)}(\mathbf{R}) + V^{(3)}(\mathbf{R}), \quad (3.89)$$

where  $V^{(2)}(\mathbf{R})$  denotes the harmonic potential, and  $V^{(3)}(\mathbf{R})$  is obtained by expanding the potential  $\mathcal{V}(\mathbf{R})$  to third order. Further assuming the cubic contribution  $V^{(3)}(\mathbf{R})$  to be small compared to the harmonic part, the inverse mode lifetime  $\tau_s^{-1} = 2\Gamma_s$  is given by the Fermi Golden Rule expression [104]

$$2\Gamma_s = \frac{\pi\hbar^2}{4\omega_s} \sum_{pq} \frac{|\mathcal{V}_{spq}^{(3)}|^2}{\omega_p \omega_q} \left[ \frac{1}{2} (1 + n_p + n_q) \delta(\omega_s - \omega_p - \omega_q) + (n_p - n_q) \delta(\omega_s + \omega_p - \omega_q) \right], \quad (3.90)$$

where  $\mathcal{V}_{spq}^{(3)}$  is the cubic potential transformed to phonon eigenstates. This equation and the single-mode expression for  $\kappa$ , Eq. (3.88), serve as the basis for most *ab initio* studies of thermal conductivity in insulating solids in recent years [13, 105, 91]. More recently, extensions of the perturbation-expansion approach up to fourth order have been presented [106, 107, 108, 109]. While higher-order perturbation theory can improve the description of heat transport in anharmonic solids [110, 111], its applicability is currently limited to simple, highly-symmetric materials because of the scaling of quartic force constants with system size, see the discussion in appendix D of Ref. [108].

### 3.4.3 Mode lifetimes from molecular dynamics simulations

In *ab initio* molecular dynamics, we have direct access to the non-perturbative dynamics of the nuclear system. Lifetimes can therefore be extracted by straightforward application of Eq. (3.79) and (3.80). To circumvent the problem of brute-force integrating the time integral in the evaluation of the lifetime expression, we use the theoretical discussion in terms of Green's functions from above to approximate the normalized mode-energy autocorrelation function  $G_{ss'}(t)$  as

$$G_{ss'}(t) \approx G_s(t) \delta_{ss'} = \frac{\langle E_s(t)E_s \rangle}{\langle E_s^2 \rangle} \approx e^{-t/\tau_s}, \quad (3.91)$$

↑  
how good is this?  
Who has analyzed this?

<sup>14</sup> Using

$$\begin{aligned} J_s &= \omega_s v_s n_s, \\ \langle n_s \rangle &= \frac{k_B T}{\omega_s}. \end{aligned}$$

↑ again:  
 Please make it clear:  
 What of the above  
 fact is new?  
 What idea is  
 from you?

strange wording



from which the lifetime  $\tau_s$  can be obtained by fitting  $G_s(t)$  to an exponential function. This is exemplified for a simulation of MgO at 300 K in Fig. 3.1

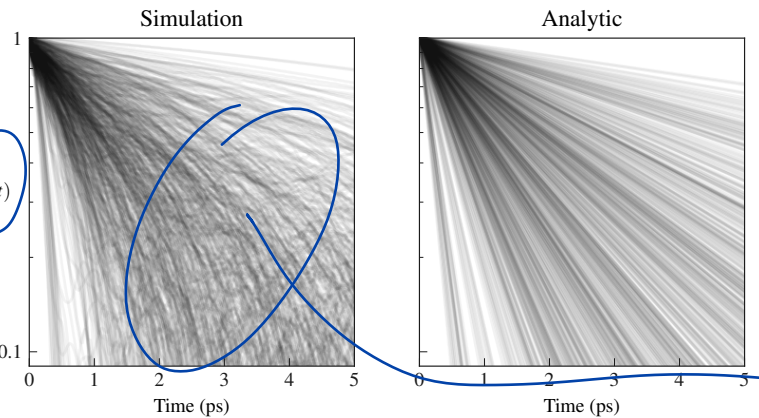


Figure 3.1: Fit of mode lifetimes for MgO at 300 K. Simulation performed with a timestep of 5 fs for a simulation time of 60 ps. The size of the simulation cell was 216 atoms. Left: normalized mode-energy autocorrelation function  $G_s(t)$  as obtained from the simulation. Right: Analytic expression of the form  $G_s(t) = e^{-t/\tau_s}$  after fitting mode lifetimes  $\tau_s$ . The y-axis is logarithmic such that exponential functions appear as straight lines.

**REM:** Interpolation here?

**REM:** Remove plot?

### 3.5 Ab initio Green Kubo

Building on the previous sections, we are now in position to present the *ab initio* Green Kubo approach adopted in this work. The approach comprises four steps:

1. The thermal conductivity  $\kappa_{ai}$  is obtained by numerically evaluating the Green-Kubo integral using the *ab initio* heat flux  $\mathbf{J}_{ai}(t)$  defined in Eq. (3.66) evaluated during microcanonical *ab initio* molecular dynamics simulations.
2. The harmonic contribution  $\kappa_{ha}$  to the thermal conductivity is computed from the simulation data by using lifetimes extracted via Eq. (3.91) in the BTE-type formula for  $\kappa_{ha}$  given in Eq. (3.88).
3. The quantities used to compute  $\kappa_{ha}$ , i.e., the group velocities and lifetimes, are interpolated to dense q-point grids in reciprocal space to achieve an extrapolation of the harmonic thermal conductivity to bulk limit,  $\kappa_{ha\text{-bulk}}$  [15]. The interpolation works by assuming that  $\tau_b(\mathbf{q}) = \lambda_b(\mathbf{q})\omega_b^{-2}(\mathbf{q})$  with a weakly q-dependent function  $\lambda_b(\mathbf{q})$  obtained by linearly interpolating the lifetimes obtained at commensurate q-points. The scaling of lifetimes with  $\omega_s^{-2}$  is rooted in basic phonon theory as developed by Herring [112] and holds especially for long-ranged acoustic modes which are difficult to describe in finite-sized *ab initio* molecular dynamics simulations.
4. The interpolation scheme yields a finite-size corrected thermal conductivity via

$$\kappa_{\text{bulk}} = \kappa_{ai} - \kappa_{ha} + \kappa_{ha\text{-bulk}} . \quad (3.92)$$

We temporarily restore the full notation  $s = (b, \mathbf{q})$  to make the q-dependence of the appearing quantities explicit.

} was this explained?

### 3.6 Conclusion

It is apparent from the presentation above that a low-order expansion of the potential-energy surface combined with low-order perturbation expressions represents a wealth of approximations that certainly hold for some materials [92, 13, 113], but are questionable or even outright unjustified for others. In particular, dynamical effects such as phase transitions to dynamically stabilized crystal structures ( $\text{ZrO}_2$  [114, 15],  $\text{SrTiO}_3$  [115]), spontaneous defect formation (e.g., in noble metal halides [116, 117]), or simply a soft bonding and therefore strong anharmonicity ( $\text{NaCl}$  [108],  $\text{NaBr}$  [118]) are inherently absent in such a description. These are cases where a non-perturbative description of thermal transport is necessary. By the same argument, largely harmonic materials like silicon or diamond fulfill the requirements for a perturbative treatment, and brute-force simulating the nuclear dynamics via MD techniques is therefore not necessary.

FOR THESE REASONS, IT IS DESIRABLE TO PRE-CATEGORIZE MATERIALS in terms of their “anharmonic strength”, especially when one attempts to screen materials space for a significant amount of materials, as this allows to choose appropriate simulation techniques for each system. We present a systematic approach towards “measuring anharmonicity” in the next chapter.



## **Part II**

# **Applications**



# 4

## Anharmonicity

*only vib.*

As we have seen in the previous chapter, thermal conductivity is an anharmonic effect — in a purely harmonic system, thermal conductivity is infinite. We have also discussed methods to assess thermal transport in materials, either via the Green-Kubo approach, or via perturbation theory. In perturbation theory, the potential energy is expanded to third or fourth order, and these terms are used to compute the change of phonon properties, in particular, their lifetimes. From a computational perspective, the two approaches have different strengths: Perturbative techniques are ideally suited when the anharmonicity is weak, i. e., there is a well defined reference configuration and the harmonic terms in the potential dominate the dynamical evolution of the system. However, in strongly anharmonic systems, these basic assumptions can be violated, for example because the reference configuration changes qualitatively during phase transitions, or the anharmonic terms in the potential become too strong to be described by the asymptotic perturbation series [102, p. 53]. The Green-Kubo technique on the other hand does not require approximations to the potential ~~energy~~ surface, and therefore naturally includes dynamical effects of arbitrary anharmonic strength. It is ideally suited in situations where the anharmonicity is strong, i. e., when the basic assumptions of perturbation theory are not satisfied. It is therefore desirable to *measure* the “degree of anharmonicity” to enable a discussion of anharmonicity on a quantitative basis.

You should tell who has done this, and for what systems

### 4.1 Definition of Anharmonicity

In accordance with the previous chapters, classical nuclear dynamics within the Born-Oppenheimer approximation is governed by the Hamiltonian

$$\mathcal{H}(\mathbf{P}, \mathbf{R}) = \sum_I \frac{\mathbf{P}_I^2}{2M_I} + \mathcal{V}(\mathbf{R}), \quad (4.1)$$

where  $\mathbf{P}$  and  $\mathbf{R}$  denote the atomic momenta and coordinates. Using an expansion of the full potential  $\mathcal{V}(\mathbf{R})$  in the displacements  $\mathbf{U}$  around a reference configuration  $\mathbf{R}^0$  as discussed in Chp. 2, the potential can be split into a harmonic contribution,  $\mathcal{V}^{(2)}$ , and a second term capturing all anharmonic effects,  $\mathcal{V}^A$ ,

$$\mathcal{V}(\mathbf{R}) = \mathcal{V}^{(2)}(\mathbf{R}) + \mathcal{V}^A(\mathbf{R}). \quad (4.2)$$

*Das Wort  
ist nicht sinnvoll.  
Welche anderen Kräfte  
gibt es denn?*

In the classical limit, the dynamical evolution of the nuclei is determined by the potential through the atomic forces as defined Eq. (2.55),

$$M_I \ddot{\mathbf{R}}_I = -\frac{\partial \mathcal{V}}{\partial \mathbf{R}_I} \equiv \mathbf{F}_I, \quad (4.3)$$

i.e., Newton's equations of motion. By linearity of the differential, the forces can therefore be split into harmonic and anharmonic contributions as well,

$$\mathbf{F}_I = \mathbf{F}_I^{(2)} + \mathbf{F}_I^A. \quad (4.4)$$

The division of potential and forces into harmonic and anharmonic contributions is depicted for a one-dimensional potential in Fig. 4.1.

## 4.2 Anharmonicity measure

We base the definition of a measure for anharmonicity on the forces, for two reasons: First, because the forces give microscopic insight, as they can be resolved per atom. Second, the forces are statistically easier to describe, since per configuration  $\mathbf{R}$ , there are  $3N$  force components  $\mathbf{F} = (\mathbf{F}_1, \dots, \mathbf{F}_N)$ . In terms of the force contributions defined in Eq. (4.4), we define a *measure of anharmonicity*,  $\sigma^A$ , in the following way:

$$\sigma^A(T) = \sqrt{\frac{\sum_{I,\alpha} \langle (F_{I,\alpha}^A)^2 \rangle_T}{\sum_{I,\alpha} \langle (F_{I,\alpha})^2 \rangle_T}}, \quad (4.5)$$

where  $F_{I,\alpha}^{(A)}$  is the  $\alpha$  component of the (anharmonic) force on atom  $I$  and  $\langle \cdot \rangle_T$  denotes a thermodynamic average at temperature  $T$ . The measure  $\sigma^A$  quantifies the anharmonic strength in terms of the standard deviation of the distribution of anharmonic force components at a given temperature,  $\sigma[F^A]_T$ , normalized by the standard deviation of the actual force distribution,  $\sigma[F]_T$ . The standard deviation of a force distribution is defined as

$$\sigma[F]_T = \sqrt{\frac{1}{3N} \sum_{I,\alpha} \langle F_{I,\alpha}^2 \rangle_T}. \quad (4.6)$$

The effect of normalizing the distribution of forces is shown in Fig. 4.2 for the two exemplary materials already discussed in the context of phonon dispersions in Sec. 2.2.6, silicon, and the orthorombic perovskite  $\text{KCaF}_3$ . Only after normalizing the forces, a meaningful comparison between materials or across temperatures can be achieved.

FOR THE TWO EXEMPLARY MATERIALS, WE SHOW THE JOINT NORMALIZED DISTRIBUTIONS OF FORCE AND ANHARMONIC FORCE CONTRIBUTIONS in Fig. 4.3, where the thermodynamic sampling is performed by *ab initio* molecular dynamics simulations at 300 K. In this representation,  $\sigma^A$  is given by the standard deviation of the distribution in y-direction, as indicated by the dashed horizontal lines in the plot. The distribution of anharmonic force components is more than twice as broad for the perovskite  $\text{KCaF}_3$  compared to silicon, with a  $\sigma_{\text{KCaF}_3}^A = 0.36$  compared to  $\sigma_{\text{Si}}^A = 0.15$ . This can be interpreted in the sense that 36 % of the forces stem from anharmonic contributions in  $\text{KCaF}_3$ , and 15 % in silicon. Furthermore, strongly anharmonic

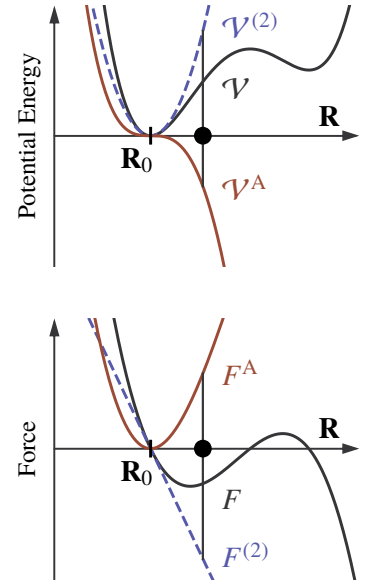


Figure 4.1: Upper: Sketch of a one-dimensional potential-energy surface  $\mathcal{V}$  (solid black), its harmonic approximation  $\mathcal{V}^{(2)}(\mathbf{R})$  (dashed blue), and the anharmonic contribution  $\mathcal{V}^A(\mathbf{R})$  (solid red). Lower: The force  $F(\mathbf{R})$  given by the derivative of  $\mathcal{V}$  (black), the force  $F^{(2)}$  stemming from  $\mathcal{V}^{(2)}(\mathbf{R})$  (blue), and the anharmonic contribution  $F^A = F - F^{(2)}$  (red), cf. Eq. (4.4).

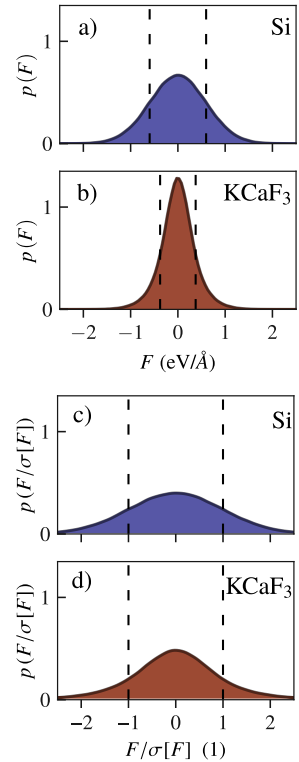


Figure 4.2: Force component distribution before and after normalization with the width of the distribution  $\sigma[F]$ .  $p(F)$  denotes the probability to find a force component  $F_{I,\alpha}$  of strength  $F$  in the material. Panel a) and b) show the distribution before normalization, c) and d) after normalization. Dashed vertical lines denote the standard deviation of the displayed distribution.

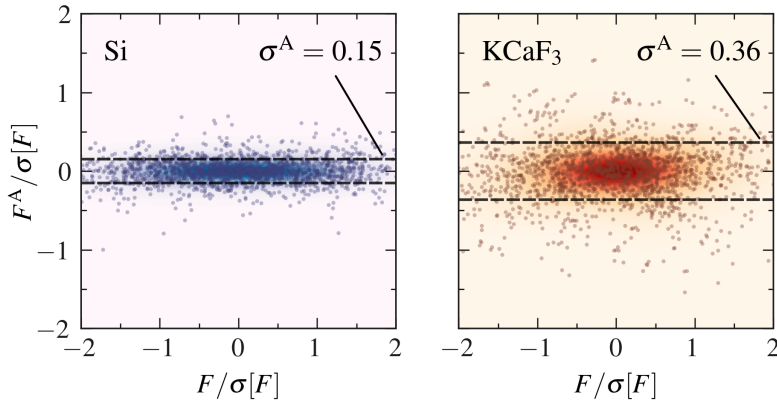


Figure 4.3: Normalized anharmonic force components versus normalized force components. Dashed horizontal lines: Width of the distribution estimated from standard deviation. Individual dots are force components sampled during an *ab initio* MD simulations.

force contributions with a strength of  $0.5 \sigma[F]$  or more are nearly absent in silicon with a probability of  $< 0.01\%$ , whereas anharmonic forces of this strength in KCaF<sub>3</sub> occur with a much higher probability of  $\sim 16.5\%$ .

THE ANHARMONICITY MEASURE DEFINED IN EQ. (4.5) can also be evaluated for subsets of the dynamical degrees of freedom, e. g., per chemical species, as shown in Fig. 4.4. In the example of KCaF<sub>3</sub>, this analysis shows

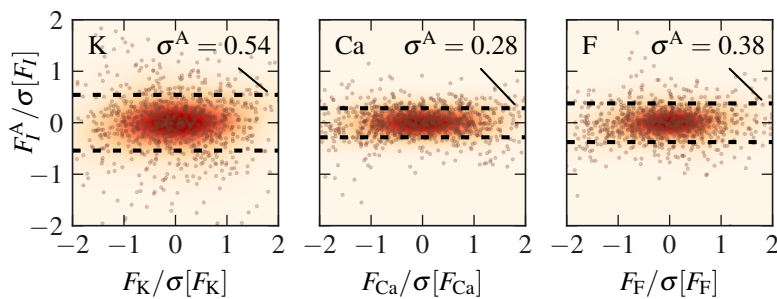


Figure 4.4: Normalized anharmonic force components versus normalized force components. Dashed horizontal lines: Width of the distribution estimated from standard deviation.

that the calcium (Ca) atoms occupying the vertices of the unit cell are comparatively well described by the harmonic model, whereas the description of potassium (K) is particularly bad. This can be explained by the phase-transition mechanism observed in KCaF<sub>3</sub>: Above 560 K, the material becomes cubic, and the octahedral displacement of fluorine (F) is removed, as shown in Fig. 4.5. This tilt also affects the potassium atoms, which are displaced from their high-temperature reference position in the orthoromantic phase, and are therefore located in a shallow potential already at room temperature, well below the phase transition [48, 119].

IT IS INSTRUCTIVE TO EVALUATE THE ANHARMONICITY FOR SINGLE CONFIGURATIONS, be it snapshots in time during molecular dynamics simulations, or when using other sampling approaches, e. g, harmonic Monte Carlo samples as defined in Eq. (2.89). The sample-resolved anharmonicity is given

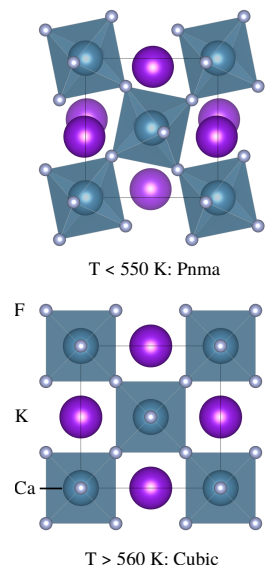


Figure 4.5: KCaF<sub>3</sub> in the low-temperature Pnma (top) and high-temperature cubic phase (bottom). Both structures are viewed along the long  $b$ -axis.

in analogy to Eq. (4.5) as

$$\sigma^A[\mathbf{R}] = \sqrt{\frac{\sum_{I,\alpha} (F_{I,\alpha}^A)^2}{\sum_{I,\alpha} (F_{I,\alpha})^2}}. \quad (4.7)$$

While we will discuss “time-resolved anharmonicity” in detail at a later point, we show the evaluation of  $\sigma^A$  for samples generated by Eq. (2.89) in Fig. 4.6. The analysis shows that a decent estimate of  $\sigma^A$  can be obtained

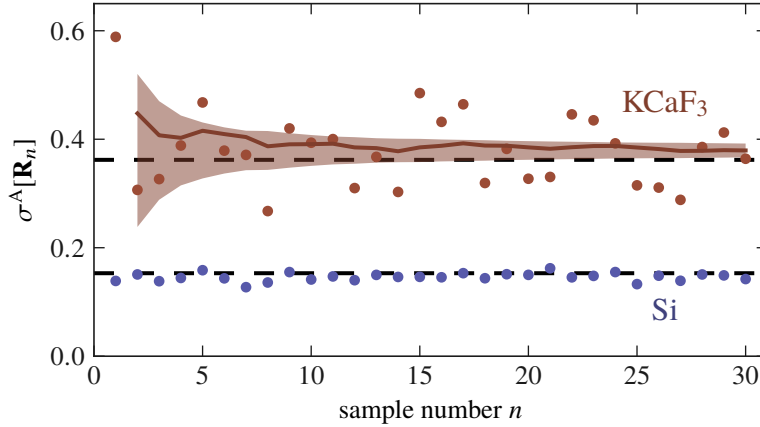


Figure 4.6: Anharmonicity measure  $\sigma^A$  evaluated for individual atomic configurations obtained from Eq. (2.89). Dots:  $\sigma^A[\mathbf{R}_n]$  for individual samples; Red line: Cumulative average. Black dashed line:  $\sigma^A$  from aiMD. Shadowed region: Convergence estimated by standard error.

from the harmonic sampling analysis with few samples. Especially in silicon, each individual harmonic sample yields a  $\sigma^A$  within 99 % of the reference value obtained by MD simulations for several hundred simulation time steps, which is indicated by the dashed horizontal line. For the more anharmonic  $\text{KCaF}_3$ , the harmonic sampling with 30 samples yields an estimated value of  $\sigma_{\text{est.}}^A = 0.38$ , which differs from the MD value ( $\sigma^A = 0.36$ ) by about 5 %. A distinction between largely harmonic materials like silicon, and anharmonic materials like  $\text{KCaF}_3$ , is therefore possible with very few samples.

Motivated by this fact, we investigated the possibility to estimate  $\sigma^A$  based on a single sample, as suggested by Zacharias and Giustino in Ref. [120]: They use a single, deterministic sample to probe the most probable part of the harmonic distribution by choosing  $\zeta_s = (-1)^s$  instead of a random distribution in Eq. (2.89). We denote anharmonicity measures obtained by such a “one-shot” approach by  $\sigma_{\text{OS}}^A$  in the following. As shown in Fig. 4.7, the one-shot samples provide very good estimates for silicon in the entire temperature range from 200 K to 800 K, which can be expected due to the largely harmonic nature of silicon. For  $\text{KCaF}_3$ , the agreement is decent in the temperature range from 200 to 400 K, at least within the limits of the harmonic sampling approach as discussed in the previous paragraph. Above 500 K, the difference to the reference value from MD simulations increases, which is due to the phase transition mechanism in  $\text{KCaF}_3$  discussed earlier: A prediction of anharmonicity across phase transitions cannot be expected from simple harmonic sampling approaches, because the entire reference frame for the harmonic model changes when a phase transition occurs. The phase transition mechanism of  $\text{KCaF}_3$  and implications for the anharmonicity measure are further discussed in Ref. [121].

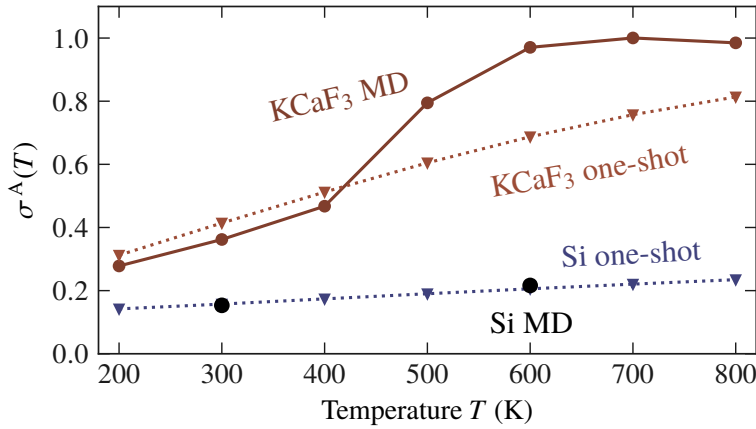


Figure 4.7:  $\sigma^A$  as a function of temperature obtained from MD simulations (black circles) and one-shot sampling (triangles connected by dashed curves)

needs to be assessed for a diverse set of materials, especially if one aims to use this scheme to screen for anharmonicity in material space. As shown in Fig. 4.8 for a set of 63 materials, the one-shot sampling is reliable within  $\pm 10\%$  for all materials in the set, up to a value of about  $\sigma^A \approx 0.2$ . For larger

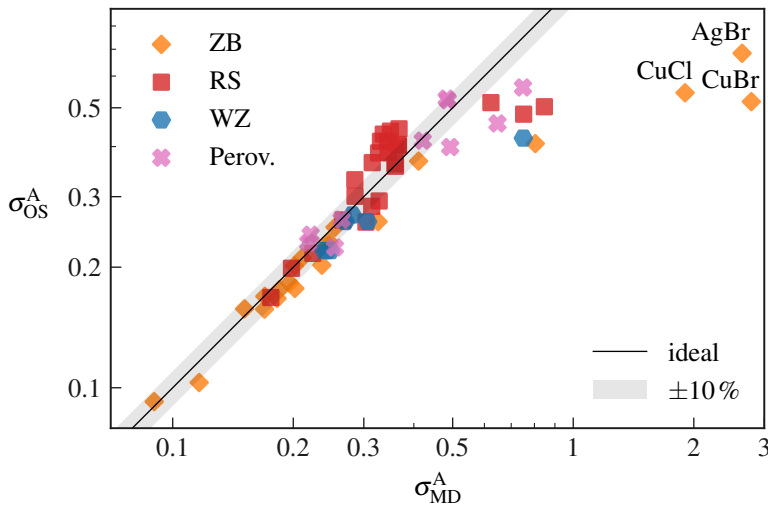


Figure 4.8: Comparison of the anharmonicity measure obtained from MD simulations and one-shot sampling (OS) for 63 materials at 300 K. The set comprises 25 rock salt (RS), 21 zincblende (ZS), 7 wurtzite (WZ), and 10 orthorombic perovskite (Perov.) materials. The diagonal line denotes perfect agreement between MD and OS, and the green area denotes a 10% error margin to guide the eye. Data was taken from Ref. [121].

values of  $\sigma^A$ , the deviation can become larger, especially for the group of rock salt materials with  $\sigma^A \approx 0.35$  (red squares) where the one-shot sampling overestimates  $\sigma^A$  by about 20 %. Nevertheless, the agreement is qualitatively correct up to values of about  $\sigma^A \approx 0.4$ , after which materials begin to show effects not captured by the harmonic sampling, e.g., phase transitions as discussed earlier for  $\text{KCaF}_3$ . In particular, the three highlighted noble metal halides  $\text{AgBr}$ ,  $\text{CuCl}$ , and  $\text{CuBr}$  deviate strongly. These materials tend towards non-perturbative effects during the MD simulation such as spontaneous defect formation [121], which is a dynamical effect impossible to describe by any fixed-reference harmonic model. We will discuss the nature of these effects in more detail later in Sec. 4.5.

To conclude, we point out that also in the case of non-trivial dynamical effects such as defect formation, the estimated anharmonicity scores  $\sigma_{\text{OS}}^A$  are larger than  $\gtrsim 0.5$ , and therefore indicate strong anharmonicity. A qualitative classification of strong anharmonicity in terms of one-shot sampling is there-

fore possible for all materials in the set, while quantitative agreement is only achieved for harmonic materials with  $\sigma^A \lesssim 0.2$ .

### 4.3 Anharmonicity and thermal conductivity

Based on the qualitative discussion of thermal transport in Sec. 3.4.1, one can expect that stronger anharmonicity leads to shorter phonon lifetimes and therefore lower thermal conductivity. We tested this hypothesis for a list of 47 materials where experimental references were available [11, 122]. The results are shown in Fig. 4.9. The analysis reveals an inverse power law relation-

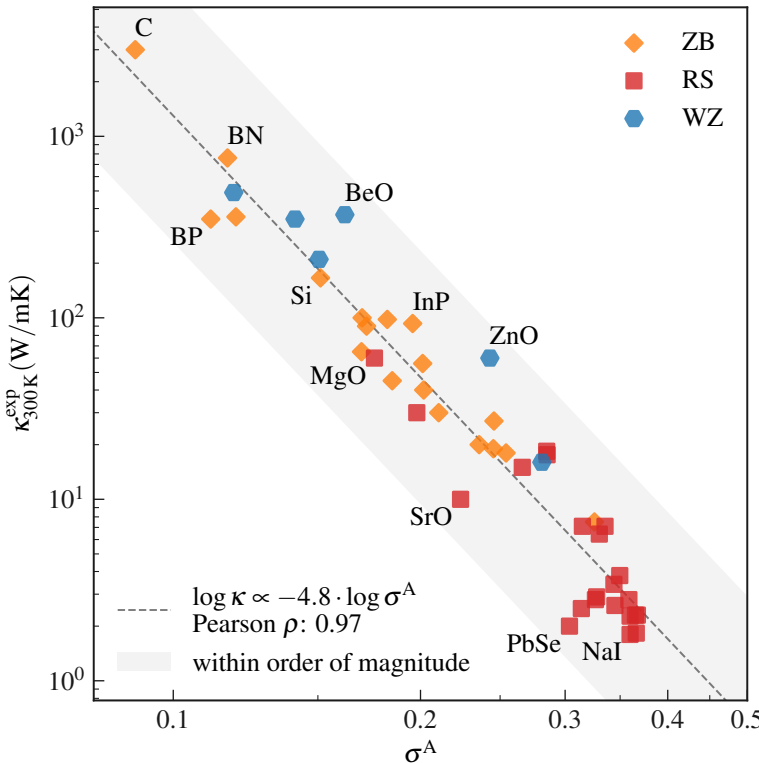


Figure 4.9: Experimental thermal conductivity at room temperature,  $\kappa_{300\text{K}}^{\text{exp}}$ , versus one-shot measure of anharmonicity,  $\sigma_{\text{OS}}^A$ , and fully anharmonic  $\sigma_{\text{MD}}^A$  for materials with  $\sigma_{\text{OS}}^A > 0.2$ . The dashed diagonal line indicates a power law fit for the data. The grey area denotes values of  $\kappa$  which agree with the fit within an order of magnitude. The dataset contains 47 materials, 22 rock salt (RS), 19 zincblende (ZB), and 6 wurtzite (WZ) structures. Experimental data from Ref. [11, 122].

ship between thermal conductivity and anharmonicity for the materials in the dataset. Given that just a single descriptor is used, i.e., the estimated anharmonicity score, and no further vibrational properties as commonly employed in semi-empirical models for thermal conductivity [123, 122], this correlation is surprisingly good and indicates that  $\sigma^A$  captures some essential physics relevant to heat transport.

THE MOST IMPORTANT MESSAGES FROM FIG. 4.9 CAN BE SUMMARIZED AS FOLLOWS, adopting the definition suggested by Morelli and Slack to define “high thermal conductivity” as  $\kappa \gtrsim 50 \text{ W/mK}$  [11]:

1. Largely harmonic materials with  $\sigma^A \approx 0.1$ , like diamond (C), boron nitride (BN), or boron phosphide (BP) can be expected to be good thermal conductors with  $\kappa \gtrsim 100 \text{ W/mK}$ .
2. Strongly anharmonic materials with  $\sigma^A \gtrsim 0.3$  can be expected to be poor thermal conductors with  $\kappa \lesssim 10 \text{ W/mK}$ .

3.  $\sigma^A$  has a strong correlation with thermal conductivity across the entire dataset, but nevertheless only a rough estimate can be made solely based on  $\sigma^A$ , especially in the middle region with  $\sigma^A \simeq 0.2$ . This can be seen by comparing strontium oxide (SrO) with  $\kappa = 10 \text{ W/mK}$  and  $\sigma^A = 0.22$ , and zinc oxide (ZnO) with  $\kappa = 60 \text{ W/mK}$  and  $\sigma^A = 0.24$ , or beryllium oxide (BeO) with  $\kappa = 370 \text{ W/mK}$  and  $\sigma^A = 0.16$  to magnesium oxide (MgO) with  $\kappa = 60 \text{ W/mK}$  and  $\sigma^A = 0.18$ . These pairs of materials differ only slightly in their estimated anharmonicity, but still quite strongly in the thermal conductivity. Nevertheless, the correct order of magnitude of  $\kappa$  as indicated by the grey area in Fig. 4.9 can always be predicted for the investigated materials.

THESE FINDINGS SUGGEST THE FOLLOWING APPROACH towards screening material space in search for thermal insulators: Estimate the anharmonicity for materials of interest and discard the largely harmonic ones, as they will be good thermal conductors most of the time. Of course, the reverse approach can be pursued when searching for materials with potentially high thermal conductivity.

#### 4.4 Candidate Materials

Using the measure  $\sigma^A$ , we have identified a set of 118 binary and ternary materials for further investigation with the *ab initio* Green Kubo (aiGK) approach. The materials comprise five lattice types and 12 space groups as summarized in Fig. 4.10. Since we are mainly interested in thermal insulators as candidate thermoelectric and thermal barrier coating materials, we have discarded largely harmonic materials with  $\sigma^A < 0.17$  from the set, and focus on anharmonic strengths  $\sigma^A > 0.2$  with a mean of  $\sigma^A = 0.31$  and a median of  $\sigma^A = 0.29$ . A histogram displaying the distribution of  $\sigma^A$  values is shown in Fig. 4.11. All values are given with respect to room temperature,

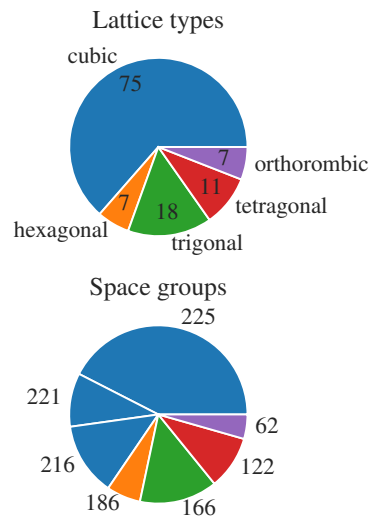


Figure 4.10: Lattice types and space groups represented in the dataset. Space groups not shown in the pie chart: 56, 61, 160, 164, 206, with one representative each.

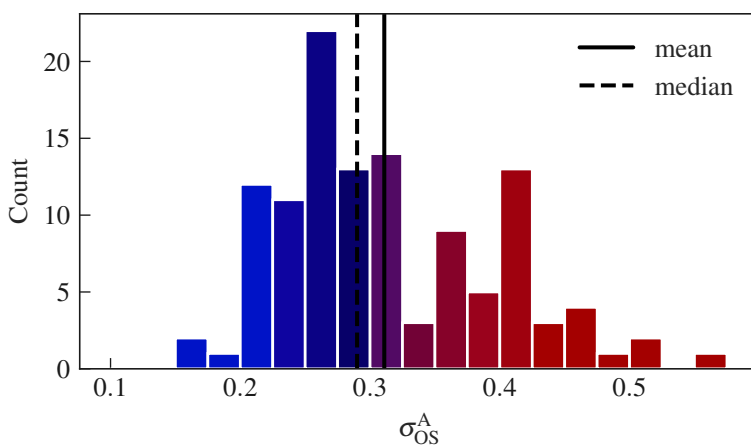


Figure 4.11: Histogram of  $\sigma_{OS}^A$  values samples for the 118 chosen materials

as this is the regime where the most experimental reference is available to benchmark the aiGK method and to showcase the approach. In total, there are experimental reference values for 45 materials available. The references are given in Tab. I.1 in appendix I.

**TODO:** Include full list of materials with reference in appendix

The materials have been chosen based on the following criteria:

1. Material has to have an experimentally known stable phase at room temperature,
2. material has to be semiconductor or insulator with a bandgap large enough to prevent partial occupations of the valence band during molecular dynamics simulations,
3. the most heavy element considered is Barium ( $Z = 56$ ), after which relativistic effects beyond the “zeroth order regular approximation” cannot be neglected [124, 125, 126].

#### 4.5 Dynamical effects

As shown in the initial screening of material space presented in Ref. [121], strongly anharmonic materials with  $\sigma^A > 0.3$  are prone to exhibiting non-trivial dynamical effects such as metastable defect formation and precursors of structural phase transitions.

WE CARRIED OUT *AB INITIO* MOLECULAR DYNAMICS SIMULATIONS<sup>1</sup> for each of the candidate materials introduced in the previous chapter to see whether the materials exhibit such non-trivial dynamical effects. These dynamical effects can be detected by using a time-resolved anharmonicity measure as defined in Eq. (4.7), i. e., by evaluating the anharmonicity measure for each sample during the MD with  $\sigma^A(t) = \sigma^A[\mathbf{R}(t)]$ , and evaluating fluctuations of  $\sigma^A(t)$  in terms of its standard deviation  $\text{std}[\sigma^A]$  evaluated along a given trajectory. A comparison of  $\sigma^A$  values obtained by one-shot sampling,  $\sigma_{\text{OS}}^A$ , and molecular dynamics,  $\sigma_{\text{MD}}^A$ , is shown in Fig. 4.12. Materials with a standard deviation larger than  $\text{std}[\sigma_{\text{MD}}^A] > 0.01$  are highlighted and labeled.

<sup>1</sup> Computational settings: PBEsol function and *light default* basissets. Time step 4-5 fs based on the highest harmonic vibrational frequency, total simulation time at least 30 ps. Lattice expansion accounted for by minimizing the pressure in the simulation cell according to the scheme outlined in Sec. E.2. Full details given in appendix H.

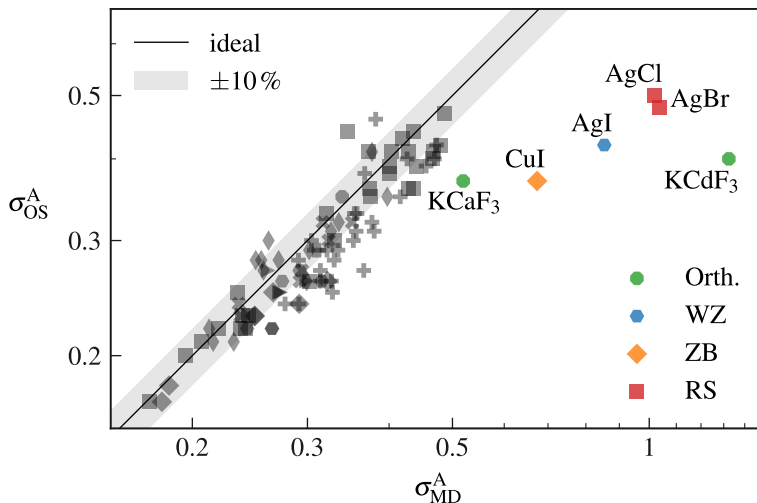


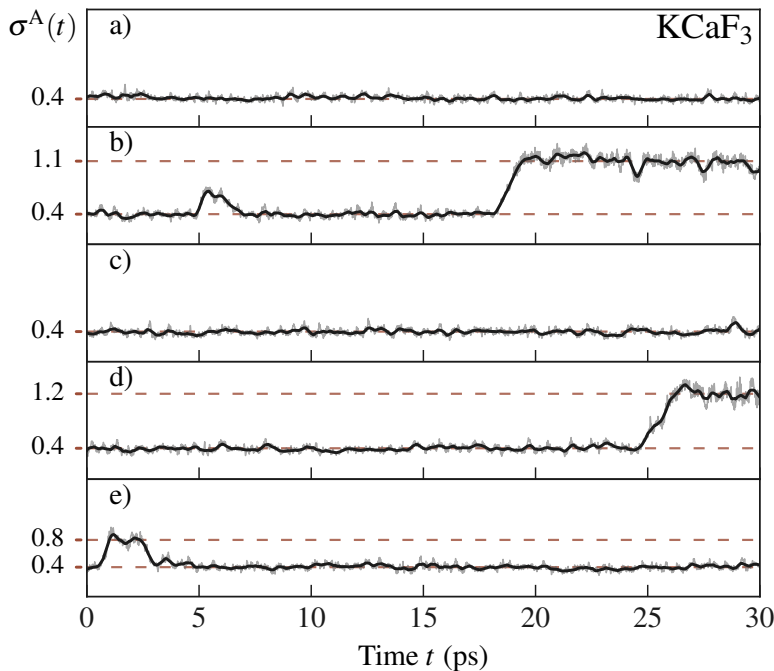
Figure 4.12:  $\sigma^A$  values obtained by one-shot sampling (OS) and molecular dynamics simulations (MD) in comparison. Materials with significant fluctuations of the time-resolved anharmonicity measure  $\sigma^A(t)$  are highlighted and labeled.

We discuss the nature of these effects for  $\text{KCaF}_3$ ,  $\text{CuI}$ ,  $\text{AgI}$ , and  $\text{AgCl}$  in the following.  $\text{AgBr}$  and  $\text{KCdF}_3$  are omitted because they behave qualitatively similar to  $\text{AgCl}$  and  $\text{KCaF}_3$ , respectively.

The discussion is meant to highlight the prevalence of non-trivial dynamical effects that violate one basic assumption of phonon theory, i. e., the assumption of well-defined and stationary reference positions for all atoms in a given phase. Another key insight is that the observed effects are precursors of phase transitions known to occur in these materials at higher temperatures, which means that their onset is observed on the microscopic scale during the dynamic evolution already several 100 K below the phase transition temperature. From a methodological point of view, we show how the time-resolved anharmonicity can be used to uncover and explain the nature of the underlying dynamical effect.

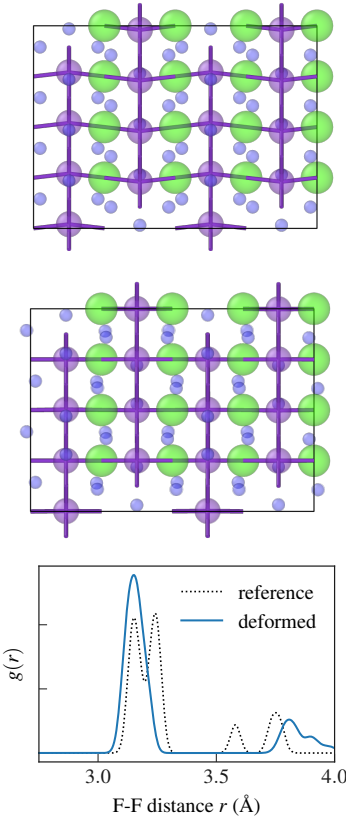
### 4.5.1 KCaF<sub>3</sub>

KCaF<sub>3</sub> is the perovskite material already discussed in some detail in Sec. 4.2, where the octahedral tilting mechanism typical for this class of materials, and the phase transition phenomenology were presented [48, 119, 50]. In total, we performed five *NVE* simulations for KCaF<sub>3</sub>, with a simulation time of 30 ps each. The time resolved anharmonicity measure is displayed for each of those trajectories in Fig. 4.13. We find that in three of the five trajectories,  $\sigma^A(t)$  jumps between the reference value of  $\sigma^A \approx 0.4$ ,<sup>2</sup> and increased values between  $\sigma^A \approx 0.8$  and  $\sigma^A \approx 1.2$ .



<sup>2</sup> We round to 1 decimal point in the following, which is completely sufficient for the discussion of intermittent jumps.

Figure 4.13: Time-resolved anharmonicity measure  $\sigma^A(t)$  for orthorombic KCaF<sub>3</sub> in five molecular dynamics runs of 30 ps length. Increased values of  $\sigma^A(t)$  are found in three trajectories (b, d, e).



THE NATURE OF THE UNDERLYING DYNAMICAL EFFECTS can be resolved by time-averaging the positions  $\mathbf{R}(t)$ ,

$$\mathbf{R}_{\text{avg}} = \langle \mathbf{R}(t) \rangle_t , \quad (4.8)$$

for the time spans in which  $\sigma^A(t)$  is increased. Performing this time average for time spans where  $\sigma^A(t) < 0.5$ , i. e., in situations in which no increase is seen, one recovers the initial orthorombic structure shown in Fig. 4.14 (top figure). When averaging trajectory b) for the time where  $\sigma^A(t) \approx 1.1$ , the resulting structure is more symmetric, with an approximately tetragonal arrangement of atoms. This can be seen by focusing on the potassium sub-lattice (purple atoms connected by sticks) in Fig. 4.14 (middle). The increased symmetry is further revealed by noting that the fluorine cage becomes more ordered, as shown in terms of the F-F pair distribution function in Fig. 4.14 (bottom). This phenomenon can be viewed as a precursor of the phase transitions towards tetragonal and cubic phases known to occur in this material at temperatures higher than 560 K [48, 119, 121]. However, at 300 K, well

Figure 4.14: Precursor of phase transition in KCaF<sub>3</sub>. Upper panel: The reference orthorombic structure viewed in (010) direction. The orthorombic displacement of the potassium sub-lattice (violet balls connected by sticks) is clearly visible. Middle panel: When  $\sigma^A(t) \approx 1.1$ , the potassium sub-lattice temporarily adopts a tetragonal shape. Also the fluorine atoms (small blue balls) reduce their tilt consequently. Lower panel: Radial distribution function  $g(r)$  for the fluorine atoms in the orthorombic reference and deformed structure: The number of distinct peaks reduces, reflecting an increase in symmetry when the orthorombic tilt reduces.

below the transition temperature, this configuration only occurs sporadically on the time scale of several picoseconds during the simulation, and is therefore not fully stabilized.

#### 4.5.2 CuI

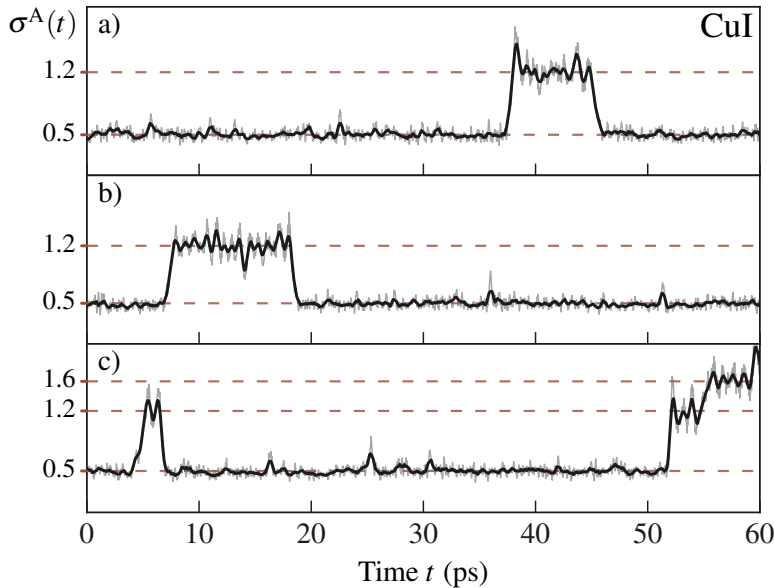


Figure 4.15: Time-resolved anharmonicity measure  $\sigma^A(t)$  for zincblende CuI in three molecular dynamics runs of 60 ps length. Increased values of  $\sigma^A(t)$  are found in all three trajectories.

Copper iodide (CuI), also known as marshite, is a simple material with fcc lattice of the zincblende type. This phase is also known as the  $\gamma$  phase ( $\gamma$ -CuI). The time-resolved anharmonicity measures are shown in Fig. 4.15 for three trajectories of 60 ps simulation time. The characteristic features are the jumps in  $\sigma^A(t)$  from values of  $\sigma^A(t) \approx 0.5$  to  $\sigma^A(t) \approx 1.2$  or 1.6. In the simulated time period, these values are taken for 3 to 12 ps, before the initial value of  $\sigma^A(t) \approx 0.5$  is restored.

As in the case of KCaF<sub>3</sub>, we compare two time-averaged structures in Fig. 4.16: A time average with respect to the entire simulation time reveals the perfect zincblende structure of CuI which corresponds to the minimum of the potential energy surface. When averaging over the time span where  $\sigma^A(t) \approx 1.2$ , however, the average structure has one Cu atom displaced along the (111) direction. Viewing the supercell in (110) direction, the displacement is clearly visible (Fig. 4.16, middle). This means that the Cu occupies a metastable interstitial site at the given position for the respective time period. When  $\sigma^A(t)$  is restored to the base value of  $\sigma^A(t) \approx 0.5$ , the Cu atom moves back to the high-symmetry reference position within the zincblende structure. The third trajectory shown in Fig. 4.15 c) evolves to a situation where  $\sigma^A \approx 1.6$ . This corresponds to a situation, where more than one defects forms (Fig. 4.16, bottom).

$\gamma$ -CuI IS KNOWN TO UNDERGO A PHASE TRANSITION TO A SUPERIONIC CONDUCTING  $\beta$  PHASE above 643 K [127, 128, 129, 130]. It is very likely that the defect formation observed in the aiMD simulations at 300 K are

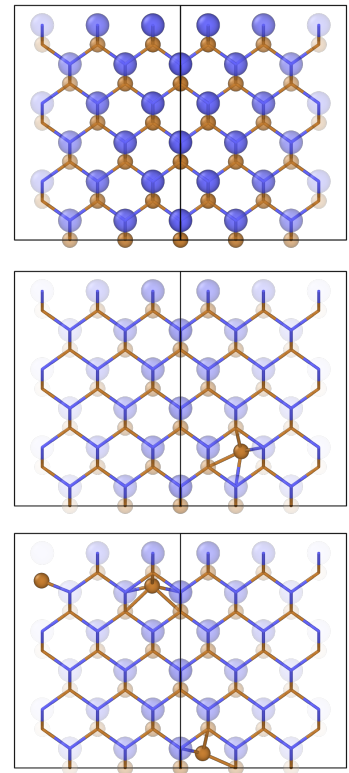


Figure 4.16: CuI viewed in (110) direction. Top: High-symmetry zincblende structure. Middle: Copper ion in lower-right quadrant moves into interstitial site along (111) direction when  $\sigma^A(t) \approx 1.2$ . Bottom: Several defects form when  $\sigma^A(t) \approx 1.6$ .

precursors of this phase transition, but too infrequent at this temperature to destabilize the fcc lattice of the  $\gamma$  phase.

#### 4.5.3 AgI

Wurtzite silver iodide ( $\beta$ -AgI), or iodargyrite, is another transition metal halide that shares some similarities with  $\beta$ -CuI discussed in the previous section [129]. It is known to transition into the superionic conducting  $\alpha$  phase above  $\sim 420$  K [131, 129, 117], and was in fact one of the earliest studied materials exhibiting this phenomenon [132, 133, 134].

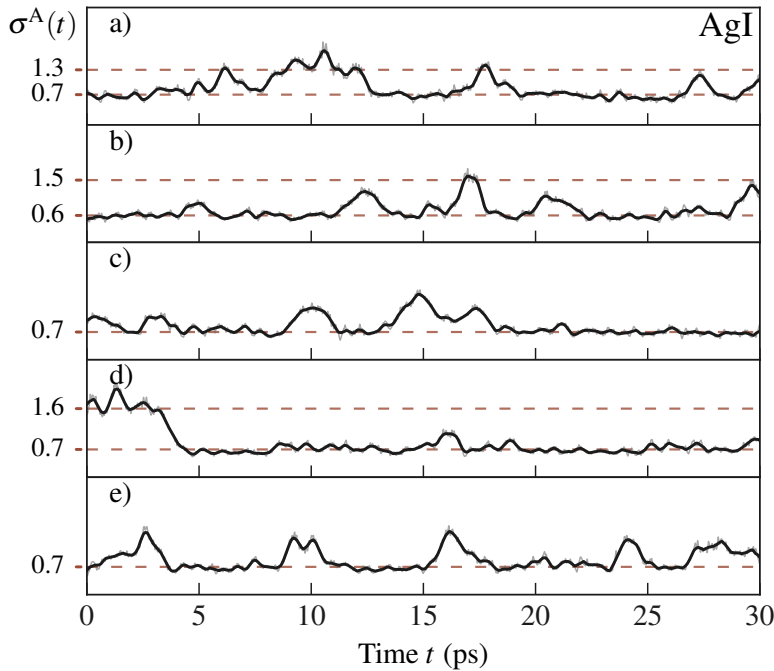


Figure 4.17: Time-resolved anharmonicity measure  $\sigma^A(t)$  for wurtzite AgI in five molecular dynamics runs of 30 ps length. Increased values of  $\sigma^A(t)$  are found in all five trajectories.

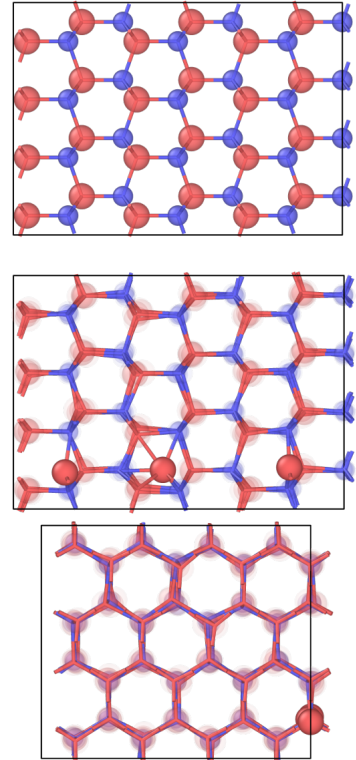


Figure 4.18: AgI viewed in (100) direction. Top: High-symmetry wurtzite structure. Middle: Silver ions (red) move into interstitial sites along (001) direction when  $\sigma^A(t) \approx 1.3$ . Bottom: The same configuration viewed along (001) direction.

The time-resolved anharmonicity measure for AgI at 300 K is shown in Fig. 4.17. As in  $\gamma$ -CuI, the value jumps back and forth between the already quite large reference value of  $\sigma^A \approx 0.7$ , short spikes at  $\sigma^A \approx 0.5$ , and longer periods where  $\sigma^A \approx 1.3 - 1.6$  for several picoseconds. For example, the first trajectory displayed in Fig. 4.17 a) jumps between  $\sigma^A \approx 0.7$  and  $\sigma^A \approx 1.3$  several times, where the longest time span around this value is about 5 ps. Averaging the positions over this time span as before, we obtain a supercell containing three Ag defects moving along (001) direction in the supercell, as shown in Fig. 4.18 (middle and bottom), as opposed to the reference wurtzite structure (top). It is again very likely that the instability of the wurtzite lattice towards defect formation at room temperature is a precursor of the actual phase transition taking place at temperatures approximately 120 K higher.

#### 4.5.4 AgCl

Silver chloride (AgCl) is yet another material of the class of transition metal halides, and the room-temperature stable phase is rock salt [135, 136, 137].

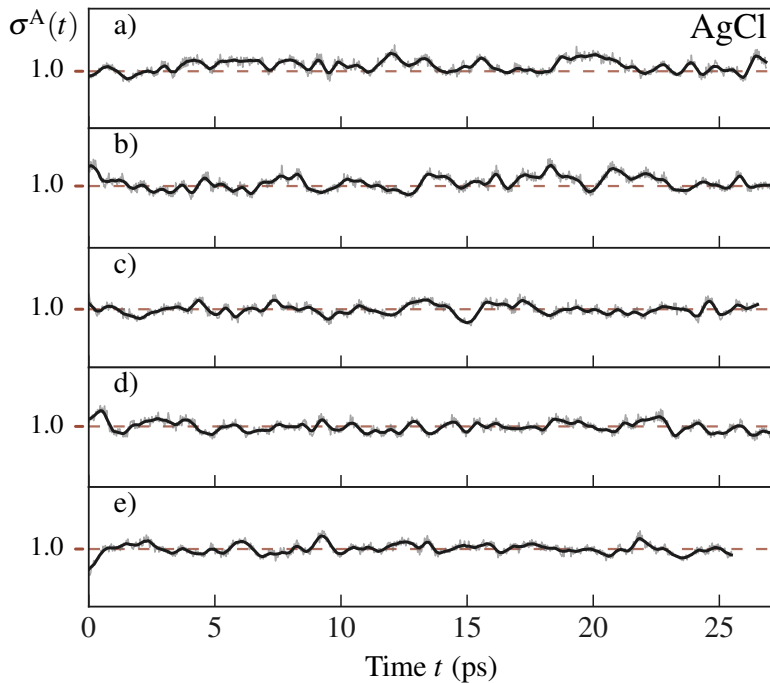


Figure 4.19: Time-resolved anharmonicity measure  $\sigma^A(t)$  for rock salt AgCl in five molecular dynamics runs of 30 ps length. No temporarily increased value of  $\sigma^A(t)$  is observed.

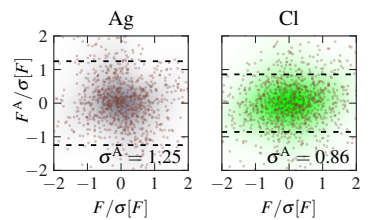


Figure 4.20: Species-resolved anharmonicity score in AgCl.

As opposed to the previously discussed transition metal halides CuI and AgI, the time-resolved anharmonicity  $\sigma^A(t)$  exhibits no “jumps” in AgCl, but rather stays constants at  $\sigma^A \approx 1$ , which can be interpreted as a situation where the 0 k harmonic model loses predictive power for the observed forces. By resolving the anharmonicity measure per atom species in Fig. 4.20 similar to the discussion for KCaF<sub>3</sub> in Sec. 4.2, we see that the harmonic model performs better for the chlorine atoms with  $\sigma_{\text{Cl}}^A = 0.86$ , and worse for silver with  $\sigma_{\text{Ag}}^A = 1.25$ . This is in line with the previous observations in metal halides where small cations proved to be more mobile and susceptible to dislocations. However, no clear-cut dislocation pattern can be identified for AgCl as opposed to CuI and AgI.

THE NATURE OF THE DYNAMICAL EFFECTS MANIFESTING IN AGCL CAN NEVERTHELESS BE ELUCIDATED. We do this by computing the pair distribution functions for the first four coordination shells in AgCl

**CITE:** pair distribution function. Boon?

, as shown in Fig. 4.21, and contrasting them with the prototypical, largely harmonic rock salt material magnesium oxide (MgO,  $\sigma^A = 0.17$ ) in Fig. 4.22.

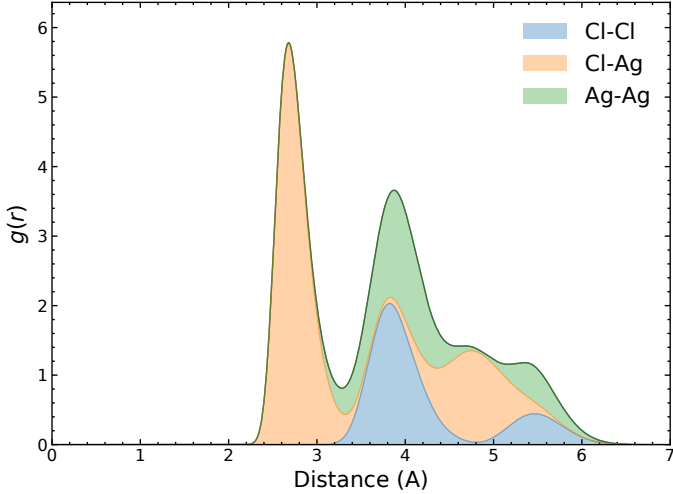


Figure 4.21: Rocksalt (SG 225) AgCl, describe comp. details Coordination shells: 1: 2.75579 atoms: Cl-Ag 2: 3.89727 atoms: Ag-Ag/Cl-Cl 3: 4.77317 atoms: Ag-Cl 4: 5.51158 atoms: Ag-Ag

In MgO, the distribution of atoms are sharply distinguishable, which means that the atoms vibrate closely around their reference position. In AgCl on the other hand, only the first coordination shell of silver-chlorine atoms is distinct at 300 K. The chlorine (Cl-Cl) and silver (Ag-Ag) sublattices (purple/green area in Fig. 4.21) show discernible peaks, although the broadening is significant compared to MgO. The silver-chlorine (Cl-Ag) distribution (yellow area) is even more broadened and is still non-zero at distances normally characteristic of like atoms (Cl-Cl or Ag-Ag), see e. g., the non-zero width of the yellow curve at 3.9 and 5.5 Å (second and fourth coordination shell). In total, this leads to a very strong broadening in the third and fourth coordination shell, with a barely discernible local maximum in the third coordination shell (4.8 Å). This is in line with experimental Extended X-ray Absorption Fine Structure (EXAFS) measurements detecting an “anomalously large motion” in the third neighbor shell already at a temperature of 120 K [137]. This hints at severe dynamical distortions throughout the simulation which are typically discussed in terms of dynamical Frenkel pair formation, where the mobile Ag<sup>+</sup> cations dynamically populate interstitial sites [138, 136, 139, 140]. While we can confirm an increased mobility of Ag<sup>+</sup> ions as discussed above, we do not observe a local accumulation of Ag<sup>+</sup> ions at interstitial sites, which should correspond to additional local minima in the respective pair distribution functions compared to the reference structure. However, such an effect might very well occur at higher temperatures, and the observed effects are fingerprints of the instability of the lattice towards this kind of dynamical defect formation. Irrespective of the exact type of defect formation, the observed dynamical effect hints at a strong form of premelting phenomenon in AgCl, which has an experimental melting temperature of 728 K.

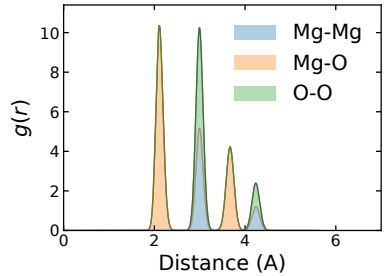


Figure 4.22: Radial distribution function resolved by pair contributions.

**SIMILAR EFFECTS CAN BE OBSERVED IN SILVER BROMIDE (AgBr).** As discussed in Ref. [136], the dynamical properties of AgCl and AgBr share many similarities with the chemically related material AgI presented in the previous section. In contrast to AgI however, they do not become superionic conductors before melting, despite the increased ion mobility presented here.

#### 4.5.5 Conclusion

In summary, we have observed a variety of non-perturbative dynamical effects occurring in the candidate materials, and discussed them for the prototypical systems  $\text{KCaF}_3$ ,  $\gamma\text{-CuI}$ ,  $\beta\text{-AgI}$ , and  $\text{AgCl}$ . The common feature of these effects is that they indicate phenomena which are known to occur in the respective materials, but at significantly higher temperatures. This comprised the onset of structural phase transitions in  $\text{KCaF}_3$ , fingerprints of a superionic phase in  $\text{CuI}$  and  $\text{AgI}$ , and pre-melting phenomena in  $\text{AgCl}$  and  $\text{AgBr}$ .



# 5

## *Ab Initio Green Kubo: Implementation*

The theoretical background for the *ab initio* simulation of thermal conductivity has been established in the previous chapters, in particular, Chp. 3. The purpose of this chapter is to discuss the practical implementation of the respective formulas for two benchmark materials. The scheme is implemented in FHI-vibes [141].

WE RESTATE THE GREEN-KUBO FORMULA for the thermal conductivity initially introduced in Sec. 3.3 as

$$\kappa^{\alpha\beta}(T) = \int d\Gamma_0 \kappa^{\alpha\beta}(\Gamma_0) f_T(\Gamma_0), \quad (5.1)$$

where  $\kappa^{\alpha\beta}(T)$  are the Cartesian components of the thermal conductivity tensor at temperature  $T$ ,<sup>1</sup> and  $\Gamma_0$  are phase-space configurations with a respective ensemble weight  $f_T(\Gamma_0)$  at the given temperature. For each phase-space configuration  $\Gamma_0$ , the thermal conductivity is computed as

$$\kappa^{\alpha\beta}(\Gamma_0) = \frac{V}{k_B T^2} \lim_{t_c \rightarrow \infty} \int_0^{t_c} dt C_{JJ}^{\alpha\beta}(\Gamma_0, t). \quad (5.2)$$

Here,  $C_{JJ}^{\alpha\beta}(\Gamma_0, t)$  denotes the heat flux autocorrelation function (HFACF),

$$C_{JJ}^{\alpha\beta}(\Gamma_0, t) = \lim_{t_0 \rightarrow \infty} \frac{1}{t_0 - t} \int_0^{t_0-t} ds J^\alpha(\Gamma_{t+s}) J^\beta(\Gamma_s), \quad (5.3)$$

which can be viewed as an average over all available starting conditions  $\Gamma_s$  during a simulation of length  $t_0$ . Each phase-space point  $\Gamma_t$  is related to the initial configuration  $\Gamma_0$  through the canonical time evolution determined by the many-body Hamiltonian of the system,  $\mathcal{H}(\Gamma)$ . Equation (5.1) through (5.3) represent an exact reformulation of the Green Kubo formula.

IN ORDER TO EVALUATE THESE EQUATIONS IN FINITE SIMULATIONS, the integrals need to be discretized and truncated to finite domains. First, we approximate Eq. (5.1) by choosing a finite set of  $M$  starting configurations  $\Gamma_0^i$ , so that

$$\kappa^{\alpha\beta}(T) \approx \frac{1}{M} \sum_{i=1}^M \kappa^{\alpha\beta}(\Gamma_0^i), \quad (5.4)$$

where the starting conditions  $\Gamma_0^i$  are chosen from NVT molecular dynamics simulations for the thermodynamic conditions of interest. For each starting

<sup>1</sup>  $T$  represents all thermodynamic conditions in the simulation, including pressure  $p$ .

condition  $\Gamma_0^i$ , we perform NVE molecular dynamics simulations to generate the time evolution of the system,  $\Gamma_t^i$ , and evaluate the heat flux,  $J^\alpha(\Gamma_t^i)$  along this trajectory. The simulation is performed for a total simulation time  $t_0$ , thereby truncating the time integral in Eq.(5.3). From the resulting autocorrelation function of finite length, the thermal conductivity is computed via Eq.(5.2), where a *cutoff time*  $t_c < t_0$  is chosen to reduce noise when the autocorrelation function has effectively decayed [142]. After computing the thermal conductivity for each trajectory, the final value is given by Eq.(5.4), i.e., by the *mean* of the individual trajectories. The statistical error due to the finite ensemble average is estimated by the *standard error*, i.e., the standard deviation of the mean,

$$\Delta\kappa^{\alpha\beta}(T) = \frac{1}{\sqrt{N}} \sqrt{\frac{1}{N} \sum_i \left( \kappa^{\alpha\beta}(T) - \kappa^{\alpha\beta}(\Gamma_0^i) \right)^2}. \quad (5.5)$$

From the Cartesian components of the thermal conductivity  $\kappa^{\alpha\beta}(t)$ , the scalar thermal conductivity  $\kappa(T)$  is obtained via

$$\kappa(T) = \frac{1}{3} \sum_\alpha \kappa^{\alpha\alpha}(T). \quad (5.6)$$

**IN EMPIRICAL FORCE FIELD APPROACHES**, the appearing equations can be evaluated as is, and convergence in size and time can be checked in a brute-force way by increasing the respective scales well beyond the necessary limits. From an *ab initio* perspective, the accessible size and time scales are each at least two orders of magnitude lower,<sup>2</sup> and additional steps are necessary to increase the amount of information that can be extracted from the comparatively short simulations. The purpose of this chapter is to discuss these additional steps in detail: First, we present steps to remove noise from the heat flux autocorrelation functions  $C_{JJ}(t)$ , which enables to choose cutoff times  $t_c$  in a numerically robust way. Next, we discuss the size extrapolation scheme in terms of the harmonic mapping presented in Sec.3.5 which allows to correct for the finite size of simulations cells used in *ab initio* molecular dynamics simulations. Finally, we discuss the necessary simulation times  $t_0$  and how those can be estimated for novel materials.

**WE PRESENT THE IMPLEMENTATION IN DETAIL** for the case of periclase magnesium oxide (MgO) which is well-known in the literature, and, as a rather harmonic material, a typical benchmark system for perturbative heat transport techniques. We then apply the same approach to the strongly anharmonic marshite copper iodide (CuI), for which basic assumptions of perturbation theory are violated, as we will explain in detail. Both structures are studied at GGA level of theory using the PBEsol functional and light-default basissets in FHI-aims [143, 98]. Supercell sizes are 216 atoms each, and the MD simulations are performed via FHI-vibes [144, 141]. The aiGK methods as described is implemented in FHI-vibes as well. Force constants for the size extrapolation via harmonic mapping are obtained via regression from the MD runs via the temperature dependent effective potentials code (TDEP) [145]. The MD runs are thermalized using the pre-thermalization technique outlined in Sec.2.4.1 using finite-differences force constants obtained via phonopy [146]. Afterwards, a Langevin thermostat at the target

<sup>2</sup> Force fields: 1 ns for 10000 atoms within 1 day on one supercomputer node, *ab initio*: 50 ps for 200 atoms within 1 months on five supercomputer nodes.

temperature (300 K) is used to perform NVT sampling. After an initial sampling period of 2.5 ps, the thermal pressure is relaxed according to the scheme outlined in Sec. E.2 in the appendix to account for thermal expansion. Starting points  $\Gamma_0^i$  for the NVE simulations are chosen from an NVT run for the relaxed supercell at least 2 ps apart. The time step for the MD simulation was chosen as 5 fs, which corresponds to a tenth of the shortest period duration of the harmonic spectrum of MgO ( $\omega_{\max} \approx 20$  THz).

## 5.1 Noise Reduction Scheme and Cutoff Estimation

### 5.1.1 Discard non-contributing terms

The raw *ab initio* heat flux used in this work was defined in Eq. (3.66) and is given for a phase-space point  $\Gamma_t = \{ \mathbf{R}(t), \dot{\mathbf{R}}(t) \}$  by

$$\mathbf{J}^{\text{raw}}(t) = \frac{1}{V} \sum_I \sigma_I(t) \dot{\mathbf{R}}_I(t), \quad (5.7)$$

where  $\sigma_I(t) \equiv \sigma_I[\mathbf{R}(t)]$  are atomic virial tensors for the configuration at the given time  $t$  as defined in Eq. (3.64), and  $\dot{\mathbf{R}}_I(t)$  is the velocity of atom  $I$  as usual. We split the raw flux in two parts,

$$\mathbf{J}^{\text{raw}}(t) = \frac{1}{V} \sum_I \delta\sigma_I(t) \dot{\mathbf{R}}_I(t) + \frac{1}{V} \sum_I \langle \sigma_I \rangle \dot{\mathbf{R}}_I(t), \quad (5.8)$$

where  $\langle \sigma_I \rangle$  is the average atomic virial, and  $\delta\sigma_I(t)$  is the time-dependent part. In the absence of diffusion, the second term is the total time derivative of a bounded vector field,  $\sum_I \langle \sigma_I \rangle \dot{\mathbf{R}}_I(t) = \frac{d}{dt} \sum_I \langle \sigma_I \rangle \mathbf{R}_I(t)$ . By means of the gauge invariance principle introduced in Sec. 3.2.1, it therefore does not contribute to the time integral in Eq. (5.2), and can be discarded before evaluating the heat flux autocorrelation function [90]. We therefore always use the following heat flux expression:

$$\mathbf{J}(t) = \frac{1}{V} \sum_I \delta\sigma_I(t) \dot{\mathbf{R}}_I(t). \quad (5.9)$$

Depending on the material, discarding the non-contributing part from the raw heat flux reduces the noise in the simulation *massively*, as shown for the case of MgO in the upper panel of Fig. 5.1 (orange curves compared to light blue curves).

Due to the finite time of the simulation, we furthermore enforce a vanishing expectation of the flux to remove bias from the resulting quantities by removing the finite-time average,  $\mathbf{J}(t) \rightarrow \delta\mathbf{J}(t) = \mathbf{J}(t) - \langle \mathbf{J} \rangle_t$ .

### 5.1.2 Noise filtering

After discarding the gauge-invariant contributions from the heat flux, there is still a considerable level of noise in the HFACF, which hinders a robust identification of the time at which it is fully decayed, i.e., the cutoff time  $t_c$ . Available techniques to identify cutoff times, such as the first avalanche method introduced in Ref. [147], are not fully parameter-free, and need hand tuning, even if very little.<sup>3</sup> We therefore suggest an approach that does rely only on a single parameter which is chosen based on the vibrational spectrum

<sup>3</sup> The first avalanche technique determines cutoff times by means of a signal-over-noise ratio and relies on two parameters, a window size for computing moving averages, and a threshold value for the resulting avalanche function.

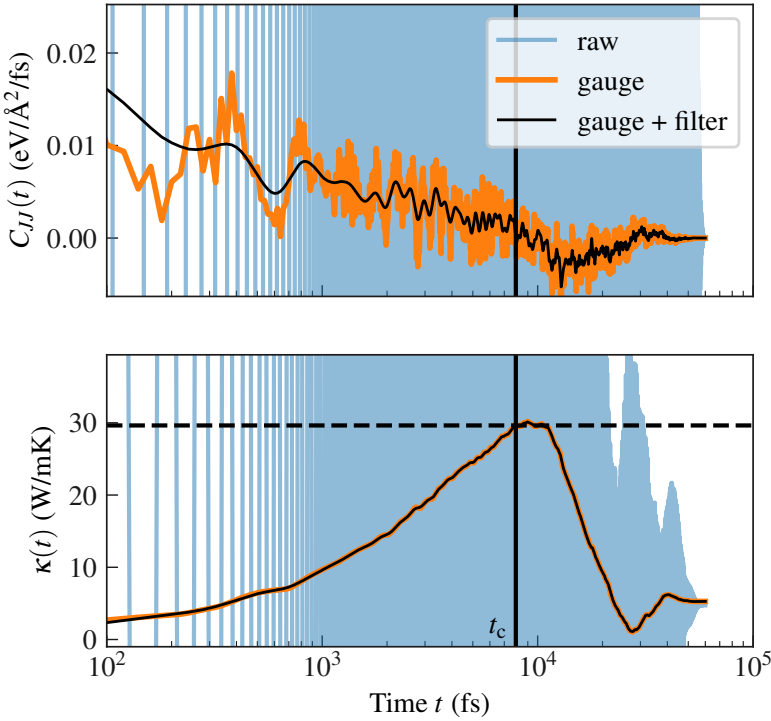


Figure 5.1: Heat flux autocorrelation function  $C_{JJ}(t)$  (HFCAF) as defined in Eq. (5.3) and its cumulative integral, i. e., the thermal conductivity  $\kappa(t)$  as function of lag time  $t$ . Light blue:  $C_{JJ}(t)$  and  $\kappa(t)$  obtained by using the raw flux as defined in Eq. (5.7). Orange: After discarding the gauge-invariant term in Eq. (5.8). Black curves: After applying additional, integral-preserving noise filtering as explained in the main text. The cutoff time  $t_c$  is chosen based on the “first dip” of the noise-filtered HFCAF. *Computational details:* The shown data is for the  $\kappa^{yy}$ -component of MgO in an aiMD simulation of 60 ps total length using a time step of 5 fs. The heat flux was evaluated every four steps. The system was thermalized to 300 K using a Langevin thermostat. The system size is 216 atoms in a cubic supercell.

of the material: Motivated by the fact that the *integrated* HFCAF, i. e., the cumulative thermal conductivity

$$\kappa(t) = \frac{V}{k_B T^2} \int_0^t dt' C_{JJ}(t') , \quad (5.10)$$

is already a much smoother function than the HFCAF itself, we apply a shape-preserving Savitzky-Golay filter to  $\kappa(t)$  as implemented in Scipy [148, 149]. The remaining parameter is the window size for the filter. It is chosen based on the vibrational spectrum of the material by taking the period length corresponding to the slowest significant frequency  $\omega_{\min}$ . Thereby, all noise of higher frequency is effectively filtered from  $\kappa(t)$ , while all relevant time integrals are preserved by construction: The cumulative kappa before (orange curve) and after (black curve) lie right on top of each other in the lower panel of Fig. 5.1. The filter is constructed such that the antisymmetry of  $\kappa(t)$  in time,  $\kappa(-t) = -\kappa(t)$  is respected.<sup>4</sup> This also ensures that  $\kappa(t)$  vanishes identically at  $t = 0$ .

Based on the filtered cumulative thermal conductivity, the HFCAF can be obtained by differentiating, which carries over the filtering to  $C_{JJ}(t)$ . The filtered HFCAF can be obtained analytically by fitting spline functions to  $\kappa(t)$ , or numerically by applying the same filter on the numerical gradient of  $\kappa(t)$ . The resulting cumulative thermal conductivity  $\kappa(t)$  and HFCAF  $C_{JJ}(t)$  are shown as black curves in Fig. 5.1. From the noise-filtered HFCAF, the cutoff time  $t_c$  is chosen by a “first dip” criterion, i. e., when  $C_{JJ}(t)$  drops to zero [147]. This corresponds to the first significant plateau in  $\kappa(t)$  after removing the noise. With the cutoff time  $t_c$ , the resulting thermal conductivity for a given component of the thermal conductivity tensor is given by the value  $\kappa = \kappa(t_c)$  as indicated by the dashed horizontal line in Fig. 5.1. The presented

<sup>4</sup> The antisymmetry of  $\kappa(t)$  is a consequence of the time symmetry of  $C_{JJ}(t)$ .

scheme will be used for all reported values of thermal conductivity in the following.

## 5.2 Size extrapolation

After we have seen how the Green-Kubo formula is used to compute thermal conductivities from the *ab initio* heat flux evaluated along aiMD trajectories, we shortly review the size extrapolation scheme first introduced in Ref. [15] and discussed in more detail in Sec. 3.5. The aim of the size extrapolation is to correct for finite size effects occurring in aiMD simulations, because the supercells used in *ab initio* simulations are limited in size, and phonon modes of longer wavelength than the supercell are therefore not included.

As discussed in Sec. 3.5, the correction works by computing the harmonic contribution to the thermal conductivity  $\kappa_{\text{ha}}$  within the supercell via Eq. (3.88)

$$\kappa_{\text{ha}}^{\alpha\beta} = V k_B \sum_{b,\mathbf{q}} v_b^\alpha(\mathbf{q}) v_b^\beta(\mathbf{q}) \tau_b(\mathbf{q}), \quad (5.11)$$

where  $v_b^\alpha(\mathbf{q})$  is the group velocity of a phonon mode with band index  $b$  and *commensurate* wave vector  $\mathbf{q}$ , and  $\tau_b(\mathbf{q})$  is the lifetime obtained from the autocorrelation function of the mode-resolved energy  $E_b(\mathbf{q}, t)$  as defined and discussed in Eq. (3.91) [15]. For a given simulation  $\{\Gamma_t^i\}$ , Eq. (5.11) is evaluated for all commensurate  $\mathbf{q}$ -points, and projected to the symmetry-inequivalent points in the Brillouin zone determined by the space group operations of the system to improve the statistics [44]. The irreducible  $\mathbf{q}$ -points in the Brillouin zone are obtained by iteratively reducing the given grid with the available symmetry operations for the system obtained by the spglib package [150].

IN THE NEXT STEP, the lifetimes  $\tau_b(\mathbf{q})$  are interpolated to denser  $\mathbf{q}$ -point meshes by  $\tilde{\tau}_b(\tilde{\mathbf{q}}) = \lambda_b(\tilde{\mathbf{q}}) \omega_b^{-2}(\tilde{\mathbf{q}})$  with a weakly  $\mathbf{q}$ -dependent function  $\lambda_b(\tilde{\mathbf{q}})$  obtained by linearly interpolating the lifetimes obtained at commensurate  $\mathbf{q}$ -points. The scaling of lifetimes with  $\omega_b^{-2}(\mathbf{q})$  is rooted in basic phonon theory as discussed in detail by Herring [112]. For the acoustic modes at  $\mathbf{q} = \Gamma = 0$ , where  $\omega(\mathbf{q} \rightarrow \mathbf{0}) \rightarrow 0$ , the value for  $\lambda_b(\Gamma)$  is obtained by averaging over values at the surrounding  $\mathbf{q}$ -points. For the new, denser grid, an interpolated value,

$$\kappa_{\text{ha-int}}^{\alpha\beta}(N_{\tilde{\mathbf{q}}}) = V k_B \frac{N_{\mathbf{q}}}{N_{\tilde{\mathbf{q}}}} \sum_{b,\tilde{\mathbf{q}}} v_b^\alpha(\tilde{\mathbf{q}}) v_b^\beta(\tilde{\mathbf{q}}) \tilde{\tau}_b(\tilde{\mathbf{q}}), \quad (5.12)$$

can be obtained, where  $N_{\tilde{\mathbf{q}}}$  is the number of points in the new grid, and the factor  $N_{\mathbf{q}}/N_{\tilde{\mathbf{q}}}$  accounts for the increased number points. The bulk limit of Eq. (5.12) is obtained by computing interpolated values for an increasing density of  $\mathbf{q}$ -points. Since Eq. (5.12) is a Riemann sum approximating the Brillouin zone integral  $\int d^3 q$ , its convergence can be expected to be linear in  $N_{\tilde{\mathbf{q}}}^{-1/3} \equiv 1/n_q$ , where  $n_q$  is number of  $\mathbf{q}$ -points per Cartesian direction. The slope of this curve can be used to extrapolate the value of  $\kappa_{\text{ha}}$  to bulk limit, as shown in Fig. 5.2. With the extrapolated value  $\kappa_{\text{ha-bulk}}$ , a correction can be

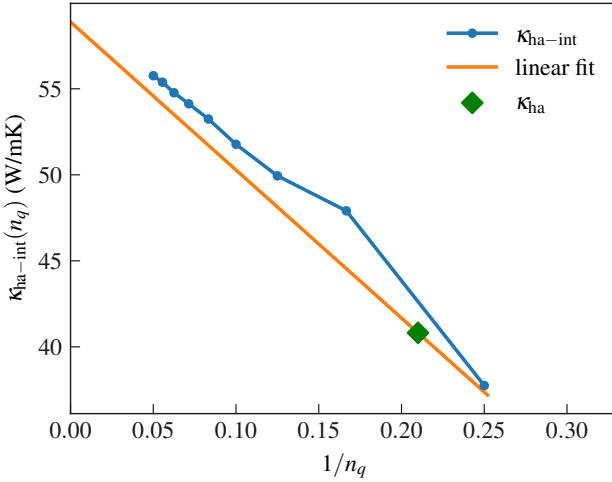


Figure 5.2: Size extrapolation correction to bulk limit computed from Eq. (5.12) assuming linear convergence in  $1/n_q$ , where  $n_q$  is the number of  $\mathbf{q}$ -points per Cartesian direction.

obtained via

$$\delta\kappa_{\text{ha-correction}} = \kappa_{\text{ha-bulk}} - \kappa_{\text{ha}}, \quad (5.13)$$

from which the final result for the thermal conductivity is obtained via

$$\kappa_{\text{corrected}}^{\alpha\beta} = \kappa^{\alpha\beta} + \delta\kappa_{\text{ha-correction}}^{\alpha\beta}, \quad (5.14)$$

where  $\kappa^{\alpha\beta}$  is the value from the *ab initio* Green Kubo simulation. The interpolation scheme effectively subtracts harmonic contributions to the thermal conductivity from vibrations commensurate with the supercell, and extrapolates them to the bulk limit, thereby including long-range contributions otherwise not present in the simulation cell.

### 5.3 Simulation Time Convergence

After we have seen how the cutoff time  $t_c$  in Eq. (5.2) can be obtained, and finite-size errors can be corrected, we discuss the convergence of presented scheme as a function of the simulation time  $t_0$  in Eq. (5.3). We do this for the case of MgO for three independent trajectories of 60 ps length each. We truncate every trajectory in 10 % steps down to a length of 6 ps, and apply the workflow presented in the previous sections to each of the truncated trajectories. The convergence of the scalar thermal conductivity is shown in Fig. 5.3 as function of a dimensionless *effective simulation time*  $t_0^{\text{eff}}$ , which we define via

$$t_0^{\text{eff}} = t_0 \cdot \bar{\omega}_{\min}, \quad (5.15)$$

where  $t_0$  is the (truncated) simulation time, and  $\bar{\omega}_{\min}$  is a characteristic frequency for the slow degrees of freedom of the system, chosen as the mean frequency of the lowest 20 % of the vibrational spectrum as explained in Fig. 5.4. In MgO, this frequency is 7.5 THz.

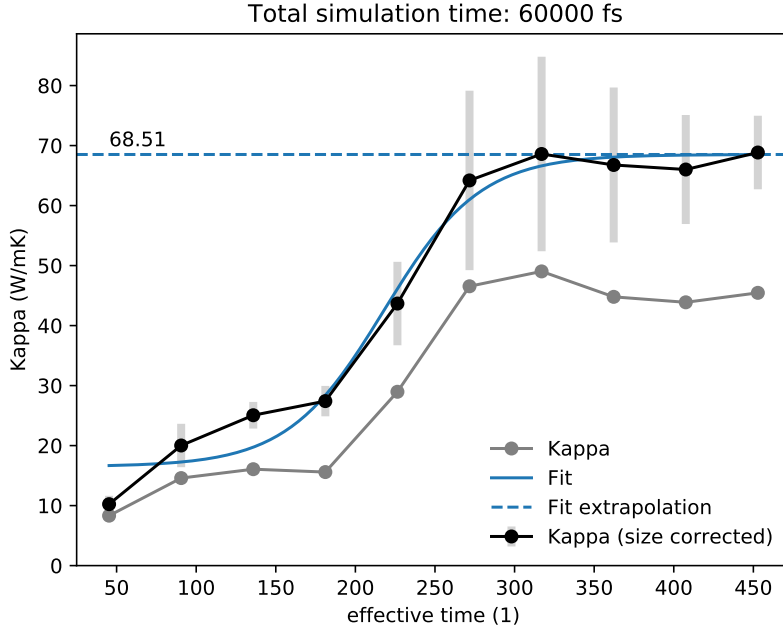


Figure 5.3: Thermal conductivity  $\kappa$  as function of the effective simulation time  $t_0^{\text{eff}} = 7.5 \text{ THz} \cdot t_0$  as defined in Eq. 5.15. Values are given as the ensemble average over three independent trajectories. The error bars are computed according to Eq. (5.5) as the standard error of the ensemble average. The blue curve is a logistic curve defined in Eq. (5.16) fitted to the  $\kappa$  values, the dashed blue curve is the infinite time limit of the fitted function. Gray dots represent the thermal conductivity as given by the simulation without the size-correction scheme.

Please note that the values for  $\kappa$  shown here cannot be directly compared to the value displayed in Fig. 5.1 or 5.2, because the latter only show single components of single runs, which can vary substantially from the total average.

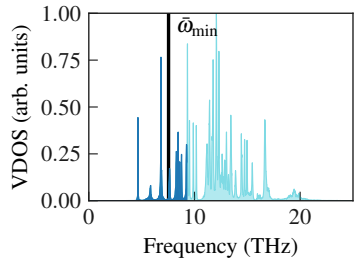


Figure 5.3 shows that the thermal conductivity converges after an effective simulation time of  $t_0^{\text{eff}} \approx 300$ , which corresponds to a time of 40 ps, where the value of  $\kappa$  reaches a plateau within the error bars. The overall shape of the curve can be described as follows: Simulations shorter than 20 ps ( $t_0^{\text{eff}} \lesssim 150$ ) sample the early decay of the HFACF which contribute about 30 W/mK to the total thermal conductivity. After a simulation time of 25 ps ( $t_0^{\text{eff}} \gtrsim 190$ ), the late decay of the HFACF is sampled, contributing more than double the amount to the total thermal conductivity of  $68.8 \pm 6.1$  W/mK after the total simulation time. In the plot, this two-step behavior is approximated by a logistic function

$$f(t) = \frac{L}{1 + \exp\left(-\frac{(t-t_{\text{inflection}})}{\tau}\right)} + f_0 , \quad (5.16)$$

which allows to accurately quantify the simulation times where the second super-linear increase in  $\kappa$  occurs, i. e., the region in the vicinity of the inflection point located at  $t_{\text{inflection}} = 218$ , which corresponds to a simulation time of 29 ps.

#### 5.4 Comparison to Literature Values

Periclase MgO is an important constituent of the earth mantle and its thermal properties have been studied in detail both experimentally and theoretically [151, 152, 153, 154, 155, 96, 156, 157]. We list the common experimental reference values for the thermal conductivity of periclase MgO in Tab. 5.1. The aiGK value presented in this work agrees within the statistical precision with the experimental value presented by MacPherson and Schloessin [154]. It slightly overestimates the values reported by Slack [152] and Touloukian et al. [153]. More recent experiments by Dalton et al. and Hofmeister using

Reference	Thermal conductivity at 300 K (W/mK)
Slack 1962 [152]	59.7
Touloukian et al. 1970 [153]	59.8
MacPherson and Schloessin 1983 [154]	$61.7 \pm 10.5$
Andersson and Bäckström 1986 [158]	$55.2 \pm 0.4$
Dalton et al. 2013 [159]	$53 \pm 2$
Hofmeister 2014 [160]	50.1
This work	$68.8 \pm 6.1$

Table 5.1: Experimental values for the thermal conductivity of periclase MgO at ambient conditions.

laser-flash experiments report lower values of thermal conductivity in the range of 50–55 W/mK [159, 160].

Overall, we overestimate the experimentally observed thermal conductivity by about 10–30 %, depending on the reference. This can be explained by two factors: First, the simulation deals with isotopically pure MgO. Neglecting isotope scattering is known to increase the thermal conductivity noticeably in MgO [152, 156], and the experiments measure samples of varying isotope and defect content. Second, the aiGK theory uses classical statistical mechanics, and nuclear quantum effects lowering the heat capacity of MgO and therefore its thermal conductivity are neglected. These effects have been shown to lower the thermal conductivity in MgO by about 5 % at 500 K [113], a stronger effect can therefore be expected at 300 K. We also compare to theoretical

Reference	Thermal conductivity at 300 K (W/mK)
Tang and Dong 2010 [156]	$\approx 66$
Dekura and Tsuchiya 2017 [157]	$\approx 54$
Plata et al. 2017 [161]	54.06
Xia et al. 2020 [110]	50.1 – 58.7
This work	$68.8 \pm 6.1$

Table 5.2: Theoretical values for the thermal conductivity of periclase MgO at ambient conditions. All cited approaches use a perturbative Boltzmann transport approach with three phonon scattering. Xia and coworkers use three different flavors of Boltzmann transport theory and therefore give three values for thermal conductivity in the indicated range.

values listed in Tab. 5.2. Our study agrees with the value reported by Tang and Dong [156], whereas the other available references are overall smaller by about 10–15 W/mK, which is above the statistical precision. Again, the difference can most probably be attributed to isotope scattering and nuclear quantum effects.

IN SUMMARY, THE AGREEMENT WITH LITERATURE VALUES CAN BE CONSIDERED SATISFACTORY, given the wide spread of experimental values in the range of 50–62 W/mK for non-defect-free MgO samples, and noticing that MgO is not fully classical at 300 K. Furthermore, please note that MgO is largely harmonic with  $\sigma^A = 0.17$  and therefore not an ideally suited candidate material for Green-Kubo studies, as all requirements for perturbative Boltzmann transport are fulfilled, and good quantitative agreement can be achieved with that approach, cf. Tab. 5.2.

## 5.5 Case Study Copper Iodide

After discussing our implementation of the aiGK method and found reasonable agreement with literature values for periclase MgO, we apply the presented methodology to zincblende copper iodide ( $\gamma$ -CuI), also known as marshite. CuI is a transparent semiconductor which shows several interesting electronic and thermal transport properties: In particular, its room temperature thermal conductivity is very low with only 1.68 W/mK [162], which is typical for copper halide materials [163]. In polycrystalline thin films, even lower thermal conductivities of 0.48–0.55 W/mK have been reported [164, 165].

In our initial screening for anharmonic materials, CuI was detected as particularly anharmonic, with a one-shot  $\sigma_{\text{OS}}^{\text{A}} = 0.37$ , and a value of  $\sigma^{\text{A}} = 0.4 - 0.5$  in molecular dynamics simulations. The peculiar dynamical effects occurring in CuI, i.e., formation of metastable Cu defects below the superionic phase transition, have been discussed in Sec. 4.5.2 in the previous chapter. CuI can therefore be considered a bigger challenge for dynamical simulations compared to MgO.

### 5.5.1 Thermal conductivity

Following the same recipe presented earlier in this chapter, the convergence of the aiGK thermal conductivity with effective simulation time is shown in Fig. 5.5 for CuI at room temperature. The final value of  $1.38 \pm 0.14$  W/mK is

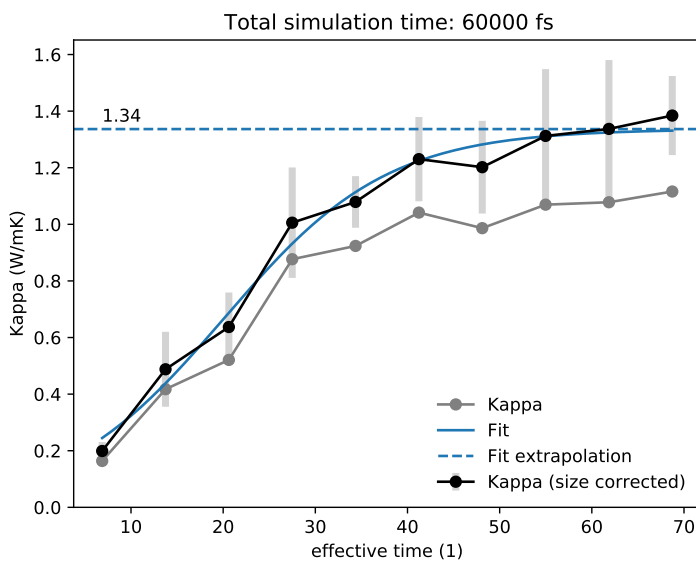


Figure 5.5: Thermal conductivity  $\kappa$  as function of the effective simulation time  $t_0^{\text{eff}} = 1.1 \text{ THz} \cdot t_0$  as defined in Eq. 5.15. Values are given as the ensemble average over three independent trajectories. The error bars are computed according to Eq. (5.5) as the standard error of the ensemble average. The blue curve is a logistic curve defined in Eq. (5.16) fitted to the  $\kappa$  values, the dashed blue curve is the infinite time limit of the fitted function. Gray dots represent the thermal conductivity as given by the simulation without the size-correction scheme.

approached within error bars after an effective simulation time of  $t_0^{\text{eff}} = 40$ , which corresponds to  $t_0 = 36$  ps. The finite size correction contributes about 0.26 W/mK to the thermal conductivity, i.e., 19 % of the total value.

Comparing this to the available literature in Tab. 5.3, we find good agreement with the experimental reference value of 1.68 W/mK, while the value is clearly above the thin-film limit of 0.55 W/mK. The theoretical reference on

Reference	Thermal conductivity at 300 K (W/mK)
CRC Handbook [162] (experiment)	1.68
Yang et al. [164] (experiment)	0.55 <sup>†</sup>
Togo et al. [166] (theory)	6.55–7.22
This work	1.38 ± 0.14

Table 5.3: Experimental values and one theoretical reference for the thermal conductivity of marshite CuI at ambient conditions. The value from Yang et al. marked by <sup>†</sup> is from a thin film experiment, and therefore can be regarded as a lower bound of the bulk thermal conductivity [164].

the other hand drastically overestimates the thermal conductivity by a factor of  $\approx 4$  [166]. Since the theoretical reference uses a perturbative approach in terms of third-order force constants obtained at the local minimum of the potential-energy surface, a probable explanation for this strong discrepancy is the inability of this approach to model the actual, strongly anharmonic dynamics of CuI with sufficient accuracy. As discussed in Sec. 4.5.2, CuI inhibits effects like metastable defects, which are qualitatively different from the phonon picture of atoms moving about a well defined reference position in a nearly harmonic potential. These effects are, however, naturally included in the non-perturbative aiGK formalism.

## 5.6 Conclusion

We have introduced the technical details of our aiGK implementation, and discussed two benchmark systems at ambient conditions: Periclase MgO, and marshite CuI. Although both structures are very simple cubic structures with two atoms in the unit cell, they behave quite differently from a dynamical point of view: MgO is a largely harmonic system which can be regarded as a textbook example for phonon theory, where all basic assumptions hold. In particular there are well defined reference positions, and the deviation from perfectly harmonic interactions is quite weak, with a  $\sigma^A = 0.17$  signaling an anharmonic contribution to the forces of about 17 %. CuI on the other hand is strongly anharmonic, with  $\sigma^A \approx 0.4 – 0.5$ , and displays spontaneous formation of metastable insterstitial defects as discussed in Sec. 4.5.2. While perturbative approaches proved to be very accurate for MgO, and even had some advantages compared to aiGK in situations where the material of interest is not fully classical, or isotope scattering lowers the thermal conductivity substantially, the differences were much bigger for the strongly anharmonic CuI, where the perturbative approach overestimated the thermal conductivity drastically, whereas the aiGK is in good agreement.

THE AI GK METHOD IS THEREFORE OUR METHOD OF CHOICE for the investigation of the strongly anharmonic candidate thermal insulators suggested in Chp. 4 with potentially low thermal conductivity.

# 6

## *Thermal Conductivities for Strongly Anharmonic Compounds*

After introducing the implementation of the *ab initio* Green Kubo (aiGK) method in the previous chapter, we are now in position to present results for the set of potential thermal insulators identified in chapter 4.

We first discuss the question of simulation time convergence for an initial set of materials in order to predict systems which can be computed with a simulation time of 30-60 ps. This time was chosen as a compromise between the finite amount of available computational resources and the desire to compute as many materials from the list of candidates as possible. In a second step, we compare the computed thermal conductivities at room temperature to experimental references for the subset of materials for which experiments are available to further verify the aiGK method beyond the two materials presented in the previous chapter. In the last step, we present the computed thermal conductivities for the remaining materials, i. e., those for which no experimental thermal conductivity was reported before, and discuss how they fit into the schema of predicting thermal insulators from anharmonicity estimates as discussed in Sec. 4.3. We eventually highlight the particularly interesting class of chalcopyrite compounds and try to answer some open questions from experimental and semi-empirical theoretical literature.

### *6.1 Convergence estimation*

We discuss simulation time convergence in the light of the *effective simulation time* introduced in Sec. 5.3. The key idea is to identify lower boundaries for the *necessary* effective simulation time in a material in order to assess whether a time-converged thermal conductivity is possible to obtain within a simulation time of 30-60 ps. For choosing these boundaries, we leverage the observed convergence behavior of seven materials, i. e., MgO, NaF, KMgF<sub>3</sub>, NaCl, NaBr, CuI, and NaI, each of them computed with 60 ps simulation time. We thereby define four thresholds of minimal effective simulation time based on a material's anharmonicity  $\sigma^A$ , reflecting that phonons in harmonic materials like MgO have longer lifetimes than those in anharmonic materials. The criteria are displayed in Fig. 6.1. In particular, we define the thresholds  $t_0^{\text{eff}} > 240$  for harmonic materials with  $\sigma^A \leq 0.2$ ,  $t_0^{\text{eff}} > 120$  for materials with  $0.2 < \sigma^A \leq 0.3$ ,  $t_0^{\text{eff}} > 60$  for materials with  $0.3 < \sigma^A \leq 0.4$ , and  $t_0^{\text{eff}} > 45$  for materials with  $\sigma^A > 0.4$ .

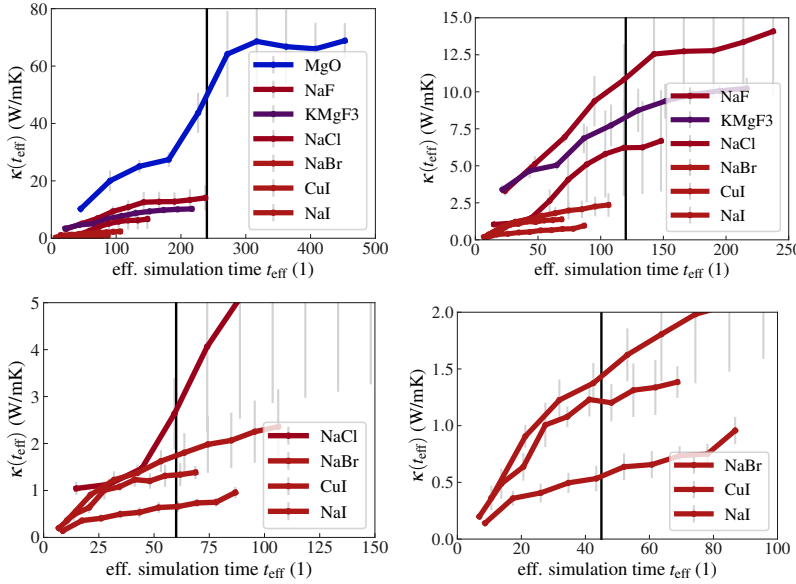


Figure 6.1: Illustration of minimal necessary effective simulation times. Upper left:  $t_0^{\text{eff}} = 240$  for harmonic materials with  $\sigma^A \leq 0.2$ . Upper right:  $t_0^{\text{eff}} = 120$  for materials with  $0.2 < \sigma^A \leq 0.3$ . Lower left:  $t_0^{\text{eff}} = 60$  for materials with  $0.3 < \sigma^A \leq 0.4$ . Lower right:  $t_0^{\text{eff}} = 45$  for materials with  $\sigma^A > 0.4$ .

We point out that at this stage, the given thresholds are meant as a *necessary* condition for convergence, which ensures that a significant contribution to the cumulative thermal conductivity is included in the simulation. A statement about the *sufficient* simulation time, however, can only be made on the level of individual trajectories by means of longer simulation times. This verification should therefore be reserved for materials that show interesting properties after the *necessary* simulation time.

Based on this estimation, we identify 57 materials out of the list of 112 candidates to compute thermal conductivity on, and discuss those in the following: First we compare thermal conductivities for 24 of these 57 materials to the experimental literature in order to benchmark the aiGK method, afterwards we present and discuss our findings for the remaining 33 materials without experimental reference.

**TODO:** list of materials in appendix

## 6.2 Comparison to Experiment

In order to assess the validity of the aiGK method for the computation of thermal conductivity in anharmonic compounds, we compare results for 21 materials to the experimental literature. A detailed list including all considered experimental references is given in Tab. I.1 in appendix I. The difficulties when comparing to experimental references have been discussed in detail for periclase MgO in Sec. 5.4. In principle, these carry over to all other compounds, however, for most materials, the body of literature is much smaller compared to MgO. The list of experiments also includes measurements on polycrystalline samples. While thermal conductivity should be reduced in polycrystalline samples compared to single crystals because of boundary scattering, experimental studies have shown that the effect is minor in sufficiently dense polycrystalline samples, especially in low thermal conductivity materials which are less sensitive to boundary scattering due to their intrinsically low phonon mean free paths [151]. In the course of our literature

review we have generally found differences of 0–20 % between measurements on single- and polycrystalline samples, which supports this finding. Nevertheless, additional care must be taken when evaluating literature on polycrystalline samples: Experiments aiming at measuring other properties besides thermal conductivity, in particular the thermoelectric figure of merit  $zT$ , typically do not attempt to reproduce the bulk thermal conductivity, and use less dense samples, which is beneficial for reducing thermal conductivity and thereby increasing the figure of merit. The resulting thermal conductivity will then be influenced severely by the details of the sample processing, and a comparison to bulk thermal conductivity is not meaningful. However, some experiments specifically aim at reproducing polycrystalline samples of near-bulk density in order to assess the bulk thermal conductivity of a material. Only experiments on polycrystalline samples of this type are considered in this work.

A comparison of thermal conductivities computed via the aiGK method as introduced in the previous chapter and the experimental literature is shown in Fig. 6.2. Overall, we find very good agreement in the 24 considered

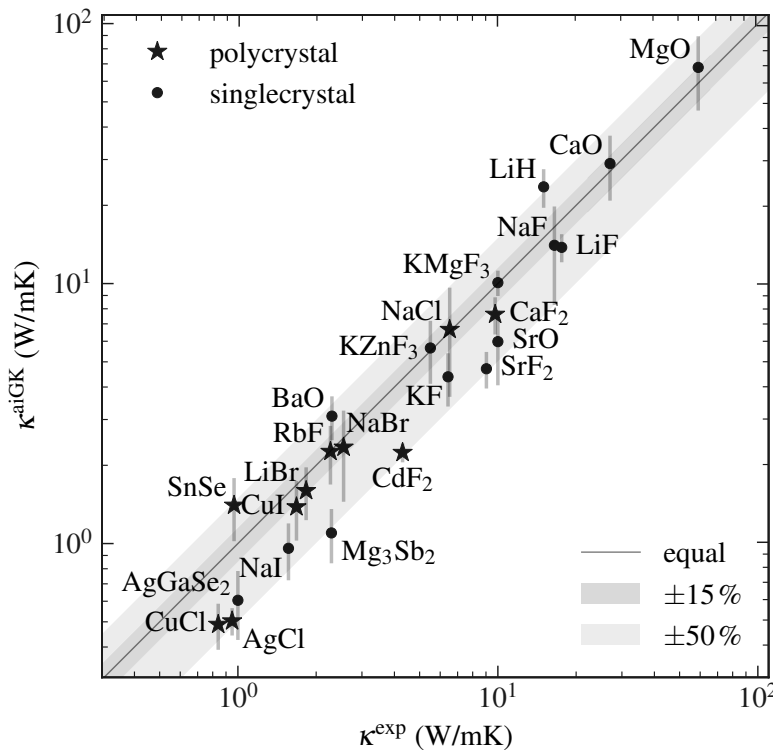


Figure 6.2: Comparison to experiment. Bullets (●): Single crystal. Stars (★): Contains data from polycrystalline experiment. Error bar in y-direction: Statistical uncertainty for  $\kappa^{\text{aiGK}}$  from standard error over individual trajectories. Diagonal line: Agreement with experiment or mean of experiments if multiple available. Dark grey region: Agreement between mean experiment and mean computation with  $\pm 15\%$  deviation. Light grey region: Agreement between mean experiment and mean computation with  $\pm 50\%$  deviation.

materials, with 10 out of 24 being within experimental accuracy of  $\pm 15\%$ , and all other within an extended accuracy which we choose as  $\pm 50\%$  within the average experimental reference, reflecting the high degree of variation in experimental values for materials where a significant amount of references is available, see especially the discussion in Ref. [10].

The strongest deviation from experiment is seen for LiH, which is computed as  $\kappa^{\text{aiGK}} = 23.6 \pm 4.0 \text{ W/mK}$ , where the available experimental value is  $\kappa^{\text{exp}} = 14.7 \text{ W/mK}$  [167]. However, both lithium and especially hydrogen

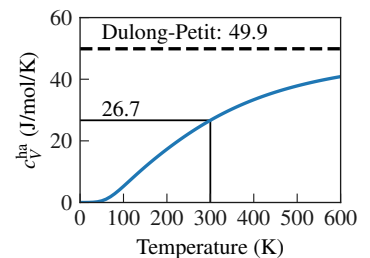


Figure 6.3: Harmonic heat capacity per formula unit  $c_V^{\text{ha}}$  for LiH compared to the classical Dulong-Petit value.

are light elements, so that LiH is not fully classical at room temperature, as can be estimated by comparing the harmonic heat capacity of LiH at 300 K to the classical Dulong-Petit value in Fig. 6.3 [68]. The harmonic heat capacity for LiH is only at about 50 % of the classically expected value of  $6R = 49.9 \text{ J/mol/K}$  for solids with two atoms in the unitcell. This value can only be taken as an upper boundary to the deviation in thermal transport properties expected from the lack of nuclear quantum effects, since low-frequency phonon modes already behave more classical at the given temperature [168, 169]. A significant overestimation by the classical Green Kubo method can nevertheless be expected in this material. Interestingly, the aiGK value agrees very well with another computational study by Lindsay, who found a value of  $\kappa = 23.00 \text{ W/mK}$  using third-order Boltzmann transport [170].<sup>1</sup> In that approach, the quantum nature of nuclei should be better captured than in the aiGK method, and Lindsay ascribes the deviation from experiment to higher-order phonon-phonon interactions neglected in their approach. This discussion is in line with the more phenomenological discussion proposed by Slack in Ref. [167], where he points out the strong anharmonicity in LiH that manifests in the change of phonon frequencies as measured by the Grüneisen parameter. Indeed, in this study we find a value of  $\sigma^A = 0.30$  for the strength of anharmonicity in LiH, which can be expected to be even larger when nuclear quantum effects are considered.<sup>2</sup> We therefore suggest LiH as an interesting yet simple candidate for studying the interplay of strong anharmonicity and nuclear quantum effects in bulk solids in future work.

Another noteworthy material in the list is SnSe: We predict the thermal conductivity of SnSe to be  $1.40 \pm 0.38 \text{ W/mK}$ , which is on the upper limit of the experimental references and agrees reasonably with the value of  $1.3 \text{ W/mK}$  found by Wei and coworkers [10]. However, this value is twice as big as the ultralow thermal conductivity of  $0.6 \text{ W/mK}$  reported in the seminal work on record-high thermoelectric figure of merit in Snse by Zhao and coworkers [8]. Our findings support the critique of Wei and coworkers that the SnSe crystals studied by Zhao and coworkers contained a non-negligible amount of defects and were heavily modified structurally, as reflected by an approximately 10 % lower density of the studied samples compared to theoretical bulk limit and measurements reported by other groups [10].

### 6.3 New materials and relation to anharmonicity

After validating the aiGK method against experimental literature, we present results for 33 materials *without* experimental reference. We display these values in the context of the  $\kappa$  vs.  $\sigma^A$  plot introduced in Fig. 4.9, where we identified a power-law relation of experimental thermal conductivities with the anharmonicity measure  $\sigma^A$  for simple elementary and binary materials. We show the data again in Fig. 6.4, but this time including the additional, non-experimentally measured materials computed in this work. It is apparent that the correlation between thermal conductivity  $\kappa$  and  $\sigma^A$  carries over from the simple materials to the more complex binary and ternary compound classes studied in this work, since the power-law fit in Fig. 6.4 is still performed with respect to the experimental values initially presented in Fig. 4.9.

<sup>1</sup> Lindsay used an LDA exchange-correlation functional, which can deviate  $\pm 20\%$  from the PBEsol functional used in this work [15]. However, the disagreement with experiment is still significantly larger than the potential inaccuracy stemming from the xc functional.

<sup>2</sup> NQE increase the anharmonic strength of LiH at room temperature to about  $\sigma^A = 0.36$  [171].

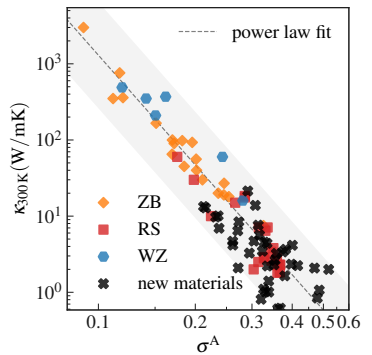


Figure 6.4: Thermal conductivity at room temperature vs. anharmonicity measure.

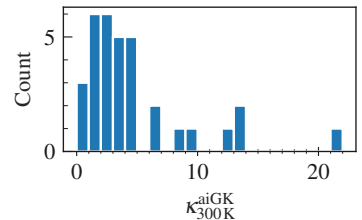
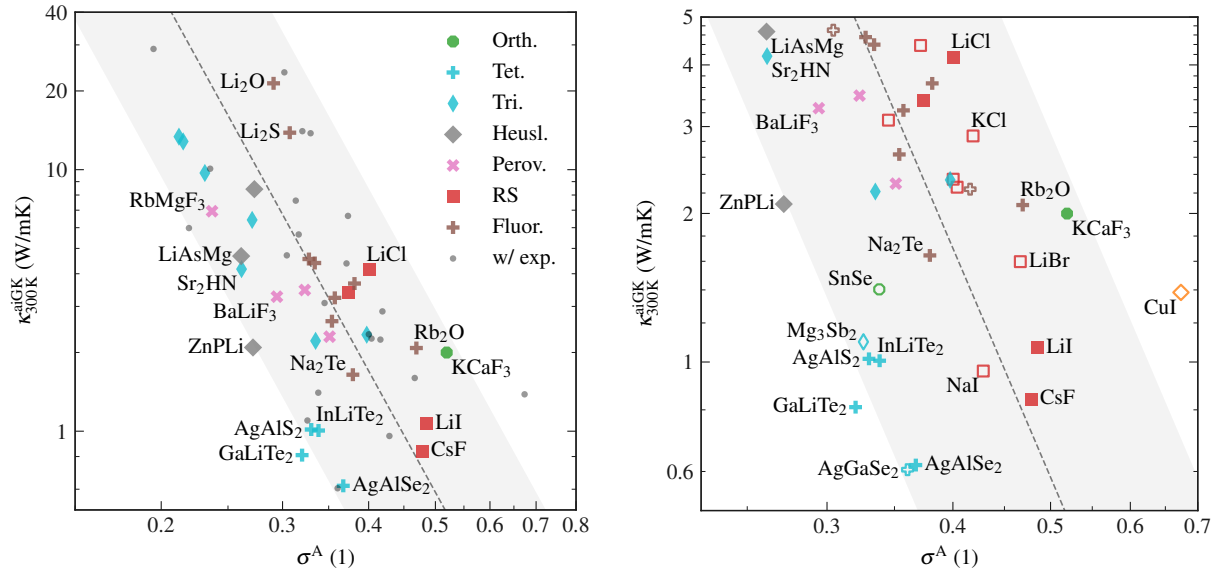


Figure 6.5: Summary of the range of thermal conductivities for materials without experimental reference found in this study.

While the overall trend of decreasing thermal conductivity with increasing anharmonicity is clearly preserved, the spread of  $\kappa$  values for materials with similar  $\sigma^A$  or vice versa increases, which is expected due to the increased structural and chemical complexity of the studied materials.

Focusing on the new materials, we show a zoomed-in part of the  $\kappa - \sigma^A$  plane in Fig. 6.6, with only computational data, highlighting the materials where no experimental reference is available. In particular, we find 28 new



materials with a computed bulk thermal conductivity of  $\kappa^{aiGK} < 10$  W/mK, 24 of which show  $\kappa^{aiGK} < 5$  W/mK, and 8 with  $\kappa^{aiGK} \leq 2$  W/mK, i. e., comparable to the bulk thermal conductivity of existing and candidate thermoelectric materials such as Bi<sub>2</sub>Te<sub>3</sub> and Bi<sub>2</sub>Se<sub>3</sub> (1.3 W/mK [172, 173]), PbTe (2.0 W/mK [174]), SnSe (1 W/mK [8, 10, 175]), M<sub>2</sub>Sb<sub>3</sub> (2.3 W/mK [176, 177]), or GeTe (2.5 W/mK [178]). A full list of all values is given in Tab. 6.3, and a histogram of the values is shown in Fig. 6.5. The materials of very low thermal conductivity comprise simple binary, cubic materials such as the rock salt structures CsF ( $\kappa^{aiGK} = 0.84$ ) and LiI ( $\kappa^{aiGK} = 1.07$ ), or the fluorite structure Na<sub>2</sub>Te ( $\kappa^{aiGK} = 1.64$ ), but also more complex structures such as the strongly anharmonic perovskites KCdF<sub>3</sub> ( $\kappa^{aiGK} = 1.67$ ) and KCaF<sub>3</sub> ( $\kappa^{aiGK} = 2.00$ ).

### 6.3.1 Chalcopyrite systems

Particularly noteworthy is a class of ternary materials, so-called *chalcopyrites*, a tetragonal crystal class closely related to the zincblende structure [179]. These crystals have been studied in the past primarily because of their non-linear optical properties [180], but also thermal transport properties have been studied [181, 179, 182], mainly because thermal transport can limit the optical efficiency in these devices [183]. However, experimental references for this class of materials are scarce, and do not agree well [183]. Picking AgGaSe<sub>2</sub> as an example, there are two distinct measurements available as summarized in Tab. 6.1, ranging from 1.1 – 2.7 W/mK [183, 184]. These values are

Figure 6.6: Thermal conductivity at room temperature computed via *ab initio* Green Kubo (aiGK) vs. anharmonicity measure. Filled symbols denote materials without experimental reference. Left: Overview of studied materials without experimental reference. Materials with experimental reference are included as small dots for reference. Right: Zoom into the region  $\kappa \leq 5$  W/mK. Open symbols represent materials where experimental reference is available.

Reference	Thermal conductivity at 300 K (W/mK)
Berger 1966 [184]	2.7
Beasley 1995 [183]	1.1
This work	$0.6 \pm 0.2$

Table 6.1: Overview of experimental references for AgGaSe<sub>2</sub>. [update values](#).

complemented by calculated values based on semi-empirical models, ranging from 4.8 – 9.0 W/mK [179, 185]. Our computed thermal conductivities are collected in Tab. 6.2.

Material	$\kappa^{\text{aiGK}}$	$\sigma^A$
AgAlS <sub>2</sub>	$1.01 \pm 0.20$	0.33
AgAlSe <sub>2</sub>	$0.62 \pm 0.16$	0.37
AgGaSe <sub>2</sub>	$0.61 \pm 0.18$	0.35
GaLiTe <sub>2</sub>	$0.81 \pm 0.15$	0.31
InLiTe <sub>2</sub>	$1.01 \pm 0.26$	0.33

Table 6.2: Overview of computed thermal conductivities for chalcopyrite materials.

Besides AgGaSe<sub>2</sub>, there is experimental reference for the chemically closely related material, AgGaS<sub>2</sub>, with a measured thermal conductivity of 1.4 W/mK [183]. While our computational data might underestimate the thermal conductivity in these compounds slightly<sup>4</sup>, we nevertheless see a clear indication of very low intrinsic thermal conductivity in AgGaSe<sub>2</sub>, and the chemically closely related compounds AgAlS<sub>2</sub> and AgAlSe<sub>2</sub>. At least regarding their thermal transport properties, they are therefore comparable or even superior to the existing thermoelectric materials listed in the previous section, while being free of heavy metals such as Pb or Bi.

To qualitatively elucidate the nuclear dynamics of the chalcopyrite systems, we present phonon spectral functions obtained from a temperature dependent model Hamiltonian for the nuclear system up to third-order displacements to estimate phonon-phonon interactions in Fig. 6.7 [145, 186, 46]. The common feature of these dispersions are the very flat acoustic branches which vary less than 1 THz across the entire Brillouin zone, and a multitude of flat, nearly degenerate optical branches showing very little to no dispersion. From a phonon-theory point of view, non-dispersive branches correspond to localized atomic motion in the system and therefore carry little heat beyond the Einstein-like diffusion of thermal energy from atom to atom, which is the dominant heat transport mechanism in structurally disordered systems like glasses [105]. Furthermore, in particular the optical branches are substantially broadened, which corresponds to strong anharmonic coupling in these systems, reducing their thermal conductivity.

<sup>3</sup>While we included AgGaS<sub>2</sub> in our dataset, we needed to discard the material because of aiMD convergence problems. However, we like to mention this material in the context of this study as potentially interesting material for future investigations.

<sup>4</sup> Please keep in mind, that the absolute errors are only of the order of 0.5-1 W/mK.

## 6.4 Conclusion

We have estimated the convergence of aiGK simulations in terms of an effective simulation time focusing on the slow degrees of freedom of the system, and validated the approach against experimental values from the literature.

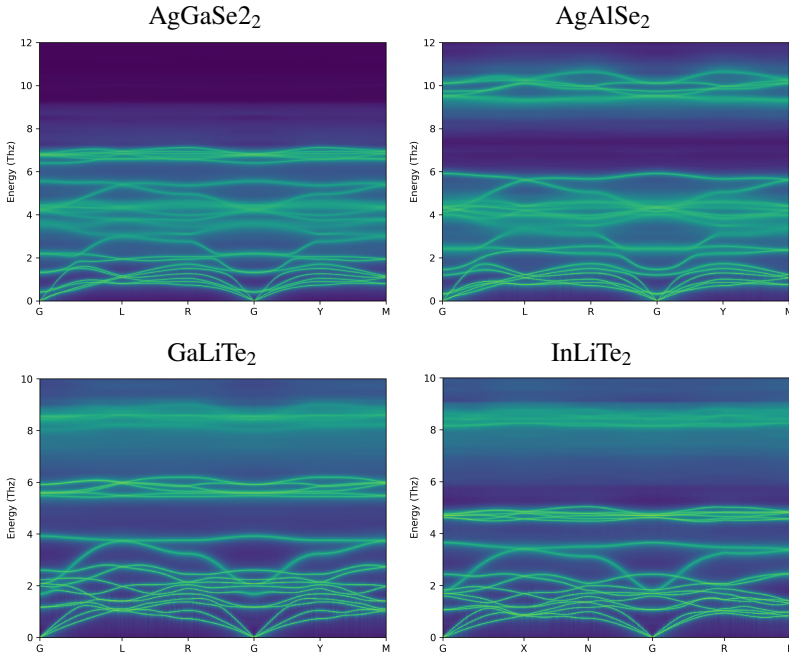


Figure 6.7: Spectral functions for the chalcopyrite materials,  $\text{AgGaSe}_2$ ,  $\text{AgAlSe}_2$ ,  $\text{GaLiTe}_2$ , and  $\text{InLiTe}_2$ .

In total, we computed thermal conductivities for 57 materials and verified our screening approach in terms of the anharmonicity measure  $\sigma^A$ . We found that the overall trend of decreasing thermal conductivity when anharmonicity increases initially inferred from the set of simple compounds carried over qualitatively to the more complex bulk materials considered in this work. We presented thermal conductivities for 33 materials where experimental reference is not yet available, and identified the family of chalcopyrite crystals as a potentially interesting class of low thermal conductivity compounds, with several systems showing very low thermal conductivity of  $\kappa \approx 1 \text{ W/mK}$  at room temperature, which is comparable to or even below currently investigated thermoelectric candidates such as SnSe or  $\text{Mg}_2\text{Sb}_3$  [8, 10, 175, 177, 189, 190, 191, 192, 193]

Space group	material	$\kappa^{\text{aiGK}}$	$\sigma^A$
122	AgAlSe <sub>2</sub>	0.62	0.37
122	GaLiTe <sub>2</sub>	0.81	0.32
225	CsF	0.84	0.48
122	InLiTe <sub>2</sub>	1.01	0.34
122	AgAlS <sub>2</sub>	1.01	0.33
225	LiI	1.07	0.49
225	Na <sub>2</sub> Te	1.64	0.38
62	KCdF <sub>3</sub>	1.67	0.53*
62	KCaF <sub>3</sub>	2.00	0.52
225	Rb <sub>2</sub> O	2.08	0.47
216	ZnPLi	2.09	0.27
166	InNaSe <sub>2</sub>	2.22	0.34
221	CsCdF <sub>3</sub>	2.30	0.35
166	InLiSe <sub>2</sub>	2.34	0.40
225	Na <sub>2</sub> Se	2.63	0.35
225	Li <sub>2</sub> Te	3.24	0.36
221	BaLiF <sub>3</sub>	3.27	0.29
225	KH	3.39	0.37
221	RbZnF <sub>3</sub>	3.47	0.32
225	K <sub>2</sub> O	3.67	0.38
225	LiCl	4.14	0.40
166	Sr <sub>2</sub> HN	4.17	0.26
225	Na <sub>2</sub> S	4.40	0.33
225	Li <sub>2</sub> Se	4.55	0.33
216	LiAsMg	4.67	0.26
166	LiScS <sub>2</sub>	6.42	0.27
221	RbMgF <sub>3</sub>	6.94	0.24
216	LiNZn	8.42	0.27
166	InNaO <sub>2</sub>	9.71	0.23
166	CuGaO <sub>2</sub>	12.82	0.22
166	LiRhO <sub>2</sub>	13.37	0.21
225	Li <sub>2</sub> S	13.85	0.31
225	Li <sub>2</sub> O	21.39	0.29

Table 6.3: Bulk thermal conductivities for materials without experimental reference. \*: The anharmonicity measure for KCaF<sub>3</sub> is increased when the entire simulation is taken into account with  $\sigma^A \approx 1.32$ , since the simulation is close to a structural phase transition. We observe jumps in  $\sigma^A(t)$  similar to those discussed for KCaF<sub>3</sub> in Sec. 4, but more pronounced. When KCdF<sub>3</sub> is close to the orthorombic reference,  $\sigma^A \approx 0.53$ . Structural phase transition are known to occur in KCdF<sub>3</sub> at around 470 K [187, 188].

# 7

## Conclusion

### 7.1 Summary

We have presented a systematic study of *ab initio* thermal transport in experimentally known semiconductors and insulators, focusing on strongly anharmonic systems. To this end, we have developed a novel scheme based on first-principles force calculations which enables to measure the “strength of anharmonicity” in materials across chemical space, and facilitates to uncover strongly anharmonic dynamical effects in individual systems in a computationally efficient way [121]. We found that this measure of anharmonicity,  $\sigma^A$ , correlates significantly with experimental thermal conductivities, and used the logic to predict materials with potentially low thermal conductivity based on estimating their anharmonic strength.

To study heat transport in these systems, we have presented a comprehensive exposition of classical Green-Kubo theory from first principles in the framework of DFT, and discussed the implementation of a slightly adapted version of the *ab initio* Green Kubo (aiGK) method first presented by Carbogno and coworkers in Ref. [15] in FHI-vibes [141]. In Chp. 6.2, we have verified this approach by computing thermal conductivities at room temperature for 24 materials which are well characterized by experiments. We computed 33 more materials without experimental reference, finding 28 materials with low thermal conductivity  $\kappa < 10 \text{ W/mK}$ , with several materials in the range of state-of-the-art thermoelectrics  $\leq 2 \text{ W/mK}$ , in particular the class of chalcopyrite materials discussed in Sec. 6.3.1.

The number of materials studied in this work with fully non-perturbative *ab initio* Green Kubo theory of thermal transport is therefore an order of magnitude higher than all previously published results for solid systems combined. These comprise solid silicon and zirconia [15], ice X [16], and amorphous silica [17].<sup>1</sup>

<sup>1</sup> Further aiGK calculations have been published for liquids: Liquid Argon, heavy water, and water in different phases [14, 17, 16].

FROM A METHODOLOGICAL POINT OF VIEW, we have presented a prototypical implementation of a data-driven approach for novel materials discovery: We leveraged existing knowledge to identify trends in material space based on an efficient descriptor, predicted candidate materials based on the descriptor, and studied the reduced number of materials by a high-accuracy method.

## 7.2 Outlook

To conclude the thesis, we want to give a short outlook on topics and questions that naturally arise from this project.

### 7.2.1 Remaining open questions

One question that is not fully answered after this project is at which degree of anharmonicity fully non-perturbative Green Kubo calculations become necessary to compute accurate thermal conductivities, and when perturbative treatment in terms of cubic or cubic and quartic anharmonic contributions in the framework of self-consistent or effective phonons is sufficient [186, 106, 194, 109, 108]. The conceptual tools for studying this question have been laid out completely in this work: The anharmonicity measure  $\sigma^A$  can be generalized to quantify third, fourth, and higher order anharmonicity separately in straightforward manner. Furthermore, the molecular dynamics data produced in this work are made accessible to the community so that force constants models as input for perturbative expressions of thermal conductivity can be extracted with regression or sensing approaches [195, 196]. And of course, the thermal conductivities computed in this work can serve as benchmark for identifying materials with significant deviations which are suited for further testing. This should be possible as of now at least for the binary systems with high symmetry studied in this work, as for more complex systems a treatment of quartic anharmonicity might become infeasible because of the unfavorable scaling of quartic force constants with number of irreducible atoms, see the discussion in appendix D of Ref. [108].

### 7.2.2 Next steps for materials discovery

Our screening for thermal insulators was governed by a single computational parameter, i. e., the anharmonicity measure  $\sigma^A$ . It is certain that including further structural and harmonic material properties in semi-empirical equations derived by feature extraction techniques can improve thermal conductivity predictions and thereby accelerate materials discovery [197, 198, 122, 199]. The systematic data computed in the course of this project can serve as a testbed for these approaches.

### 7.2.3 Next steps for *ab initio* Green Kubo

As presented in the previous chapters, the *ab initio* Green Kubo method in its current formulation uses an interpolation approach to deal with long-wavelength phonons, assuming an approximative scaling  $\tau_{\mathbf{q},b} \propto \omega_{\mathbf{q},b}^{-2}$ , where  $\tau_{\mathbf{q},b}$  denotes the lifetime and  $\omega_{\mathbf{q},b}$  the angular frequency of a phonon with wave vector  $\mathbf{q}$  and band index  $b$ . This relationship, however, only holds for crystals of certain lattice types in the limit of vanishing wave vector and small anharmonicity [112]. Especially when working on intermediate levels of anharmonicity, where phonons with long wavelengths are more important, an improvement of the current interpolation scheme is certainly desirable, e. g., by using the full phonon spectral function  $S(\mathbf{q}, \omega)$  which implicitly

contains information about frequencies  $\omega_{\mathbf{q},b}$  and lifetimes  $\tau_{\mathbf{q},b}$ , lends itself for interpolation in momentum space, and can be systematically improved by surrogate models beyond the harmonic approximation [200]. More advanced surrogate models could also help to map out long-lived contributions better, thereby reducing the necessary amount of effective simulation time,  $t_0^{\text{eff}}$ , by converging out the harmonic contribution to heat transport faster than in the current approach. The data produced in the course of this work can serve as a basis to develop and test ideas in that regard.

#### 7.2.4 Challenges for *ab initio* Green Kubo

We see the following challenges with the current formulation of the *ab initio* Green Kubo method that are worth further investigation:

THE ISSUES OF DEFECTS AND ISOTOPE SCATTERING have only been briefly mentioned in the discussion of thermal transport in MgO in Sec. 5.4, but have not been further investigated in this work, although they are known to impact thermal conductivity in actual materials [201]. In a supercell-based *ab initio* approach, these effects are notoriously difficult to study because of the required system sizes and time scales [202]. However, these are technical and not conceptual issues which might be possible to solve by the increasing computational power, or by surrogate models based on a DFT description of the potential energy surface, see also Sec. 7.3.1.

THE TOPIC OF CONVECTIVE CONTRIBUTIONS TO THE HEAT FLUX has been touched in Chp. 3. As these are absent in the virial-based heat flux formulation used in this work, this rules out any study of materials with noticeable self diffusion. Furthermore, as discussed in Sec. 2.3.1 and appendix A of Ref. [93], there is no rigorous mathematical proof for the assumption of vanishing convective contributions to the thermal conductivity even in system without any self diffusion, since those can, in principle, contribute through the cross-correlation of convective and non-convective currents. While those are often negligible [88], it would be interesting to estimate the strength of this effect. One could compute convective contributions to the heat flux based on a force constants model, and evaluate its contribution. This should be sufficient to quantify the expected deviation, and materials with noticeable deviation could be interesting to study further, if any are found.

NUCLEAR QUANTUM EFFECTS (NQE) have been mentioned in the discussion of LiF in Sec. 6.2. These are inherently absent in the formulation of classical Green Kubo theory, and correct treatment of NQE for dynamical effects such as heat transport poses a formidable challenge already on a conceptual level, i. e., in the definition of a heat flux estimator, and the correct evaluation of Kubo-transformed quantum mechanical correlation functions. However, some very recent path-integral molecular dynamics based approaches using classical force fields show some promising progress in the field [203, 204].

### 7.3 Perspective

After discussing the status quo and potential futures of the methods used in this work, I want to discuss more long-term trends that are currently emerging in the field of heat transport simulations, and might have the power to push the topic forward considerably: Green-Kubo simulations using machine-learned expressions for the potential energy function  $\mathcal{V}(\mathbf{R})$  [205, 206, 207], and model Hamiltonian-based approaches using Boltzmann transport theory [105] or analytical Green's functions [91, 208].

#### 7.3.1 Machine learning Green Kubo

The advent of machine-learned potentials with *ab initio* quality [209, 210, 211, 212, 213] coupled with on-the-fly or active-learning training strategies [214, 215, 216, 217] promises to become a versatile tool for dynamical simulations of materials in a range of subfields, especially for phenomena where the electronic structure of a given material is only of secondary importance, i. e., in uncharged systems with electronically trivial defects. In such materials, machine-learned potentials can remove computational bottlenecks when aiming for statistical convergence in simulation time, as well as system and ensemble sizes, which in turn could make GK-based transport simulations of new materials accessible to more researchers than currently. While several proofs of principle for GK simulations from machine-learned potentials exist already [205, 206, 207], some more fundamental problems persist, e. g., the question of transferability across temperature and phase transitions in particular, or how long-range electrostatic interactions in polar systems can be properly described in these models [218, 219, 220, 221]. From materials discovery perspective, where one aims at studying a multitude of systems, it remains to be seen how straightforward and robust the parametrization of these force fields can be achieved in practice, and if the extra cost in human time in order to train the potentials can be reduced to a minimum without compromising their reliability. The aiGK data computed and made available in the course of this project can help to develop and benchmark these approaches.

#### 7.3.2 Boltzmann transport and analytical Green's functions

A complementary route for not too complex materials is the use of model Hamiltonians coupled with perturbation theory in the framework of lattice dynamics, which become increasingly sophisticated and continue to develop [222, 145, 186, 223, 194, 224]. While these approaches are limited to non-diffusing materials with a definite long-range structural order and limited complexity,<sup>2</sup> they allow to study subtle dynamical effects such as the behavior of thermal transport close to and across phase transitions with very good precision [208], which is particularly important for potential thermoelectrics such as SnSe and GeTe [8, 225, 208]. Further, these methods give straightforward access to nuclear quantum effects [226], which is a formidable task for molecular dynamics-based Green Kubo methods as discussed above.

Worth noting are more recent approaches that try to bridge the gap between

<sup>2</sup> See comments in Sec. 7.2.1.

state of the art Boltzmann transport [105] and analytical Green Kubo in terms of phonon Green's functions [91, 208]. Combined with self-consistent sampling techniques [227], these approaches promise to be a very efficient alternative for heat transport simulations in a wide class of solid systems.

Last but not least, lattice-dynamics techniques can be coupled with molecular dynamics simulations to extract fully anharmonic properties such as phonon lifetimes, e. g., as we use them in the *ab initio* Green Kubo method [92, 228, 229, 15, 230] – the opportunities for combining these approaches are certainly not exhausted.



## Bibliography

- [1] W Schottky. *Thermodynamik*. Springer, Berlin.
- [2] Power plant operations report. [https://www.eia.gov/electricity/annual/html/epa\\_08\\_01.html](https://www.eia.gov/electricity/annual/html/epa_08_01.html).
- [3] David R. Clarke, Matthias Oechsner, and Nitin P. Padture. Thermal-barrier coatings for more efficient gas-turbine engines. 37(10):891–898.
- [4] John H Perepezko. ideal performance (given by the green curve) exceeds that of actual engines (blue bullets) and reflects inefficiencies. These performance data reveal a trou-. 326(November).
- [5] D.R. Clarke and C.G. Levi. Materials Design for the Next Generation Thermal Barrier Coatings. 33(1):383–417.
- [6] G Jeffrey Snyder and Eric S Toberer. Complex thermoelectric materials. 7(2):105–114.
- [7] G. S. Nolas, J. Sharp, and H. J. Goldsmid. *Thermoelectrics, Basic Principles and New Materials Developments*, chapter 1. Springer.
- [8] Li-Dong Zhao, Shih-Han Lo, Yongsheng Zhang, Hui Sun, Gangjian Tan, Ctirad Uher, C. Wolverton, Vinayak P. Dravid, and Mercouri G. Kanatzidis. Ultralow thermal conductivity and high thermoelectric figure of merit in SnSe crystals. 508(7496):373–377.
- [9] Springer materials. <http://materials.springer.com>. Accessed: 2019-11-07.
- [10] Pai-Chun Wei, S. Bhattacharya, J. He, S. Neeleshwar, R. Podila, Y. Y. Chen, and A. M. Rao. The intrinsic thermal conductivity of SnSe. 539(7627):E1–E2.
- [11] Donald T. Morelli and Glen A. Slack. High Lattice Thermal Conductivity Solids. In Subhash L. Shindé and Jitendra S. Goela, editors, *High Thermal Conductivity Materials*, pages 37–68. Springer-Verlag.
- [12] M. Fierz and V. F. Weisskopf. *Theoretical physics in the twentieth century: A memorial volume to Wolfgang Pauli*. Interscience Publishers, New York-London.
- [13] David A Broido, Michael Malorny, Gerd Birner, Natalio Mingo, and DA Stewart. Intrinsic lattice thermal conductivity of semiconductors from first principles. 91(23):231922.

- [14] Aris Marcolongo, Paolo Umari, and Stefano Baroni. Microscopic theory and quantum simulation of atomic heat transport. 12(1):80–84.
- [15] Christian Carbogno, Rampi Ramprasad, and Matthias Scheffler. Ab initio Green-Kubo Approach for the Thermal Conductivity of Solids. 118(175901):1–5.
- [16] Federico Grasselli, Lars Stixrude, and Stefano Baroni. Heat and charge transport in H<sub>2</sub>O at ice-giant conditions from ab initio molecular dynamics simulations. 11(1):3605.
- [17] Aris Marcolongo, Loris Ercole, and Stefano Baroni. Gauge fixing for heat-transport simulations. 16(5):3352–3362.
- [18] Paul Adrien Maurice Dirac. Quantum mechanics of many-electron systems. 123(792):714–733.
- [19] Gerd Czycholl. *Theoretische Festkörperphysik: von den klassischen Modellen zu modernen Forschungsthemen*. Springer-Verlag.
- [20] M. Born and R. Oppenheimer. 4(84):457.
- [21] Max Born and Kun Huang. *Dynamical theory of crystal lattices*. Clarendon Press.
- [22] Max Born. *Kopplung der Elektronen-und Kernbewegung in Molekülen und Kristallen*, volume 6. Vandenhoeck und Ruprecht.
- [23] Dominik Marx and Jürg Hutter. *Ab initio molecular dynamics: basic theory and advanced methods*. Cambridge University Press.
- [24] JM Ziman. The electron-phonon interaction, according to the adiabatic approximation. In *Mathematical Proceedings of the Cambridge Philosophical Society*, volume 51, pages 707–712. Cambridge University Press.
- [25] Walter Kohn. Highlights of condensed matter theory. In *International School of Physics” Enrico Fermi*, pages 1–15.
- [26] Pierre Hohenberg and Walter Kohn. Inhomogeneous electron gas. 136(3B):B864.
- [27] Hans Hellmann. *Hans Hellmann: Einführung in Die Quantenchemie: Mit Biografischen Notizen von Hans Hellmann Jr.* Springer-Verlag.
- [28] R. P. Feynman. Forces in molecules. 56:340–343.
- [29] Paul Bendt and Alex Zunger. Simultaneous relaxation of nuclear geometries and electric charge densities in electronic structure theories. 50(21):1684–1688.
- [30] Che Ting Chan, Klaus Peter Bohnen, and KM Ho. Accelerating the convergence of force calculations in electronic-structure computations. 47(8):4771–4774.
- [31] Peter Pulay. Ab initio calculation of force constants and equilibrium geometries in polyatomic molecules: I. theory. 17(2):197–204.

- [32] Walter Kohn and Lu Jeu Sham. Self-consistent equations including exchange and correlation effects. 140(4A):A1133.
- [33] D. M. Ceperley. Ground State of the Electron Gas by a Stochastic Method. 45(7):566–569.
- [34] Ryo Nagai, Ryosuke Akashi, and Osamu Sugino. Completing density functional theory by machine learning hidden messages from molecules. 6(1):43.
- [35] Reiner M Dreizler and Eberhard KU Gross. *Density functional theory: an approach to the quantum many-body problem*. Springer Science & Business Media.
- [36] John P. Perdew, J. A. Chevary, S. H. Vosko, Koblar A. Jackson, Mark R. Pederson, D. J. Singh, and Carlos Fiolhais. Atoms, molecules, solids, and surfaces: Applications of the generalized gradient approximation for exchange and correlation. 46:6671–6687.
- [37] Aron J. Cohen, Paula Mori-Sánchez, and Weitao Yang. Insights into Current Limitations of Density Functional Theory. 321(5890):792–794.
- [38] Aron J. Cohen, Paula Mori-Sánchez, and Weitao Yang. Challenges for Density Functional Theory. 112(1):289–320.
- [39] Donald E Sands. *Vectors and tensors in crystallography*. Dover Publications.
- [40] Paul Adrien Maurice Dirac. *The principles of quantum mechanics*. Number 27. Oxford university press.
- [41] Donald E Sands. *Introduction to crystallography*. W. A. Benjamin.
- [42] Max Born. *Atomtheorie des Festen Zustandes (Dynamik der Kristallgitter)*. Springer-Verlag.
- [43] K. Parlinski, Z. Li, and Y. Kawazoe. First-Principles Determination of the Soft Mode in Cubic ZrO<sub>2</sub>. 78(21):4063–4066.
- [44] AA t MARADUDIN and So H Vosko. Symmetry properties of the normal vibrations of a crystal. 40(1):1.
- [45] Peter E. Blöchl, O. Jepsen, and O. K. Andersen. Improved tetrahedron method for brillouin-zone integrations. 49:16223–16233.
- [46] Gordon Leslie Squires. *Introduction to the theory of thermal neutron scattering*. Courier Corporation.
- [47] G. Nilsson and G. Nelin. Study of the homology between silicon and germanium by thermal-neutron spectrometry. 6(10):3777–3786.
- [48] A. Bulou, A.W. Hewat, F. J. Schäfer, and J. Nouet. Structural phase transitions in KCaF<sub>3</sub>- DSC, birefringence and neutron powder diffraction results. 25(1):375–378.

- [49] D. Z. Demetriou, C. R.A. Catlow, A. V. Chadwick, G. J. McLntyre, and I. Abrahams. The anion disorder in the perovskite fluoride KCaF<sub>3</sub>. 176(17-18):1571–1575.
- [50] K. S. Knight, C. N. W. Darlington, and I. G. Wood. The crystal structure of KCaF<sub>3</sub> at 4.2 and 300 K: A re-evaluation using high-resolution powder neutron diffraction . 20(1):7–13.
- [51] Ph. Daniel, M. Rousseau, and J. Toulouse. Raman Scattering Study of Potassium Calcium Fluoride KCaF<sub>3</sub>. 203:327.
- [52] Lev Davidovich Landau and Evgenii Mikhailovich Lifshitz. *Quantum mechanics: non-relativistic theory*, volume 3. Elsevier.
- [53] Paul Ehrenfest. Bemerkung über die angenäherte Gültigkeit der klassischen Mechanik innerhalb der Quantenmechanik. 45(7-8):455–457.
- [54] Jean-Louis Basdevant. *Lectures on quantum mechanics*. Springer.
- [55] M Parrinello and A Rahman. Polymorphic transitions in single crystals: A new molecular dynamics method. 52(12):7182–7190.
- [56] R. Car and M. Parrinello. Unified Approach for Molecular Dynamics and Density-Functional Theory. 55(22):2471–2474.
- [57] M Parrinello and A Rahman. Study of an F center in molten KCl. 80(2):860–867.
- [58] Thomas E. Markland and Michele Ceriotti. Nuclear quantum effects enter the mainstream. 2(3):0109.
- [59] Yair Litman, Jörg Behler, and Mariana Rossi. Temperature dependence of the vibrational spectrum of porphycene: a qualitative failure of classical-nuclei molecular dynamics. 221:526–546.
- [60] George DJ Phillips. *Elementary lectures in statistical mechanics*. Springer Science & Business Media.
- [61] Mark Tuckerman. *Statistical mechanics: theory and molecular simulation*. Oxford university press.
- [62] Erwin Schrödinger. *Statistical thermodynamics*. Courier Corporation.
- [63] Loup Verlet. Computer "Experiments" on Classical Fluids. I. Thermo-dynamical Properties of Lennard-Jones Molecules. 159(1):98–103.
- [64] Eric Vanden-Eijnden and Giovanni Cicotti. Second-order integrators for langevin equations with holonomic constraints. 429(1-3):310–316.
- [65] Shuichi Nosé. A unified formulation of the constant temperature molecular dynamics methods. 81(1):511–519.
- [66] William G. Hoover. Canonical dynamics: Equilibrium phase-space distributions. 31(3):1695–1697.
- [67] Giovanni Bussi, Davide Donadio, and Michele Parrinello. Canonical sampling through velocity rescaling. 126(1):014101.

- [68] M. Dove. *Introduction to lattice dynamics*. Cambridge University Press.
- [69] D. West and S. K. Estreicher. First-principles calculations of vibrational lifetimes and decay channels: Hydrogen-related modes in Si. 96(11):22–25.
- [70] Daan Frenkel and Berend Smit. *Understanding Molecular Simulations*. Academic Press, Elsevier.
- [71] Gilles H Peslherbe, Haobin Wang, and William L Hase. Monte carlo sampling for classical trajectory simulations. 105:171–201.
- [72] Jean Baptiste Joseph Baron Fourier. *The analytical theory of heat*. The University Press.
- [73] PL Kapitza. Heat transfer and superfluidity of helium ii. 60(4):354.
- [74] Aleandro Antidormi and Luciano Colombo. *Lattice Thermal Boundary Resistance*, pages 845–863. Springer International Publishing.
- [75] Albert Einstein. Über die von der molekularkinetischen theorie der wärme geforderte bewegung von in ruhenden flüssigkeiten suspendierten teilchen. 4.
- [76] Harry Nyquist. Thermal agitation of electric charge in conductors. 32(1):110.
- [77] Herbert B Callen and Theodore A Welton. Irreversibility and generalized noise. 83(1):34.
- [78] Ryogo Kubo. Statistical-mechanical theory of irreversible processes. i. general theory and simple applications to magnetic and conduction problems. 12(6):570–586.
- [79] Melville S. Green. Markoff random processes and the statistical mechanics of time-dependent phenomena. 20(8):1281–1295.
- [80] Ryogo Kubo, Mario Yokota, and Sadao Nakajima. Statistical-mechanical theory of irreversible processes. ii. response to thermal disturbance. 12(11):1203–1211.
- [81] Stefano Baroni, Riccardo Bertossa, Loris Ercole, Federico Grasselli, and Aris Marcolongo. Heat transport in insulators from ab initio green-kubo theory. pages 809–844.
- [82] Lars Onsager. Reciprocal relations in irreversible processes. i. 37(4):405.
- [83] James A. McLennan. Statistical Mechanics of the Steady State. 115(6):1405–1409.
- [84] James A McLennan. Statistical Mechanics of Transport in Fluids. 3(4):493.

- [85] R Zwanzig. Time-Correlation Functions and Transport Coefficients in Statistical Mechanics. 16(1):67–102. Discussion of "thermal processes": Problem of representing effect of temperature gradient through perturbation Hamiltonian.
- [86] Eugene Helfand. Transport coefficients from dissipation in a canonical ensemble. 119(1):1.
- [87] Bingqing Cheng and Daan Frenkel. Computing the heat conductivity of fluids from density fluctuations. 125(13):130602.
- [88] R Vogelsang, C Hoheisel, and G Ciccotti. Thermal conductivity of the lennard-jones liquid by molecular dynamics calculations. 86(11):6371–6375.
- [89] Alper Kinaci, Justin B Haskins, and Tahir Çağın. On calculation of thermal conductivity from einstein relation in equilibrium molecular dynamics. 137(1):014106.
- [90] Loris Ercole, Aris Marcolongo, Paolo Umari, and Stefano Baroni. Gauge invariance of thermal transport coefficients. 185(1-2):79–86.
- [91] Leyla Isaeva, Giuseppe Barbalinardo, Davide Donadio, and Stefano Baroni. Modeling heat transport in crystals and glasses from a unified lattice-dynamical approach. 10(1):1–6.
- [92] Anthony JC Ladd, Bill Moran, and William G Hoover. Lattice thermal conductivity: A comparison of molecular dynamics and anharmonic lattice dynamics. 34(8):5058.
- [93] Loris Ercole. ab initio Simulation of Heat Transport in Silica Glass.
- [94] Zheyong Fan, Luiz Felipe C Pereira, Hui-Qiong Wang, Jin-Cheng Zheng, Davide Donadio, and Ari Harju. Force and heat current formulas for many-body potentials in molecular dynamics simulations with applications to thermal conductivity calculations. 92(9):094301.
- [95] Paul Boone, Hasan Babaei, and Christopher E Wilmer. Heat flux for many-body interactions: corrections to lammps. 15(10):5579–5587.
- [96] Stephen Stackhouse, Lars Stixrude, and Bijaya B. Karki. Thermal conductivity of periclase (mgo) from first principles. 104:208501.
- [97] Franz Knuth, Christian Carbogno, Viktor Atalla, Volker Blum, and Matthias Scheffler. All-electron formalism for total energy strain derivatives and stress tensor components for numeric atom-centered orbitals. 190:33–50.
- [98] Volker Blum, Ralf Gehrke, Felix Hanke, Paula Havu, Ville Havu, Xinguo Ren, Karsten Reuter, and Matthias Scheffler. Ab initio molecular simulations with numeric atom-centered orbitals. 180(11):2175–2196.
- [99] P Debye. Vorträge über die kinetische theorie der materie und der elektrizität.

- [100] Rudolf Peierls. Zur kinetischen theorie der wärmeleitung in kristallen. 395(8):1055–1101.
- [101] Robert J Hardy. Energy-flux operator for a lattice. 132(1):168.
- [102] John W Negele. *Quantum many-particle systems*. Addison-Wesley Publishing.
- [103] Gyaneshwar P Srivastava. *The physics of phonons*. Routledge.
- [104] Jaroslav Fabian and Philip B Allen. Anharmonic decay of vibrational states in amorphous silicon. 77(18):3839.
- [105] Michele Simoncelli, Nicola Marzari, and Francesco Mauri. Unified theory of thermal transport in crystals and glasses. 15(8):809–813.
- [106] Tianli Feng and Xiulin Ruan. Quantum mechanical prediction of four-phonon scattering rates and reduced thermal conductivity of solids. 93(4):1–10.
- [107] Tianli Feng, Lucas Lindsay, and Xiulin Ruan. Four-phonon scattering significantly reduces intrinsic thermal conductivity of solids. 96(16):1–6.
- [108] Navaneetha K Ravichandran and David Broido. Unified first-principles theory of thermal properties of insulators. 98(8):085205.
- [109] Yi Xia. Revisiting lattice thermal transport in PbTe: The crucial role of quartic anharmonicity. 113(7).
- [110] Yi Xia, Vinay I Hegde, Koushik Pal, Xia Hua, Dale Gaines, Shane Patel, Jiangang He, Muratahan Aykol, and Chris Wolverton. High-throughput study of lattice thermal conductivity in binary rocksalt and zinc blende compounds including higher-order anharmonicity. 10(4):041029.
- [111] Navaneetha K Ravichandran and David Broido. Phonon-Phonon Interactions in Strongly Bonded Solids: Selection Rules and Higher-Order Processes. 10(2):021063.
- [112] Conyers Herring. Role of low-energy phonons in thermal conduction. 95(4):954.
- [113] Marcello Puligheddu, Yi Xia, Maria Chan, and Giulia Galli. Computational prediction of lattice thermal conductivity: A comparison of molecular dynamics and boltzmann transport approaches. 3(8):085401.
- [114] Christian Carbogno, Carlos G. Levi, Chris G. Van de Walle, and Matthias Scheffler. Ferroelastic switching of doped zirconia: Modeling and understanding from first principles. 90:144109.
- [115] Terumasa Tadano and Shinji Tsuneyuki. Self-consistent phonon calculations of lattice dynamical properties in cubic  $\text{srto}_3$  with first-principles anharmonic force constants. 92:054301.

- [116] C Ulrich, A Göbel, K Syassen, and M Cardona. Pressure-induced disappearance of the raman anomaly in cucl. 82(2):351.
- [117] Thomas M. Brenner, Christian Gehrman, Roman Korobko, Tsachi Livneh, David A. Egger, and Omer Yaffe. Anharmonic host-lattice dynamics enable fast ion conduction in superionic agi. 4:115402.
- [118] Y. Shen, C. N. Saunders, C. M. Bernal, D. L. Abernathy, M. E. Manley, and B. Fultz. Anharmonic origin of the giant thermal expansion of nabr. 125:085504.
- [119] M Hidaka, S Yamashita, and Y Okamoto. Study of structural phase transitions of kcaf3. 81(1):177–183.
- [120] Marios Zacharias and Feliciano Giustino. One-shot calculation of temperature-dependent optical spectra and phonon-induced band-gap renormalization. 94(7).
- [121] Florian Knoop, Thomas A. R. Purcell, Matthias Scheffler, and Christian Carbogno. Anharmonicity measure for materials. 4:083809.
- [122] Lihua Chen, Huan Tran, Rohit Batra, Chiho Kim, and Rampi Ram-prasad. Machine learning models for the lattice thermal conductivity prediction of inorganic materials. 170:109155.
- [123] Eric S. Toberer, Alex Zevalkink, and G. Jeffrey Snyder. Phonon engineering through crystal chemistry. 21(40):15843–15852.
- [124] E van Lenthe, E J Baerends, and J G Snijders. Relativistic total energy using regular approximations. 101(11):9783–9792.
- [125] William P. Huhn and Volker Blum. One-hundred-three compound band-structure benchmark of post-self-consistent spin-orbit coupling treatments in density functional theory. 1(3):033803.
- [126] Rundong Zhao, Victor Wen-zhe Yu, Kimberly Zhang, Yunlong Xiao, Yong Zhang, and Volker Blum. Quasi-four-component method with numeric atom-centered orbitals for relativistic density functional simulations of molecules and solids. 103(24):245144.
- [127] James B Boyce and Bernardo A Huberman. Superionic conductors: Transitions, structures, dynamics. 51(4):189–265.
- [128] JB Boyce, TM Hayes, JC Mikkelsen Jr, and W Stutius. Exafs investigation of superionic conduction in cui. 33(2):183–189.
- [129] JB Boyce, TM Hayes, and JC Mikkelsen Jr. Extended-x-ray-absorption-fine-structure investigation of mobile-ion density in superionic agi, cui, cubr, and cucl. 23(6):2876.
- [130] DA Keen and S Hull. The high-temperature structural behaviour of copper (i) iodide. 7(29):5793.
- [131] Sadao Hoshino. Crystal structure and phase transition of some metallic halides (iv) on the anomalous structure of  $\alpha$ -agi. 12(4):315–326.

- [132] Leater W Strock. Kristallstruktur des hochtemperatur-jod-silbers a-agj. 25(1):441–459.
- [133] LW Strock. Supplement and announcement on:" the crystal structure of high temperature-iodien silver alpha-agj". 31(1/2):132–136.
- [134] Lester W Strock. A classification of crystal structures with defect lattices. 93(1):285–311.
- [135] RP Lowndes. Anharmonicity in the silver and thallium halides: low-frequency dielectric response. 6(12):4667.
- [136] W Andreoni and MP Tosi. Premelting lattice disorder in agbr and pbf2. 11(1):49–55.
- [137] DR Batchelor, P Tangyunyong, TN Rhodin, YT Tan, and KJ Lushington. Anharmonicity in agbr exafs. 94(3):179–182.
- [138] J. K. Aboagye and R. J. Friauf. Anomalous high-temperature ionic conductivity in the silver halides. 11:1654–1664.
- [139] D Wilmer, K Funke, T Luxermann, and SM Bennington. Dynamic aspects of frenkel defect formation in silver chloride and silver bromide. 411.
- [140] David S Mebane and Joachim Maier. Dc conductivity and dielectric properties in silver chloride, revisited. 12(10):2478–2487.
- [141] Florian Knoop, Matthias Scheffler, Christian Carbogno, et al. Fhi-vibes: \_ab initio\_ vibrational simulations. 5(56):2671.
- [142] Reese E Jones and Kranthi K Mandadapu. Adaptive green-kubo estimates of transport coefficients from molecular dynamics based on robust error analysis. 136(15):154102.
- [143] John P. Perdew, Adrienn Ruzsinszky, Gábor I. Csonka, Oleg A. Vydrov, Gustavo E. Scuseria, Lucian A. Constantin, Xiaolan Zhou, and Kieron Burke. Restoring the Density-Gradient Expansion for Exchange in Solids and Surfaces. 100(13):136406.
- [144] Ask Hjorth Larsen, Jens Jørgen Mortensen, Jakob Blomqvist, Ivano E Castelli, Rune Christensen, Marcin Dułak, Jesper Friis, Michael N Groves, Bjørk Hammer, Cory Hargus, et al. The atomic simulation environment—a python library for working with atoms. 29(27):273002.
- [145] Olle Hellman, Peter Steneteg, I A Abrikosov, and S I Simak. Temperature dependent effective potential method for accurate free energy calculations of solids. 87(10):104111.
- [146] A Togo and I Tanaka. First principles phonon calculations in materials science. 108:1–5.
- [147] Jie Chen, Gang Zhang, and Baowen Li. How to improve the accuracy of equilibrium molecular dynamics for computation of thermal conductivity? 374(23):2392–2396.

- [148] Abraham Savitzky and Marcel JE Golay. Smoothing and differentiation of data by simplified least squares procedures. 36(8):1627–1639.
- [149] Eric Jones, Travis Oliphant, Pearu Peterson, et al. SciPy: Open source scientific tools for Python.
- [150] Atsushi Togo and Isao Tanaka. Spglib: a software library for crystal symmetry search.
- [151] FR Charvat and WD Kingery. Thermal conductivity: xiii, effect of microstructure on conductivity of single-phase ceramics. 40(9):306–315.
- [152] Glen A Slack. Thermal conductivity of mgo, al<sub>2</sub>o<sub>3</sub>, mg al<sub>2</sub>o<sub>4</sub>, and fe<sub>3</sub>o<sub>4</sub> crystals from 3° to 300° k. 126(2):427.
- [153] YS Touloukian, RW Powell, CY Ho, and PG Klemens. Thermal conductivity: Nonmetallic solids, vol. 2 of tprc data series.
- [154] W. R MACPHERSON and H. H. SCHLOESSIN. Apparent, lattice and radiative, thermal conductivity at temperatures from 300 to 1500 K and pressures up to 5.6 GPa: Results for MgO and NaCl. 15(5):495–509.
- [155] Nico de Koker. Thermal conductivity of mgo periclase from equilibrium first principles molecular dynamics. 103(12):125902.
- [156] Xiaoli Tang and Jianjun Dong. Lattice thermal conductivity of mgo at conditions of earth's interior. 107(10):4539–4543.
- [157] Haruhiko Dekura, Taku Tsuchiya, et al. Ab initio lattice thermal conductivity of mgo from a complete solution of the linearized boltzmann transport equation. 95(18):184303.
- [158] S. Andersson and G. Bäckström. Techniques for determining thermal conductivity and heat capacity under hydrostatic pressure. 57(8):1633–1639.
- [159] Douglas Allen Dalton, Wen-Pin Hsieh, Gregory T Hohensee, David G Cahill, and Alexander F Goncharov. Effect of mass disorder on the lattice thermal conductivity of mgo periclase under pressure. 3(1):1–5.
- [160] Anne M Hofmeister. Thermal diffusivity and thermal conductivity of single-crystal mgo and al<sub>2</sub>o<sub>3</sub> and related compounds as a function of temperature. 41(5):361–371.
- [161] Jose J Plata, Pinku Nath, Demet Usanmaz, Jesus Carrete, Cormac Toher, Maarten de Jong, Mark Asta, Marco Fornari, Marco Buongiorno Nardelli, and Stefano Curtarolo. An efficient and accurate framework for calculating lattice thermal conductivity of solids: Aflow—aapl automatic anharmonic phonon library. 3(1):1–10.
- [162] Dale L. Perry. *Handbook of Inorganic Compounds*. CRC Press, zeroth edition.

- [163] Glen A. Slack and Per Andersson. Pressure and temperature effects on the thermal conductivity of CuCl. 26(4):1873–1884.
- [164] C. Yang, D. Souchay, M. Kneiß, M. Bogner, H. M. Wei, M. Lorenz, O. Oeckler, G. Benstetter, Y. Q. Fu, and M. Grundmann. Transparent flexible thermoelectric material based on non-toxic earth-abundant p-type copper iodide thin film. 8(1):16076.
- [165] J Coroa, BM Morais Faustino, A Marques, C Bianchi, T Koskinen, T Juntunen, I Tittonen, and I Ferreira. Highly transparent copper iodide thin film thermoelectric generator on a flexible substrate. 9(61):35384–35391.
- [166] Atsushi Togo, Laurent Chaput, and Isao Tanaka. Distributions of phonon lifetimes in brillouin zones. 91(9):094306.
- [167] G.A. Slack. Nonmetallic crystals with high thermal conductivity. 34(2):321–335.
- [168] Sebastian G. Volz and Gang Chen. Molecular-dynamics simulation of thermal conductivity of silicon crystals. 61(4):2651–2656.
- [169] S. Volz, J.B Saulnier, G. Chen, and P. Beauchamp. Computation of thermal conductivity of Si/Ge superlattices by molecular dynamics techniques. 31(9-10):815–819.
- [170] L. Lindsay. Isotope scattering and phonon thermal conductivity in light atom compounds: LiH and LiF. 94(17):174304.
- [171] Hagen-Henrik Kowalski. private communication.
- [172] H J Goldsmid. The Thermal Conductivity of Bismuth Telluride. 69(2):203–209.
- [173] C. B. Satterthwaite and R. W. Ure. Electrical and Thermal Properties of Bi<sub>2</sub>Te<sub>3</sub>. 108(5):1164–1170.
- [174] A. A. El-Sharkawy, A. M. Abou El-Azm, M. I. Kenawy, A. S. Hillal, and H. M. Abu-Basha. Thermophysical properties of polycrystalline PbS, PbSe, and PbTe in the temperature range 300–700 K. 4(3):261–269.
- [175] S. Sassi, C. Candolfi, J.-B. Vaney, V. Ohorodniichuk, P. Masschelein, A. Dauscher, and B. Lenoir. Assessment of the thermoelectric performance of polycrystalline *p*-type SnSe. 104(21):212105.
- [176] Faraz Ahmadpour, Taras Kolodiazhnyi, and Yurij Mozharivskyj. Structural and physical properties of Mg<sub>3-x</sub>Zn<sub>x</sub>Sb<sub>2</sub> (x=0–1.34). 180(9):2420–2428.
- [177] Yu Pan, Mengyu Yao, Xiaochen Hong, Yifan Zhu, Fengren Fan, Kazuki Imasato, Yangkun He, Christian Hess, Jörg Fink, Jiong Yang, Bernd Büchner, Chenguang Fu, G. Jeffrey Snyder, and Claudia Felser. Mg<sub>3</sub>(Bi,Sb)<sub>2</sub> single crystals towards high thermoelectric performance. 13(6):1717–1724.

- [178] Suresh Perumal, Subhajit Roychowdhury, Devendra S. Negi, Ranjan Datta, and Kanishka Biswas. High Thermoelectric Performance and Enhanced Mechanical Stability of p-type Ge<sub>1-x</sub> Sb<sub>x</sub> Te. 27(20):7171–7178.
- [179] SM Wasim. Thermal conductivity of ternary compounds. 51(1):K35–K40.
- [180] Ching-Hwa Ho and Chia-Chi Pan. Optical behavior and structural property of cuals<sub>2</sub> and agals<sub>2</sub> wide-bandgap chalcopyrites. 53(22):E7–E13.
- [181] D.P. Spitzer. Lattice thermal conductivity of semiconductors: A chemical bond approach. 31(1):19–40.
- [182] L Garbato and A Rucci. Thermal conductivity and ionicity in chalcopyrite semiconductors. 64(2):350–351.
- [183] J. Donald Beasley. Thermal conductivities of some novel nonlinear optical materials. 33(6):1000.
- [184] Lev I. Berger and Vitalii D. Prochukhan. *Ternary Diamond-Like Semiconductors*. Springer US.
- [185] C Rincón, ML Valeri-Gil, and SM Wasim. Room-temperature thermal conductivity and grüneisen parameter of the i-iii-vi<sub>2</sub> chalcopyrite compounds. 147(2):409–415.
- [186] Olle Hellman and I. A. Abrikosov. Temperature-dependent effective third-order interatomic force constants from first principles. 88:144301.
- [187] M Hidaka, S Hosogi, M Ono, and K Horai. Structural phase transitions in kcdf3. 23(7):503–506.
- [188] M Hidaka, ZY Zhou, and S Yamashita. Structural phase transitions in kcdf3 and k0.5rb0.5cdf3. 20(1-2):83–94.
- [189] Takenobu Kajikawa, Naoyuki Kimura, and Takahiro Yokoyama. Thermoelectric properties of intermetallic compounds: Mg<sub>3</sub>bi<sub>2</sub> and mg<sub>3</sub>sb<sub>2</sub> for medium temperature range thermoelectric elements. In *Proceedings ICT'03. 22nd International Conference on Thermoelectrics (IEEE Cat. No. 03TH8726)*, pages 305–308. IEEE.
- [190] Cathie L Condron, Susan M Kauzlarich, Franck Gascoin, and G Jeffrey Snyder. Thermoelectric properties and microstructure of mg<sub>3</sub>sb<sub>2</sub>. 179(8):2252–2257.
- [191] KX Zhang, XY Qin, HX Xin, HJ Li, and Jian Zhang. Transport and thermoelectric properties of nanocrystal substitutional semiconductor alloys (mg<sub>1-x</sub>cdx) sb<sub>2</sub> doped with ag. 484(1-2):498–504.
- [192] Jiawei Zhang, Lirong Song, Mattia Sist, Kasper Tolborg, and Bo Brummerstedt Iversen. Chemical bonding origin of the unexpected isotropic physical properties in thermoelectric mg<sub>3</sub>sb<sub>2</sub> and related materials. 9(1):1–10.

- [193] Jingxuan Ding, Tyson Lanigan-Atkins, Mario Calderón-Cueva, Arnab Banerjee, Douglas L Abernathy, Ayman Said, Alexandra Zevalkink, and Olivier Delaire. Soft anharmonic phonons and ultralow thermal conductivity in mg<sub>3</sub> (sb, bi) 2 thermoelectrics. 7(21):eabg1449.
- [194] Terumasa Tadano and Shinji Tsuneyuki. First-principles lattice dynamics method for strongly anharmonic crystals. 87(4):041015.
- [195] Fei Zhou, Weston Nielson, Yi Xia, and Vidvuds Ozoliņš. Lattice Anharmonicity and Thermal Conductivity from Compressive Sensing of First-Principles Calculations. 113(18):185501.
- [196] Erik Fransson, Fredrik Eriksson, and Paul Erhart. Efficient construction of linear models in materials modeling and applications to force constant expansions. 6(1):135.
- [197] Runhai Ouyang, Stefano Curtarolo, Emre Ahmetcik, Matthias Scheffler, and Luca M Ghiringhelli. Sisso: A compressed-sensing method for identifying the best low-dimensional descriptor in an immensity of offered candidates. 2(8):083802.
- [198] Bryan R Goldsmith, Mario Boley, Jilles Vreeken, Matthias Scheffler, and Luca M Ghiringhelli. Uncovering structure-property relationships of materials by subgroup discovery. 19(1):013031.
- [199] Thomas AR Purcell, Matthias Scheffler, Luca M Ghiringhelli, and Christian Carbogno. A60.00008: Uncovering the relationship between thermal conductivity and anharmonicity with symbolic regression.
- [200] A. A. Maradudin and A. E. Fein. Scattering of Neutrons by an Anharmonic Crystal. 128(6):2589–2608.
- [201] Jean-François Bisson, Danièle Fournier, Martine Poulain, Odile Lavigne, and Rémy Mévrel. Thermal Conductivity of Yttria-Zirconia Single Crystals, Determined with Spatially Resolved Infrared Thermography. 83(8):1993–1998.
- [202] T M Gibbons, By Kang, S K Estreicher, and C Carbogno. Thermal conductivity of Si nanostructures containing defects: Methodology, isotope effects, and phonon trapping. 84(3):035317.
- [203] Ripeng Luo and Kuang Yu. Capturing the nuclear quantum effects in molecular dynamics for lattice thermal conductivity calculations: Using ice as example. 153(19):194105.
- [204] Benjamin J Sutherland, William HD Moore, and David E Manolopoulos. Nuclear quantum effects in thermal conductivity from centroid molecular dynamics. 154(17):174104.
- [205] Pavel Korotaev, Ivan Novoselov, Aleksey Yanilkin, and Alexander Shapeev. Accessing thermal conductivity of complex compounds by machine learning interatomic potentials. 100(14).
- [206] R. Li, E. Lee, and T. Luo. A unified deep neural network potential capable of predicting thermal conductivity of silicon in different phases. 12:100181.

- [207] Claudia Mangold, Shunda Chen, Giuseppe Barbalinardo, Jörg Behler, Pascal Pochet, Konstantinos Termentzidis, Yang Han, Laurent Chapat, David Lacroix, and Davide Donadio. Transferability of neural network potentials for varying stoichiometry: Phonons and thermal conductivity of  $Mn_xGe_y$  compounds. 127(24):244901.
- [208] Đorđe Dangić, Olle Hellman, Stephen Fahy, and Ivana Savić. The origin of the lattice thermal conductivity enhancement at the ferroelectric phase transition in  $gete$ . 7(1):1–8.
- [209] Sönke Lorenz, Axel Groß, and Matthias Scheffler. Representing high-dimensional potential-energy surfaces for reactions at surfaces by neural networks. 395(4-6):210–215.
- [210] Jörg Behler and Michele Parrinello. Generalized neural-network representation of high-dimensional potential-energy surfaces. 98:146401.
- [211] Albert P. Bartók, Mike C. Payne, Risi Kondor, and Gábor Csányi. Gaussian approximation potentials: The accuracy of quantum mechanics, without the electrons. 104:136403.
- [212] Albert P. Bartók, Risi Kondor, and Gábor Csányi. On representing chemical environments. 87:184115.
- [213] Alexander V Shapeev. Moment tensor potentials: A class of systematically improvable interatomic potentials. 14(3):1153–1173.
- [214] Zhenwei Li, James R. Kermode, and Alessandro De Vita. Molecular dynamics with on-the-fly machine learning of quantum-mechanical forces. 114:096405.
- [215] Ryosuke Jinnouchi, Jonathan Lahnsteiner, Ferenc Karsai, Georg Kresse, and Menno Bokdam. Phase transitions of hybrid perovskites simulated by machine-learning force fields trained on the fly with bayesian inference. 122:225701.
- [216] Evgeny V Podryabinkin and Alexander V Shapeev. Active learning of linearly parametrized interatomic potentials. 140:171–180.
- [217] Peitao Liu, Carla Verdi, Ferenc Karsai, and Georg Kresse.  $\alpha-\beta$  phase transition of zirconium predicted by on-the-fly machine-learned force field. 5:053804.
- [218] Nongnuch Artrith, Tobias Morawietz, and Jörg Behler. High-dimensional neural-network potentials for multicomponent systems: Applications to zinc oxide. 83:153101.
- [219] Andrea Grisafi and Michele Ceriotti. Incorporating long-range physics in atomic-scale machine learning. 151(20):204105.
- [220] Shuwen Yue, Maria Carolina Muniz, Marcos F Calegari Andrade, Linfeng Zhang, Roberto Car, and Athanassios Z Panagiotopoulos. When do short-range atomistic machine-learning models fall short? 154(3):034111.

- [221] David Peter Kovacs, Cas van der Oord, Jiri Kucera, Alice Allen, Daniel Cole, Christoph Ortner, and Gabor Csanyi. Linear atomic cluster expansion force fields for organic molecules: beyond rmse.
- [222] Keivan Esfarjani and Harold T. Stokes. Method to extract anharmonic force constants from first principles calculations. 77:144112.
- [223] Ion Errea, Matteo Calandra, and Francesco Mauri. Anharmonic free energies and phonon dispersions from the stochastic self-consistent harmonic approximation: Application to platinum and palladium hydrides. 89(6):064302.
- [224] Fei Zhou, Weston Nielson, Yi Xia, and Vidvuds Ozoliņš. Compressive sensing lattice dynamics. i. general formalism. 100:184308.
- [225] Antoine Dewandre, Olle Hellman, Sandip Bhattacharya, Aldo H. Romero, Georg K. H. Madsen, and Matthieu J. Verstraete. Two-step phase transition in snse and the origins of its high power factor from first principles. 117:276601.
- [226] Nina Shulumba, Olle Hellman, and Austin J Minnich. Lattice thermal conductivity of polyethylene molecular crystals from first-principles including nuclear quantum effects. 119(18):185901.
- [227] Sandra E Brown, Ionuț Georgescu, and Vladimir A Mandelshtam. Self-consistent phonons revisited. ii. a general and efficient method for computing free energies and vibrational spectra of molecules and clusters. 138(4):044317.
- [228] J. E. Turney, E. S. Landry, A. J. H. McGaughey, and C. H. Amon. Predicting phonon properties and thermal conductivity from anharmonic lattice dynamics calculations and molecular dynamics simulations. 79:064301.
- [229] Dong-Bo Zhang, Tao Sun, and Renata M. Wentzcovitch. Phonon quasiparticles and anharmonic free energy in complex systems. 112:058501.
- [230] Albert Glensk, Blazej Grabowski, Tilmann Hickel, Jörg Neugebauer, Jürgen Neuhaus, Klaudia Hradil, Winfried Petry, and Michael Leitner. Phonon lifetimes throughout the brillouin zone at elevated temperatures from experiment and ab initio. 123:235501.
- [231] Jean-Louis Basdevant and Jean Dalibard. *Quantum Mechanics*. Springer.
- [232] Mildred S Dresselhaus, Gene Dresselhaus, and Ado Jorio. *Group theory: application to the physics of condensed matter*. Springer Science & Business Media.
- [233] R. Penrose. A generalized inverse for matrices. 51(3):406–413.
- [234] Jorge Nocedal and Stephen Wright. *Numerical optimization*. Springer Science & Business Media.

- [235] Bernd G Pfrommer, Michel Côté, Steven G Louie, and Marvin L Cohen. Relaxation of crystals with the quasi-newton method. 131(1):233–240.
- [236] E. B. Tadmor, G. S. Smith, N. Bernstein, and E. Kaxiras. Mixed finite element and atomistic formulation for complex crystals. 59:235–245.
- [237] Roland Lindh, Anders Bernhardsson, Gunnar Karlström, and Per-Åke Malmqvist. On the use of a hessian model function in molecular geometry optimizations. 241(4):423–428.
- [238] Charles Kittel, Jochen Matthias Gress, and Anne Lessard. *Einführung in die Festkörperphysik*, volume 14. Oldenbourg München.
- [239] John Frederick Nye et al. *Physical properties of crystals: their representation by tensors and matrices*. Oxford university press.
- [240] Jean-Pierre Hansen and Ian R McDonald. *Theory of simple liquids*. Elsevier.
- [241] Pascal Vinet, John R Smith, John Ferrante, and James H Rose. Temperature effects on the universal equation of state of solids. 35(4):1945.
- [242] David Lomen and James Mark. *Ordinary Differential Equations with Linear Algebra*. Prentice Hall.
- [243] Lasse Bjerg, Bo B. Iversen, and Georg K. H. Madsen. Modeling the thermal conductivities of the zinc antimonides ZnSb and Zn<sub>4</sub>Sb<sub>3</sub>. 89(2):024304.
- [244] Kohsuke Hashimoto, Ken Kurosaki, Yasushi Imamura, Hiroaki Muta, and Shinsuke Yamanaka. Thermoelectric properties of BaSi<sub>2</sub>, SrSi<sub>2</sub>, and LaSi. 102(6):063703.
- [245] D. Li and X. Y. Qin. Thermoelectric properties of CuSbSe<sub>2</sub> and its doped compounds by Ti and Pb at low temperatures from 5to310K. 100(2):023713.
- [246] M.C. Goetz and J.A. Cowen. The thermal conductivity of silver iodide. 41(4):293–295.
- [247] Joseph P. Feser, Emory M. Chan, Arun Majumdar, Rachel A. Segalman, and Jeffrey J. Urban. Ultralow Thermal Conductivity in Polycrystalline CdSe Thin Films with Controlled Grain Size. 13(5):2122–2127.
- [248] Glen A. Slack. Thermal Conductivity of II-VI Compounds and Phonon Scattering by Fe<sub>2</sub> + Impurities. 6(10):3791–3800.
- [249] Ji-Guang Li, Takayasu Ikegami, and Toshiyuki Mori. Fabrication of transparent Sc<sub>2</sub>O<sub>3</sub> ceramics with powders thermally pyrolyzed from sulfate. 18(8):1816–1822.
- [250] Ching-Hua Su. Thermal conductivity, electrical conductivity, and thermoelectric properties of CdTe and Cd<sub>0.8</sub>Zn<sub>0.2</sub>Te crystals between room temperature and 780 °C. 5(5):057118.

- [251] D Gerlich and P Andersson. Temperature and pressure effects on the thermal conductivity and heat capacity of CsCl, CsBr and CsI. 15(25):5211–5222.
- [252] Mattia Sist, Karl Frederik Faerch Fischer, Hidetaka Kasai, and Bo Brummerstedt Iversen. Low-Temperature Anharmonicity in Cesium Chloride (CsCl). 56(13):3625–3629.
- [253] J. J. Martin, G. S. Dixon, and P. P. Velasco. Phonon scattering in RbCa<sub>3</sub>F<sub>3</sub> and KMnF<sub>3</sub>. 14(6):2609–2612.
- [254] Yasutaka Suemune and Hyō Ikawa. Thermal Conductivity of KMnF<sub>3</sub>, KCoF<sub>3</sub>, KNiF<sub>3</sub>, and KZnF<sub>3</sub> Single Crystals. 19(9):1686–1690.
- [255] S. R. Popuri, A. J. M. Scott, R. A. Downie, M. A. Hall, E. Suard, R. De-court, M. Pollet, and J.-W. G. Bos. Glass-like thermal conductivity in SrTiO<sub>3</sub> thermoelectrics induced by A-site vacancies. 4(64):33720–33723.
- [256] Hiroaki Muta, Ken Kurosaki, and Shinsuke Yamanaka. Thermoelectric properties of reduced and La-doped single-crystalline SrTiO<sub>3</sub>. 392(1-2):306–309.
- [257] Kashif Kamran, M Anis-ur-Rehman, and Asghari Maqsood. Thermal and electrical properties of crystalline silver bromide. 40(3):869–873.
- [258] R. G. Ross, P. Andersson, and G. Bäckström. Thermal conductivity and heat capacity of solid AgCl under pressure. 2(3):289–300.
- [259] Asghari Maqsood, M Anis-ur-Rehman, Kashif Kamran, and Iftikhar Hussain Gul. Thermophysical properties of AgCl in the temperature range 77–300 K. 37(13):1845–1847.
- [260] P Andersson. Thermal conductivity under pressure and through phase transitions in solid alkali halides. I. Experimental results for KCl, KBr, KI, RbCl, RbBr and RbI. 18(20):3943–3955.
- [261] B Hakansson and R G Ross. Thermal conductivity and heat capacity of solid LiBr and RbF under pressure. 1(25):3977–3985.
- [262] I. Sigalas, B. Håkanson, and P. Andersson. Thermal conductivity and heat capacity of solid nabr under pressure. 6(2):177–190.
- [263] B. Håkansson and P. Andersson. Thermal conductivity and heat capacity of solid NaCl and NaI under pressure. 47(4):355–362.
- [264] H. H. Li, R. A. Matula, J. M. Yang, H. R. Hume, and A. Shakoor. Physical Properties Data for Rock Salt.
- [265] Y. S. Touloukian, R. W. Powell, C. Y. Ho, and P. G. Klemens. Thermophysical Properties of Matter - The TPRC Data Series. Volume 2. Thermal Conductivity - Nonmetallic Solids.

- [266] P. A. Popov, P. P. Fedorov, and V. V. Osiko. Thermal conductivity of single crystals with a fluorite structure: Cadmium fluoride. 52(3):504–508.
- [267] J. P. Moore, F. J. Weaver, R. S. Graves, and D. L. McElroy. The Thermal Conductivities of SrCl<sub>2</sub> and SrF<sub>2</sub> from 85 to 400 K. In T. Ashworth and David R. Smith, editors, *Thermal Conductivity 18*, pages 115–124. Springer US.

# **Appendix**



# **Appendix**



# A

## Notation

### A.1 Indexation

Throughout the thesis, we use the following symbols to index and label the appearing quantities:

- $\alpha, \beta, \gamma, \delta$ : Cartesian component indices,
- $\mu, \nu, \rho$ : crystal-basis component indices,
- $I, J$ : atom number labels,
- $i, j$ : atom labels in the primitive cell,
- $\mathbf{L}, \mathbf{K}$ : lattice vectors.

We use a contra/covariant notation for vector components following Sands [39], with an Einstein convention,

$$\mathbf{x} \cdot \mathbf{y} = \sum_{\alpha} x^{\alpha} y_{\alpha} \equiv x^{\alpha} y_{\alpha},$$

for sums over vector components. In particular, we have

- $\mathbf{R}_I = (R_I^1, R_I^2, R_I^3)$ : Atomic position of atom  $I$  in a Cartesian components.
- $\{\mathbf{a}_{\mu}\}$ : crystal basis with lattice vectors  $\mathbf{a}_{\mu}$ .
- $\{\mathbf{a}^{\mu}\}$ : dual basis with inverse lattice vectors  $\mathbf{a}^{\mu}$  fulfilling  $\mathbf{a}^{\mu} \cdot \mathbf{a}_{\nu} = \delta_{\nu}^{\mu}$ .  
The cartesian components of  $\{\mathbf{a}^{\mu}\}$  and  $\{\mathbf{a}_{\mu}\}$  are related by

$$a_{\alpha}^{\mu} = (a^{-1t})_{\mu\alpha}.$$

- $\mathbf{R}_I = R_I^{\mu} \mathbf{a}_{\mu}$ : Atomic position of atom  $I$  expressed in the crystal basis  $\{\mathbf{a}_{\mu}\}$ . The are  $R_I^{\mu}$  are also called *scaled* or *fractional* components. They are related to the Cartesian components  $R_I^{\alpha}$  by  $R_I^{\mu} = \mathbf{a}^{\mu} \cdot \mathbf{R}_I = (a^{-1t})_{\mu\alpha} R_I^{\alpha}$  by the identity stated above.
- $\mathbf{L} = L^{\mu} \mathbf{a}_{\mu}$ : A lattice vector  $\mathbf{L}$  expressed in the crystal basis  $\{\mathbf{a}_{\mu}\}$ .
- $\{\mathbf{b}^{\mu}\}$ : reciprocal lattice vectors fulfilling  $\mathbf{b}^{\mu} \cdot \mathbf{a}_{\nu} = 2\pi \delta_{\nu}^{\mu}$ , i.e.,  $\mathbf{b}^{\mu} = 2\pi \mathbf{a}^{\mu}$  with the crystallographic convention of including the factor  $2\pi$  in the basis defintion.
- $\mathbf{q} = q_{\mu} \mathbf{b}^{\mu}$ : phonon wave vector in the reciprocal lattice basis  $\{\mathbf{b}^{\mu}\}$ .

- $\mathbf{q} \cdot \mathbf{R}_I = 2\pi q_\mu R_I^\mu$ : scalar product of wave vector with atomic position.

We remind the reader that in Cartesian space, indices can be lowered and raised arbitrarily, i. e., the components  $x^\alpha$  and  $x_\alpha$  are equal.

# B

## Bloch Theorem and Brillouin Zone

*“The idea of periodicity in the reciprocal space is useless but, I think, harmless.”*

Paul Gartner

### B.1 Bloch Theorem

The Schrödinger equation in 1d reads

$$\hat{H}\psi(x) = \left(-\frac{\nabla^2}{2m} + V(x)\right)\psi(x) = E\psi(x). \quad (\text{B.1})$$

In a periodic potential,

$$V(x+a) = V(x), \quad (\text{B.2})$$

the periodicity can be expressed by stating that the translation operator  $\hat{T}_a$  defined by its action,

$$\hat{T}_a f(x) = f(x+a), \quad (\text{B.3})$$

commutes with the Hamiltonian,

$$[\hat{H}, \hat{T}_a] = 0. \quad (\text{B.4})$$

The eigenstates  $\psi(x)$  of  $\hat{H}$  are therefore also eigenstates of  $\hat{T}_a$  [231]. The translation operator is unitary,  $\hat{T}_a^\dagger = \hat{T}_a^{-1}$ , but not hermitian. The eigenvalues  $\lambda$  associated with  $\hat{T}_a$  are thus complex numbers. By definition, one has  $\psi(x+na) = \lambda^n \psi(x)$ . Requiring bounded solutions,  $\lim_{x \rightarrow \infty} |\psi(x)| < \infty$ , imposes the condition  $|\lambda| = 1$ . The function  $\psi$  can therefore be written as

$$\psi(x) = c(x)u(x), \quad (\text{B.5})$$

with a real, periodic function

$$u : \mathbb{R} \rightarrow \mathbb{R} \quad \text{with} \quad u(x+a) = u(x), \quad (\text{B.6})$$

and a complex function of unit modulus,

$$c : \mathbb{R} \rightarrow \mathbb{C} \quad \text{with} \quad |c(x)| = 1. \quad (\text{B.7})$$

We label each possible solution by the number  $k$ , then

$$c_k(x) = e^{ikx} \quad (\text{B.8})$$

is a map from the domain  $x \in \mathbb{R}$  to the complex unit circle  $\{ z \in \mathbb{C} : |z| = 1 \}$ . It then holds that  $\hat{T}_a \psi_k(x) = e^{ika} \psi_k(x)$ , i. e.,  $\psi_k$  is an eigenfunction of  $\hat{T}_a$  with eigenvalue  $\lambda = e^{ika}$ . We formulate the

**Theorem (Bloch).** *Solutions to the Schrödinger equation (B.1) with a periodic potential of periodicity  $a$  are of the form*

$$\psi_k(x) = e^{ikx} u_k(x),$$

with a real, periodic function  $u_k$ .

The theorem is trivially extended to the 3d case by using the multiplication rule

$$\hat{T}_{\mathbf{a}+\mathbf{b}} f(\mathbf{x}) = \hat{T}_{\mathbf{a}} \hat{T}_{\mathbf{b}} f(\mathbf{x}) \equiv f(\mathbf{x} + \mathbf{a} + \mathbf{b}). \quad (\text{B.9})$$

A more rigorous proof in terms of representation theory can be found, e. g., in [232].

## B.2 Brillouin Zone

We have not yet specified the range of the quantum number  $k$ . This can be done by requiring the complex function  $c_k$  defined in Eq. (B.8) to map the interval  $x \in [0, a)$  exactly once to the unit circle so that  $k$  is a *unique* label for the eigenvalues  $e^{ika}$  of the translation operator  $\hat{T}_a$ . We therefore define the

$$\text{Brillouin zone} = \{ k : k \in \left[ -\frac{\pi}{a}, \frac{\pi}{a} \right) \}. \quad (\text{B.10})$$

For a wavefunction belonging to  $k' = k + G$ , where  $G$  is an integer multiple of the reciprocal lattice vector  $b = 2\pi/a$ , we would find

$$\hat{T}_a \psi_{k+G}(x) = e^{ika} \psi_{k+G}(x). \quad (\text{B.11})$$

They are therefore indistinguishable by the translation operator and we define  $\psi_k$  and  $\psi_{k+G}$  to be the same function,

$$\psi_k(x) = \psi_{k+G}(x). \quad (\text{B.12})$$

This is sometimes termed “periodicity of Bloch functions in reciprocal space”.

# C

## Born-von Karman Supercell

To ensure normalizability of the functions  $\psi_{\mathbf{k}l}$ , one additionally imposes the *Born-von Karman boundary conditions*

$$\psi_{\mathbf{k}l}(\mathbf{x} + \mathbf{A}_i) = \psi_{\mathbf{k}l}(\mathbf{x}) \quad (\text{C.1})$$

where each  $\mathbf{A}_i$  is a linear combination of the primitive basis vectors  $\{\mathbf{a}_i\}$ ,

$$\mathbf{A}_i = S_i^j \mathbf{a}_j \quad \text{with } S_i^j \in \mathbb{Z}, \quad (\text{C.2})$$

where  $S$  is a non-singular matrix with integer elements. The space spanned by the  $\{\mathbf{A}_i\}$  is parallelepiped of volume  $V = N \mathbf{a}_1 \cdot (\mathbf{a}_2 \times \mathbf{a}_3)$ , where  $N = \det S$  is the number of unit cells that fit into the enlarged cell. This cell is therefore often called *supercell*, and the matrix  $S$  is denoted as a *supercell matrix*. With the Born-von Karman boundary conditions, the domain of all functions and functionals appearing in the Kohn-Sham equations become restricted to the supercell. The ideal, infinite crystal is obtained in the limit  $N \rightarrow \infty$ . Using the periodic boundary condition expressed by Eq. (1.63) in the Bloch functions given by Eq. (1.61), and the periodicity of the functions  $u_{\mathbf{k}l}$ , one finds that

$$\mathbf{k} \cdot \mathbf{A}_i = 2\pi m_i \quad \text{with } m_i \in \mathbb{N} \text{ such that } \forall i : \mathbf{k} \cdot \mathbf{a}_i \leq 2\pi. \quad (\text{C.3})$$

In total there are  $N$  permissible values of  $\mathbf{k}$  labelled by  $\mathbf{m} = (m_1, m_2, m_3)$  that can be expressed in terms of the *reciprocal lattice vectors* [39]

$$\mathbf{B}^i = 2\pi \varepsilon^{ijk} \frac{\mathbf{A}_j \times \mathbf{A}_k}{\mathbf{A}_1 \cdot (\mathbf{A}_2 \times \mathbf{A}_3)}, \quad (\text{C.4})$$

where  $\varepsilon^{ijk}$  denotes the Levi-Civita symbol enforcing the correct ordering of  $ijk$ . The complete set of  $\mathbf{k}$ -values is

$$\mathbf{k}_{\mathbf{m}} = \sum_{i=1}^3 m_i \mathbf{B}^i. \quad (\text{C.5})$$

The values of  $\mathbf{k}$  given by Eq. (1.66) are those sampled in real-space simulation in a box of the given size, i. e., the *Born-von Karman cell*.



# D

## Numerical Force Constants

The force constants  $\Phi$  can be obtained from first-order derivatives of the potential-energy surface, i.e., the forces, by rewriting the second derivative in terms of a finite difference expression,

$$\Phi_{I\alpha,J\beta} = \left. \frac{\partial^2 \mathcal{V}(\mathbf{R})}{\partial R_I^\alpha \partial R_J^\beta} \right|_{\mathbf{R}^0} = -\frac{\partial}{\partial R_I^\alpha} F_{J,\beta} = -\lim_{\epsilon \rightarrow 0} \frac{F_{J,\beta}(\{\mathbf{R}' : R_I'^\alpha = R_I^{0,\alpha} + \epsilon\}) - F_{J,\beta}(\{\mathbf{R}' : R_I'^\alpha = R_I^{0,\alpha}\})}{\epsilon}. \quad (\text{D.1})$$

In practice, atom  $I$  is displaced by a small but finite displacement  $\epsilon$  in the direction  $\alpha$ , and the force on all other atoms is recorded. By performing the displacement in all  $3N$  degrees of freedom, the  $3N \times 3N$  forces can be arranged in a matrix  $\mathbf{F}_{[3N \times 3N]}$ , and the displacements can be arranged in a matrix  $\mathbf{U}_{[3N \times 3N]} = \epsilon \mathbf{1}_{[3N \times 3N]}$ . The  $3N \times 3N$  force-constants matrix  $\Phi$  is obtained by the trivial matrix multiplication

$$\mathbf{F} = -\Phi \mathbf{U} = -\epsilon \Phi \mathbf{1} \quad (\text{D.2})$$

$$\implies \Phi = -\frac{1}{\epsilon} \mathbf{F} \mathbf{1}. \quad (\text{D.3})$$

If  $M > 3N$  displacements are used, e.g., because positive and negative displacements  $\pm\epsilon$  are used, the force constants can be obtained by solving an overdetermined linear equation of the kind

$$\mathbf{F}_{[3N \times M]} = -\Phi_{[3N \times 3N]} \mathbf{U}_{[3N \times M]} \quad (\text{D.4})$$

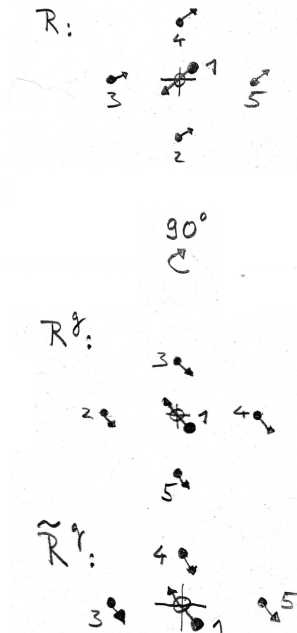
$$\implies \Phi = -\mathbf{F} \mathbf{U}^+, \quad (\text{D.5})$$

where  $\mathbf{U}^+$  denotes the Moore-Penrose pseudo inverse of the displacement matrix  $\mathbf{U}$  [233, 43].

THE NUMBER OF REQUIRED FORCE CALCULATIONS can be reduced by considering the spacegroup symmetry of the crystal. This can be achieved in two ways: First, the symmetry can be used to identify the set of inequivalent displacements from which all other forces can be constructed by the following argument: We define the representation  $\Gamma^g$  of a symmetry operation  $g$  by its action on the atomic coordinates  $\{\mathbf{R}_I = \mathbf{R}_I^0 + \mathbf{U}_I\}$  as

$$\mathbf{R}_I^g \equiv \Gamma^g(\mathbf{R}_I) = P_{IJ}^g \mathbf{R}_J^0 + M^g \mathbf{U}_I, \quad (\text{D.6})$$

where  $P_{IJ}^g$  is the permutation that relates the reference positions of atom  $I$  and atom  $J$ , and  $M^g$  is an orthogonal matrix representing the rotation (or inversion) of the respective displacement.



As depicted in Fig. D.1, the forces on each atom in the rotated system  $\mathbf{R}^g = \{\mathbf{R}_I^g\}$  are obtained by co-rotating the forces in the initial configuration  $\mathbf{R} = \{\mathbf{R}_I\}$  as

$$\mathbf{F}_I(\mathbf{R}^g) = M^g \mathbf{F}_I(\mathbf{R}), \quad (\text{D.7})$$

i. e., the forces transform as the displacements  $\mathbf{U}_I$ . Let us now define a new configuration  $\tilde{\mathbf{R}}^g$  where just the displacements  $\mathbf{U}_I$  are rotated according to  $g$ . This can be achieved by rotating the entire system according Eq. (D.6) and applying the inverse permutation  $P^{g^{-1}}$ , i. e.,

$$\tilde{\mathbf{R}}_I^g = P_{IJ}^{g^{-1}} \mathbf{R}_I^g \stackrel{(\text{D.6})}{=} \mathbf{R}_I^0 + M^g P_{IJ}^{g^{-1}} \mathbf{U}_J. \quad (\text{D.8})$$

It follows that the force on atom  $I$  in the new configuration  $\tilde{\mathbf{R}}^g$  is related to the force in the rotated system  $\mathbf{R}^g$  by this inverse permutation, so that

$$\mathbf{F}_I(\tilde{\mathbf{R}}^g) = P_{IJ}^{g^{-1}} \mathbf{F}_J(\mathbf{R}^g) = M^g P_{IJ}^{g^{-1}} \mathbf{F}_J(\mathbf{R}). \quad (\text{D.9})$$

By means of this equation, the set of forces obtained for a configuration  $\{\mathbf{R}_I = \mathbf{R}_I^0 + \mathbf{U}_I\}$  can be used to generate a set of forces for each symmetrically equivalent configuration  $\{\tilde{\mathbf{R}}_I^g = \mathbf{R}_I^0 + M^g P_{IJ}^{g^{-1}} \mathbf{U}_J\}$ , where  $g$  are space-group elements.

A complementary approach is to use the symmetry elements  $\{g\}$  to reduce the forceconstant matrix to an irreducible basis,

$$\Phi = \sum_{i=1}^D p_i \tilde{\Phi}_i, \quad (\text{D.10})$$

where the  $\tilde{\Phi}_i$  are *solely* determined by the space group elements  $\{g\}$  and analytical properties of the forceconstants, and only the *irreducible components*  $p_i$  are system dependent. The pseudoinverse procedure given in Eq. (D.5) then only has to be performed for the  $D$  parameters  $p_i$  [43]. This procedure can drastically reduce the number of free parameters in the forceconstant matrix. For example, in a  $4 \times 4 \times 4$  bcc lattice with 128 atoms,  $\Phi$  is a matrix with  $(3 \cdot 128)^2 = 147456$  elements. However, there are only  $D = 11$  irreducible parameters  $p_i$  that need to be determined [145].

**TODO:** Add the theory for symmetry reduction

## D.1 Temperature Dependent Effective Potentials

**TODO:** Add TDEP

# E

## *Geometry Optimization for Crystals*

### *E.1 Lattice optimization at zero temperature*

The task of geometry optimization is to find a local minimum  $\mathbf{R}^0$  of the potential-energy surface  $\mathcal{V}(\mathbf{R})$ . From a mathematical point of view,  $\mathcal{V}(\mathbf{R})$  is a function of the  $3N$  coordinates  $\mathbf{R}$ , or, when lattice degrees of freedom are included,  $3N + 9$  degrees of freedom.<sup>1</sup> Summarizing the positional degrees of freedom including the lattice in the generalized coordinate

$$x = \left( R_0^x, R_0^y, \dots, R_N^z; a_1^x, a_2^x, \dots, a_3^z \right), \quad (\text{E.1})$$

we seek to find

$$x^0 = \arg \min_x \mathcal{V}(x). \quad (\text{E.2})$$

The standard tools to solve this problem are very well covered in the standard reference [234]. The technical pitfalls when optimizing lattices are thoroughly discussed in [235, 236]. A slightly different approach as the ones discussed in the references listed above is taken in the molecular simulations code FHI-AIMS [98]. We therefore review this approach shortly in the following.

MANY OPTIMIZATION ALGORITHMS working with gradients as input are based on the Newton descent method in which the target function is locally approximated by a second-order Taylor expansion [234]. In our case, we denote the generalized force as  $f_x$  and the Hessian matrix of second derivatives as  $H_{xx'}$ , where

$$f_x = -\partial_x \mathcal{V}(x), \quad (\text{E.3})$$

$$H_{xx'} = \partial_x \partial_{x'} \mathcal{V}(x). \quad (\text{E.4})$$

Assuming that  $f_x$  and  $H_{xx'}$  are known, the neighborhood of a configuration  $x$  can be written to second order in a displacement  $s_x$  as

$$m(x + s_x) = \mathcal{V}(x) - s_x f_x + \frac{1}{2} s_x H_{xx'} s_{x'}. \quad (\text{E.5})$$

The minimum of this function is given by

$$s_x = H_{xx'}^{-1} f_{x'}, \quad (\text{E.6})$$

which is the essence of the Newton method. One beneficial property of the Newton method is that the exact Hessian  $H$  is not required to be known,

<sup>1</sup> When rotations are rigorously excluded, the lattice only has 6 degrees of freedom.

Sum convention  $s_x f_x \equiv \sum_x s_x f_x$  is implied.

and one can find approximate matrices  $B$  that yield good results. Replacing the exact  $H$  by an approximate matrix  $B$  is known as the *quasi*-Newton method. Typically, an initial approximate Hessian  $B^0$  is chosen to be of simple form, e.g., a constant times unit matrix, or based on some simpler model [237]. The initial guess is then updated during the optimization, for example by means of the Broyden–Fletcher–Goldfarb–Shanno (BFGS) algorithm.<sup>2</sup> The configuration  $x$  is updated according

$$x^{i+1} = x^i + s_x^i = x^i + B_{xx'}^i f_{x'}^i. \quad (\text{E.7})$$

IF THE LATTICE DEGREES OF FREEDOM are represented by the Cartesian components  $a_i^\alpha$  of the lattice vectors, the generalized force on the lattice is given by

$$f_a = -V\sigma a^{-1t}, \quad (\text{E.8})$$

where  $V = \det a$  is the unit cell volume,  $\sigma$  is the  $3 \times 3$  stress tensor, and  $a$  is the lattice matrix.<sup>3</sup> For non-cubic systems, a diagonal Hessian matrix  $B^0 = c\mathbb{1}$  will therefore produce steps proportional to the reciprocal cell  $a^{-1t}$  which, among other things, can break the space-group symmetry of the crystal. This behavior can be avoided by defining the initial Hessian as

$$B^0 = ca^{-1t}a^{-1}, \quad (\text{E.10})$$

where  $c$  is a numerical constant. This particular choice of  $B^0$  can be viewed as making the Hessian diagonal in the native coordinate system of the lattice, i.e., when deformations of the lattice are viewed as strain transformations in terms of the strain tensor  $\varepsilon$ . By the choice of the Hessian according to Eq. (E.10), the resulting steps  $s_a^i$  will mimic such strain transformations early during the optimization:

$$a^{i+1} = a^i + s_a^i = (\mathbb{1} + \varepsilon_s^i)a^i. \quad (\text{E.11})$$

Another detail that must be taken into account is that updates of the lattice necessarily have to keep the relative atomic positions expressed in the crystal basis, i.e., their fractional coordinates, unchanged. The ideas outlined in this section have been implemented in FHI-*AIMS* and the performance compared to the previous implementation is shown in Fig. E.1.

The non-systematic decrease of the residual force observed in the previous implementation (`trm_2012`) was due to spurious distortions of the lattice and dislocations of the atomic arrangements generated by keeping their *Cartesian* instead of *fractional* positions unchanged during the lattice update. These artifacts are absent in the updated implementation (`trm`). The force convergence is generally faster and better behaved.

## E.2 Lattice optimization at finite temperature: Lattice expansion

At finite temperatures, the nuclear motion results in dynamical pressure  $p(T)$  and the lattice reacts by deforming,

$$a(T) = (\mathbb{1} + \varepsilon(T))a_0, \quad (\text{E.13})$$

<sup>2</sup> BFGS update for the estimated Hessian  $B^i$  from step  $i$  to  $i + 1$ :

$$B_{xx'}^{i+1} = B_{xx'}^i + \frac{B_{xy}^i s_y^i s_{y'}^i B_{y'x'}^i}{s_y^i B_{yy'}^i s_{y'}^i} - \frac{\delta f_x^i \delta f_{x'}^i}{\delta f_x^i s_{x'}^i},$$

with  $\delta f^i = f^{i+1} - f^i$ .

Symbolically:

$$f_a = -\frac{\partial V}{\partial a} = -V \underbrace{\frac{1}{V} \frac{\partial V}{\partial \varepsilon}}_{\sigma} \underbrace{\frac{\partial \varepsilon}{\partial a}}_{a^{-1t}}.$$

<sup>3</sup> The lattice matrix is the collection of lattice vectors  $\{\mathbf{a}_i\}$ ,

$$a = (\mathbf{a}_1, \mathbf{a}_2, \mathbf{a}_3). \quad (\text{E.9})$$

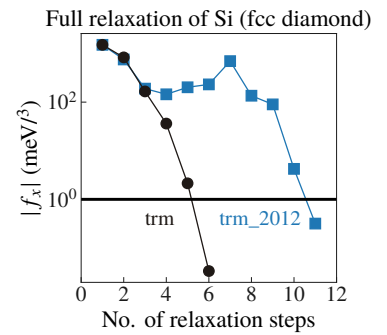


Figure E.1: Residual force component as function of the relaxation steps, before (`trm_2012`) and after (`trm`) optimizing the relaxation routine in FHI-*AIMS* according to the considerations presented in this chapter.

The volume expansion is usually measured in terms of the *thermal expansion coefficient*  $\alpha(T)$  [238]

$$\alpha(T) = \frac{1}{3V} \frac{\partial V(T)}{\partial T}. \quad (\text{E.12})$$

where  $a_0$  is the 0 K static lattice matrix, and  $a(T)$  is the lattice at finite temperature given in terms of a *strain transformation*  $\varepsilon(T)$ . The energy change per unit volume  $dW$  of a system subject to an infinitesimal strain deformation  $\varepsilon$  is defined as

$$dW = \sigma_\alpha^\beta d\varepsilon_\beta^\alpha , \quad (\text{E.14})$$

where  $\sigma$  is the *stress tensor* of the system. The lattice  $a(T)$  in thermal equilibrium will therefore be the lattice that minimizes the stress  $\sigma$  in Eq. (E.14). Depending on the crystal symmetry [239], the strain tensor  $\varepsilon$  has up to six independent values. Equation (E.14) therefore poses a six-dimensional optimization problem at a given temperature  $T$  which can be solved for example by coupling the system to a barostat and performing an *NPT* simulation

**CITE: NPT**

. In the language of the previous chapter, the lattice  $a(T)$  is then given as a time or ensemble average  $\langle a \rangle_{(p,T)}$  at thermodynamic conditions  $(p, T)$ . In practice however, this approach is quite inefficient and suffers from large noise, especially in the system sizes typically available to *ab initio* MD simulations

**CITE: ai NPT**

AN APPROXIMATE SOLUTION to the six-dimensional optimization problem of finding the finite temperature lattice  $a(T)$  can be found by the following rationale: We assume that the thermodynamic pressure at a given volume  $V$  and temperature  $T$  is given as

$$p(V, T) \approx \frac{Nk_B T}{V} + p_{\text{pot}}(V_0, T) + p_{\text{int}}(V) , \quad (\text{E.15})$$

where  $p_{\text{kin}}(T) = Nk_B T/V$  is the kinetic pressure, and  $p_{\text{pot}}(V_0, T)$  is the potential part of the pressure in the system at reference volume  $V_0$  which stems from the nuclear interaction  $\mathcal{V}(\mathbf{R})$  [240]. The last term,  $p_{\text{int}}(V)$ , is an internal pressure induced by the volume change. We assume that  $p_{\text{int}}(V)$  mainly stems from the lattice and is not temperature dependent. It can therefore be obtained from an equation of state parametrized at 0 K, for example the *Vinet equation* [241]:

$$p_{\text{int}}(V) = \frac{3B_0}{X^2} (1 - X) e^{\eta(1-X)} \quad \text{with} \quad (\text{E.16})$$

$$X = \left[ \frac{V}{V_0} \right]^{\frac{1}{3}} \quad \text{and} \quad \eta = \frac{3}{2} (B'_0 - 1) , \quad (\text{E.17})$$

where  $V_0$  is the volume,  $B_0$  is the bulk modulus, and  $B'_0 = \partial B_0 / \partial p$  is the isothermal pressure derivative of the bulk modulus. All these three parameters are obtained for the static lattice and we neglect their temperature dependence. Once the full parametrization of Eq. (E.15) is known, the temperature-dependent volume  $V_{\min}(T)$  is found by requiring zero pressure. The resulting pressure  $p_{\text{int}}(V_{\min})$  can be used to find the static reference lattice  $a(T)$  by optimizing the geometry while applying the external pressure  $p_{\text{relax}} = -p_{\text{int}}(V_{\min})$  as depicted in Fig. E.2.

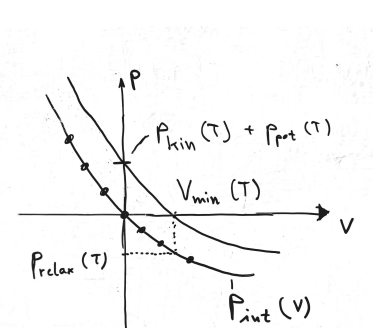


Figure E.2: Determination of relaxation pressure to obtain lattice at finite temperature. Dots denote volumes used to find  $V_{\min}(T)$  in Eq. (E.16).

The lattice  $a(T)$  obtained this way will then generate the static pressure contribution  $p_{\text{int}}$  which compensates the dynamical contributions stemming from kinetic and potential energy.

THE PROCEDURE GOES AS FOLLOWS:

1. To parametrize  $p_{\text{int}}(V)$ , calculate a  $p(V)$  curve for different volumes<sup>4</sup> and fit the Vinet equation of state given by Eq. (E.16) to obtain  $(V_0, B_0, B'_0)$ .
2. Perform MD simulation at  $V_0$  and target temperature  $T$  until pressure  $p_{\text{pot}}(V_0, T)$  is sufficiently converged.
3. Minimize Eq. (E.15) with respect to volume to find  $V_{\min} = \arg \min_V p(V, T)$ .
4. Predict pressure  $p_{\text{relax}} = -p_{\text{int}}(V_{\min})$  and obtain a reference structure of correct volume  $V_{\min}$  by applying this pressure during a geometry optimization, see Fig. E.2. The lattice of this structure will satisfy  $\det a(T) = V_{\min}$ .

AFTER THE LATTICE  $a(T)$  IS OBTAINED, it should be verified that the pressure  $p(V_{\min}, T)$  is indeed minimized. If a significant residual pressure  $p_{\text{residual}}$  persists it can be added to the pressure used for relaxation until self consistency is reached.

<sup>4</sup> For non-cubic systems or systems with internal degrees of freedom, use a set of external pressures  $p_{\text{relax}}$  to obtain a set of reference structures at different volumes  $V_{p_{\text{relax}}}$  by geometry optimization.

# F

## *Linear Response Distribution Function*

To solve for  $\Delta f(t)$  defined in Eq. (3.10), we introduce a shorthand notation such that

$$\frac{d\Delta f}{dt} = -iL\Delta f(t) - i\Delta L(t)f^0, \quad (\text{F.1})$$

where the Liouville operator  $L^0$  is defined by

$$iL^0 g = \{g, H^0\}, \quad (\text{F.2})$$

and similarly

$$i\Delta L(t)g = \{g, H'(t)\}. \quad (\text{F.3})$$

Equation (F.1) is a first order linear differential equation of the form

$$\frac{dy}{dt} + p(t)y = q(t), \quad (\text{F.4})$$

which is straightforward to solve by using an integrating factor as follows: We identify  $y = \Delta f$ ,  $p(t) = iL^0$ , and  $q(t) = -i\Delta L(t)f^0$ . Following Ref. [242, p. 68], we define the integrating factor  $\rho(t) = \exp(\int dt p(t)) = \exp(iL^0 t)$ , multiply Eq. (F.4) with  $\rho(t)$ , and use that  $\frac{d}{dt} \rho(t) = \rho(t)p(t)$  to obtain

$$\frac{d}{dt}(\rho(t)y) = \rho(t)q(t).$$

This gets integrated to

$$\rho(t)y = \int_{-\infty}^t dt' \rho(t')q(t')$$

under the boundary condition  $y(t \rightarrow -\infty) = 0$ . In total we obtain

$$y(t) = \rho^{-1}(t) \int_{-\infty}^t dt' \rho(t')q(t'), \quad (\text{F.5})$$

$$\implies \Delta f(t) = -e^{-iL^0 t} \int_{-\infty}^t dt' e^{iL^0 t'} i\Delta L(t')f^0. \quad (\text{F.6})$$



# $G$

## *Explicit Formulas*

### *G.1 Harmonic Approximation*

In Sec. 2.2.5, we introduced the shorthand notation  $s = (b, \mathbf{q}), -s = (b, -\mathbf{q})$  to write brief formulas. We give the explicit form of these formulas here.

THE NORMAL MODE COORDINATES in the periodic case in terms of complex amplitudes  $a_b^{(\dagger)}(\mathbf{q})$  read

$$u_b(\mathbf{q}) = \frac{1}{\sqrt{2\omega_b(\mathbf{q})}} [a_b^\dagger(-\mathbf{q}) + a_b(\mathbf{q})] \quad (\text{G.1a})$$

$$p_b(\mathbf{q}) = i\sqrt{\frac{\omega_b(\mathbf{q})}{2}} [a_b^\dagger(-\mathbf{q}) - a_b(\mathbf{q})] \quad (\text{G.1b})$$

The inverse relation is given by

$$a_b(\mathbf{q}) = \sqrt{\frac{\omega_b(\mathbf{q})}{2}} u_b(\mathbf{q}) + \frac{i}{\sqrt{2\omega_b(\mathbf{q})}} p_b(\mathbf{q}) \quad (\text{G.2a})$$

$$a_b^\dagger(-\mathbf{q}) = \sqrt{\frac{\omega_b(\mathbf{q})}{2}} u_b(\mathbf{q}) - \frac{i}{\sqrt{2\omega_b(\mathbf{q})}} p_b(\mathbf{q}) \quad (\text{G.2b})$$

The displacements are recovered by

$$\mathbf{u}_{iL} = \frac{1}{\sqrt{N_q}} \sum_{bq} e^{i\mathbf{q} \cdot \mathbf{R}_{iL}^0} \mathbf{e}_{bi}^*(\mathbf{q}) u_b(\mathbf{q}) \quad (\text{G.3})$$

and likewise for  $\mathbf{p}$ .

The Hamiltonian reads

$$\mathcal{H}(u_b, p_b) = \frac{1}{2} \sum_{bq} [p_b^*(\mathbf{q}) p_b(\mathbf{q}) + \omega_b^2(\mathbf{q}) u_b^*(\mathbf{q}) u_b(\mathbf{q})] \quad (\text{G.4})$$

Equations of motion

$$\ddot{u}_b(\mathbf{q}) = \dot{p}_b(\mathbf{q}) = -\frac{\partial \mathcal{H}}{\partial u_b^*(\mathbf{q})} \quad (\text{G.5})$$

## G.2 Heat Capacity

$$\beta = \frac{1}{k_B T} \quad (\text{G.6a})$$

$$c_V = \frac{\partial E}{\partial T} \quad (\text{G.6b})$$

$$E(T) = \sum_s \hbar\omega_s n_s(T) \quad (\text{G.6c})$$

$$n_s(T) = \frac{1}{e^{\beta\hbar\omega_s} - 1} \quad (\text{G.6d})$$

$$\frac{\partial n_s}{\partial T} = \frac{\hbar\omega_s}{k_B T^2} n_s(n_s + 1) \quad (\text{G.6e})$$

$$\Rightarrow c_V = \sum_s \underbrace{\frac{\hbar^2\omega_s^2}{k_B T^2} n_s(n_s + 1)}_{c_{V,s}} \quad (\text{G.6f})$$

Classical limit  $k_B T \gg \hbar\omega_s$

$$n_s(T) \rightarrow \frac{k_B T}{\hbar\omega_s} \gg 1 \quad (\text{G.7a})$$

$$\Rightarrow E(T) \rightarrow 3Nk_B T \quad (\text{G.7b})$$

$$\Rightarrow c_V \rightarrow 3Nk_B \quad (\text{G.7c})$$

*H*

## *Computational details*

**TODO:** Add table with: material, atoms in prim. cell, supercell size, cubicness(?), time step, simulation time, no. of trajectories, residual pressure.



*I*

*Experimental References*

Space group	materialsproject ID	material	$\kappa^{\text{experiment}}$	References
61	mp-753	ZnSb	3.50*	[243]
62	mp-691	SnSe	0.60*, 1.00, 1.30	[8, 175, 10]
62	mp-1477	BaSi <sub>2</sub>	1.38*, 1.60*	[244, 181]
62	mp-20331	CuSbSe <sub>2</sub>	2.00*	[245]
122	mp-5342	AgGaS <sub>2</sub>	1.40	[183]
122	mp-5518	AgGaSe <sub>2</sub>	1.00	[183]
164	mp-2646	Mg <sub>3</sub> Sb <sub>2</sub>	2.08, 2.50	[176, 177]
186	mp-22894	AgI	0.30*	[246]
186	mp-672	CdS	16.0	[11]
186	mp-1070	CdSe	9.00, 9.00*	[247, 248]
186	mp-2133	ZnO	60.0	[11]
206	mp-216	Sc <sub>2</sub> O <sub>3</sub>	17.0*	[249]
216	mp-2172	AlAs	98.0	[11]
216	mp-406	CdTe	8.00	[250]
216	mp-22913	CuBr	1.25	[162]
216	mp-22914	CuCl	0.84*	[163]
216	mp-22895	CuI	1.68	[162]
216	mp-2534	GaAs	45.0	[11]
216	mp-20305	InAs	30.0	[11]
216	mp-10695	ZnS	27.0	[11]
216	mp-1190	ZnSe	19.0	[11]
216	mp-2176	ZnTe	18.0	[11]
221	mp-22906	CsBr	0.94	[251]
221	mp-22865	CsCl	1.00, 1.00	[251, 252]
221	mp-1056920	CsI	1.10	[251]
221	mp-3448	KMgF <sub>3</sub>	10.0	[253]
221	mp-5878	KZnF <sub>3</sub>	5.50	[254]
221	mp-5229	SrTiO <sub>3</sub>	10.0, 11.5	[255, 256]
225	mp-23231	AgBr	1.10	[257]
225	mp-22922	AgCl	0.90*, 1.00	[258, 259]
225	mp-1342	BaO	2.30	[11]
225	mp-2605	CaO	27.0	[11]
225	mp-23251	KBr	2.80*, 3.40	[260, 11]
225	mp-23193	KCl	6.50*, 7.10	[260, 11]
225	mp-463	KF	6.43	[11]
225	mp-22898	KI	1.96*, 2.60	[260, 11]
225	mp-23259	LiBr	1.83*	[261]
225	mp-1138	LiF	17.6	[11]
225	mp-23703	LiH	14.7	[167]
225	mp-1265	MgO	55.2, 60.0, 61.7	[158, 11, 154]
225	mp-22916	NaBr	2.30*, 2.80	[262, 11]
225	mp-22862	NaCl	6.00*, 6.06, 6.57, 6.90, 7.10	[263, 154, 264, 265, 11]
225	mp-682	NaF	16.50	[11]
225	mp-23268	NaI	1.33, 1.80	[263, 11]
225	mp-22867	RbBr	3.38*, 3.80	[260, 11]
225	mp-23295	RbCl	2.41*, 2.80	[260, 11]
225	mp-11718	RbF	2.27	[261]
225	mp-22903	RbI	1.98*, 2.30	[260, 11]
225	mp-2472	SrO	10.00	[11]
225	mp-2741	CaF <sub>2</sub>	9.76	[266]
225	mp-241	CdF <sub>2</sub>	4.30	[266]
225	mp-23209	SrCl <sub>2</sub>	2.30	[267]
225	mp-981	SrF <sub>2</sub>	8.07, 10.00	[267, 266]

Table I.1: Experimental thermal conductivities at room temperature with experimental reference. Values marked with (\*) come from measurements of polycrystalline samples.